Modelling fast electron transport in solids and with application to Rayleigh-Taylor instability studies

Reem A. B. Alraddadi

Doctor of Philosophy

University of York

Physics

September 2015

Abstract

This thesis presents numerical investigations of the fast electron transport and discusses the fast electron heating of solid targets. Three areas have been investigated in this context:

The first area introduces the concept of an ideal fast electron transverse confinement which is obtained when the transverse dimensions of the target are comparable to the laser spot size. This facilitates the heating of thick targets. This investigation also explores the angular dispersion phenomenon in the context of the fast electrons. This dispersion results in a longitudinal velocity spread of the fast electrons which adversely affects their penetration of the target, and this in turn impairs the heating. The work here shows that angular dispersion can not be avoided even when ideal fast electron transverse confinement is achieved. Moreover, this dispersion impedes fast electron penetration more significantly than does electric field inhibition. The results indicate the importance of taking the angular dispersion into account in fast electron transport calculations.

The second area investigates the effect of grading the atomic number at the interface between the guide element and the solid substrate on resistive guide heating. The numerical results imply that this graded interface configuration improves the heating in large radius guide resembling that obtained in smaller guide. The larger radius guide with the graded interface configuration is more tolerant to laser pointing stability than smaller radius. Further, this configuration increases the magnetic collimation of fast electrons since more powerful confining magnetic field is obtained.

The last area studies numerically a Rayleigh-Taylor (RT) instability experiment driven in a fast-electron-heated solid target. It was found that it is possible to drive the RT instability in dense plasma isochoric heated by the fast electrons. The RT instability growth occurs in few picoseconds, after establishing strong radiative cooling. The curve growth rates depends on the type of atomic model used. Practicalities of extracting RT instability data due to structure in the heating profile are described.

Contents

List of Figures

List of Tables

Acknowledgement

I would like to express my gratitude and thanks to my supervisor Prof. Nigel Woolsey for his constant guidance and inspiration. His attention to detail and patience during long hours of discussion have been invaluable throughout my PhD. In the same time, I am also forever indebted to Dr. Alex Robinson for his co-supervision on the majority of this thesis and for introducing me to the fast electron transport field. The time, knowledge and funding for my frequent trips to RAL that he has provided is invaluable. It has been a great honour to learn how to be a physicist from Prof. Nigel Woolsey and Dr. Alex Robinson.

I would like to thank Dr. John Pasley for all his support during studies and for providing the last version of HYADES. My thanks also go to Dr. Andrew Rossall and Dr. Kate Lancaster for sharing their experimental experience and for their constant encouragement. I would like to thank the laser-plasma staff in York Plasma Institute, especially Prof. Greg Tallents and Prof. Geoff Pert.

I would like to express my gratitude to the plasma simulation group at the Central Laser Facilities at RAL for their warm welcome whenever I visited. I would especially like to thank Dr. Raoul Trines for his help with Linux and bearing with all my questions and Tom Fox for our enjoyable simulation discussions. I am grateful to Derek Ross and Ahmed Sajid from STFC's Scientific Computing Department for their technological support. Also, my thanks go to Ian Bush for his supportive e-mails. A big thank you to my fellow students at York Plasma Institute for their support, especially Rachel Dance, David Blackman, Mohammed Shahzad, Jonathan Brodrick, Peshwaz Abdoul, Ozgur Culfa, Robert Crowston and Lee Morgan.

Finally, I would like to thank my brother Abdullah, the only member of my family in the UK, for his great, constant support over these years. Thanks also go to my parents and family for their love and encouragement also to Prof. Mohamed El-Gomati for his great support.

Author's Declaration

I, Reem A. B. Alraddadi, declare that the work presented in this thesis, except where it is otherwise stated, is based on my own research and has not been submitted previously for a degree in this or any other university.

The work presented in Chapters 4 and 5 in this thesis is entirely the author's own work. This includes the simulations and the analysis. The analytical work of the angular dispersion is derived by A. P. L. Robinson. All simulations in Chapter 6 are the author's own work. The author did not have any role in the experimental work. This includes planning, performing and analysing the data of the experiment. The IDL code used to read and extract HYADES opacity data was written by the author.

Chapter 1

Introduction

1.1 Introduction and motivation

Extreme states of matter in conditions of high temperatures and densities resembling those found elsewhere in the universe can now be created on Earth due to the technological development of various devices such as lasers. This matter is in the plasma state, composed of charged particles characterised by few particles in a Debye sphere and strong coupling parameter greater than unity [6, 7].

When an ultra-intense laser interacts with solid matter, the matter is compressed by the laser radiation pressure, this is of the order of 10^{14} Pa for a laser intensity of 10^{18} Wcm^{-2}. At this laser intensity and above, the motion of an electron becomes relativistic and the density, at which the laser and plasma frequencies match, increases by a factor of γ. This allows the laser to deposit a significant fraction of its energy at higher densities than is possible in low intensity laser-plasma interactions [8]. The laser energy couples to electrons at the relativistic critical density, and these in turn acquire high energies of several MeV [9]. These "fast" and energetic electrons carry energy to the cold dense region of the plasma where the laser cannot reach. One area of great interest is to heat targets at constant volume or isochorically [10]. This type of heating, where the density is known precisely, is required to investigate dense plasma properties [11], such as opacity and equation of state.

The opacity and equation of state are crucial to the understanding of a number of fields such as inertial confinement fusion (ICF) [12] and astrophysics. Although this heating can be obtained to some extent in thin targets [13,14], the small inertial confinement time of thin targets, which is roughly equal to the target thickness divided by the sound speed [15] drives interest in thicker targets. For example, the inertial confinement time of an Al target with a thickness of 10 μm is less than 1 ns if this target is heated to $T_e = 300$ eV, so the sound speed can reach $\approx 10^7$ cms^{-1}. So these thin targets expand rapidly. Also, the isochoric heating of thick targets is desirable in the investigation of hydrodynamic phenomena such as the Rayleigh-Taylor instability [16]. Although different experimental approaches have been employed in order to obtain isochoric heating, these include X-ray [15, 17], laser-driven shock [18] and proton heating [10], these techniques all have limitations as isochoric heating methods [10, 15]. This thesis explores fast electron heating in thick targets and explains how a thick target can be designed to decrease the temperature gradients across its depth.

The main advantage of using fast electrons is that they efficiently absorb laser energy and are capable of heating targets to high temperatures [19] in a timescale which is shorter than hydrodynamic timescales (usually in ns). The main heating mechanism is Ohmic heating which results from a collisional return current. This resistive background electron current heats the target as it flows to balance the opposite fast electron current. Sherlock *et al*. [20] recently found that the collisional damping of large amplitude plasma waves induced by the fast electrons is another important source of heating. However, fast electron penetration of a target and as a result target heating is obstructed by a number of mechanisms, most notably electric field inhibition [21], fast electron spreading [22, 23], filamentation [24] and angular dispersion. These mechanisms need to be considered carefully when designing a thick target.

Generally, fast electron transport into a thick target can be divided into five

stages as described by Norreys *et al.* [25]. The first stage is at the beginning of the laser pulse when the fast electrons are ponderomotively accelerated into the cold plasma and electric fields are setup. These fields then accelerate the background electrons to draw a return current. The second stage is when the fast electrons slow down due to electric field inhibition and the plasma temperature starts to rise due to Ohmic heating. The third stage is when the plasma enters a Spitzer-like regime (the temperature is of the order of 100 eV [26]) and the fast electrons are able to penetrate further due to the reduction in resistivity. The fourth stage is when the energy loss through collisions becomes significant (drag) and angular scattering of the fast electrons starts to dominate. The final stage is when thermal diffusion carries the deposited energy deeper into the target due to the large temperature gradient. Practically, distinguish ability between these stages is difficult as the plasma rapidly evolves between these stages [25].

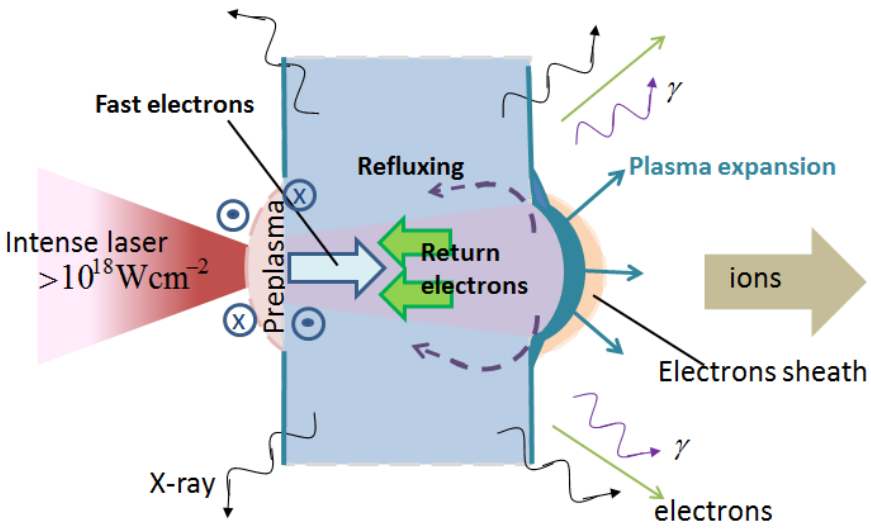

Figure 1.1: Overview of the main mechanisms that occur when a laser of intensity $> 10^{18}$ Wcm^{-2} interacts with a solid target.

Figure 1.1 shows a schematic of the main mechanisms which occur when a laser of intensity $> 10^{18}$ Wcm^{-2} interacts with a solid density target and fast electrons penetrate into the target. First, the laser interacts with the surface of the solid

target. The pre-plasma forms at the surface due to the edge of the laser pulse arriving before the main pulse. This pulse ionises the target, leading to an exponential decrease in density from the target surface. Then the peak pulse reaches and interacts with the plasma at the corrected critical density γn_{crit} [1]. At this region, a large fraction of the laser energy is converted into fast electrons which are accelerated in the direction of the laser propagation. This causes charge separation from the background ions within the plasma which in turn sets up an electrostatic field and a large magnetic field. The electrostatic field then accelerates the heavier ions. Moreover, both electrostatic and magnetic fields prevent any further penetration of the fast electrons into the target. However, since the plasma is ionised, it can supply a background (return) current that limits the magnetic field. In the target, the fast and background current densities nearly balance, i.e. $\mathbf{j}_f + \mathbf{j}_b \approx 0$ allowing the fast electrons to propagate. As the background electron density n_b is much higher than the fast electron density n_f, the balanced current densities ensure that the background current drift speed v_b is low compared to the fast electrons' current speed v_f. The latter is approximately the speed of light. The slow moving background current is highly collisional and heats the target. In addition, the fast electrons travel transversely with large divergence angles. This angular spread has no clear characterisation and adds considerable complexity to the field of fast electron transport [27]. A fraction of the fast electrons will leave the rear surface of a target. This sets up a sheath field. One result of this is the acceleration of ions by the target normal sheath acceleration (TNSA) mechanism. Further, if the target is thin, the fast electrons can be reflected at the back of the target by this sheath. This is referred to as refluxing [28]. Finally, the plasma pressure increases rapidly due to rapid heating, which is mostly by Ohmic heating, leading to the plasma expansion but on hydrodynamic timescales. More details regarding some of these processes are given later in Chapter 2.

The rich physics of fast electron transport makes it of great interest in a number

of applications [29, 30] including the Fast Ignition (FI) approach to the inertial confinement fusion scheme [31]. In the FI approach, fast electrons are used to heat the core of a spherically compressed DT plasma to temperatures exceeding 5 keV. This part is critical as it needs accurate characterisation and control of fast electron transport. Robinson *et al.* [27] cite the following three reasons why fast electron transport is challenging for FI:

1. The stand-off distance, i.e. the distance between the fast electron source (at γn_{crit}) and the centre of the compressed fuel (hot spot), is several times the size of the hot spot and fast electron source, so a reduction in the coupling efficiency might occur due to angular spread.

2. There is a high possibility of various fast electron transport instabilities.

3. There are difficulties in depositing all the fast electrons in the hot spot.

This thesis presents three pieces of work which investigate fast electron heating. The first explores how the heating of thick targets can be facilitated using a wire-like shaped target to control the fast electron spreading. As part of this, a numerical investigation is carried out to explore the effect of the angular dispersion of the fast electrons on target heating and compared with the effect of electric field inhibition on target heating. The second piece of work is a study the heating in larger radius of the resistive guide using laser-generated-fast-electrons, aiming to improve the uniformity of heating and to increase the magnetic collimation. This part mainly explores the effect of grading the atomic number at the interface between the guide element and the solid substrate. The third part of the study concerns the numerical investigation of an experiment designed to study the Rayleigh-Taylor instability that is driven in a fast electron heated target. This work involves extensive simulations using a hybrid-PIC code to investigate the fast electron heating and hydrodynamic codes to examine the Rayleigh-Taylor hydrodynamic instability.

1.2 Thesis outline

This thesis consists of seven chapters, the first of which is this short introduction. The next six chapters are summarised below:

Chapter 2: outlines some of the basic physics of fast electron transport and gives a brief overview of femtosecond lasers and fast electron generation. The physics relating to fast electron transport is then discussed, followed by a description of the fast electron transport code ZEPHYROS.

Chapter 3: discusses the physics relating to the simulation work of Chapter 6. This thesis investigates a Rayleigh-Taylor target heated by fast electrons and the simulations involve a number of physical principles such as fast electron heating, radiative cooling, opacity and the hydrodynamic Rayleigh-Taylor unstable situation. The basic physics relating to the simulations is discussed here, along with a description of the hydrodynamics codes HYADES and HELIOS.

Chapter 4: discusses a wire-like shaped target design whereby the transverse confinement of the fast electrons can be achieved. Since angular dispersion has been neglected in most fast electron transport calculations, an analytical and numerical investigation of its effect on the heating has been carried out here. This chapter also investigates the competing effects of angular dispersion and electric field inhibition in impeding fast electron penetration which thus impairs the heating with depth in the target.

Chapter 5: investigates the effect of grading the atomic number at the interface between the guide element and the solid substrate, i.e. surrounding target. This graded interface configuration is investigated into two main schemes of resistive guiding; a pure-Z and a multilayered resistive guides. The aim of this configuration is to improve the heating across the depth of a large radius guide since those larger guides provide more tolerance to laser pointing stability. The theory of resistive guiding structure and heating in the resistive guide are

discussed. Numerical discussions are presented to analyse both the growth rate of azimuthal magnetic field and guide heating using the graded interface configuration.

Chapter 6: explores numerically the radiative cooling Rayleigh-Taylor experiment that was performed by Rossall *et al.* [4]. This experiment is application of the fast electron heating. The target heating, cooling rate, radiation transport and Rayleigh-Taylor instability are investigated numerically and are compared with the experimental results.

Chapter 7: summarises the findings of the thesis and suggests ideas for further study in this field.

Chapter 2

Fast electron transport

This chapter presents the theoretical background to the analytical and numerical work discussed mainly in Chapters 4 and 5. After a brief introduction to the ultra-intense laser, an overview of fast electron generation is presented followed by an in-depth discussion of the fast electron transport.

2.1 Femtosecond petawatt laser: review

The laser-plasma scientist is primarily interested in four laser parameters: pulse duration, energy, pulse shape contrast and the focal spot size. These parameters are responsible for determining the laser power transferred per unit area (intensity) and the condition of the target during the interaction. The invention of the chirped pulse amplification (CPA) technique in 1985 [32] makes it possible to reach intensities of $> 10^{18}$ Wcm^{-2}. Before CPA, it was almost impossible to achieve such high intensities, since a laser pulse of GWcm^{-2} causes significant damage to the active medium due to the nonlinear processes. The CPA technique provides a way of obtaining higher intensities by stretching out a short laser pulse in time to prevent damaging the laser components.

The peak intensity $> 10^{18}$ Wcm^{-2} does not immediately interact with the pure solid target. It is often accompanied by a nanosecond pre-pulse τ_{ASE}, produced by

amplified spontaneous emission, (low intensity pulse $I_{\mathrm{ASE}} < 10^{13}$ Wcm^{-2}) interacts first with the solid target and creates a pre-plasma as shown in Figure 2.1(a). Then the peak intensity interacts with the pre-plasma before reaching solid density. Here, the electrons are accelerated to relativistic speed as shown in Figure 2.1(b). The ratio of peak pulse to pre-pulse (laser contrast factor) needs to be known and in most cases be sufficiently high to prevent plasma formation. In this way, the surface of the target remains unperturbed until the main pulse arrives and thus can interact with the solid target.

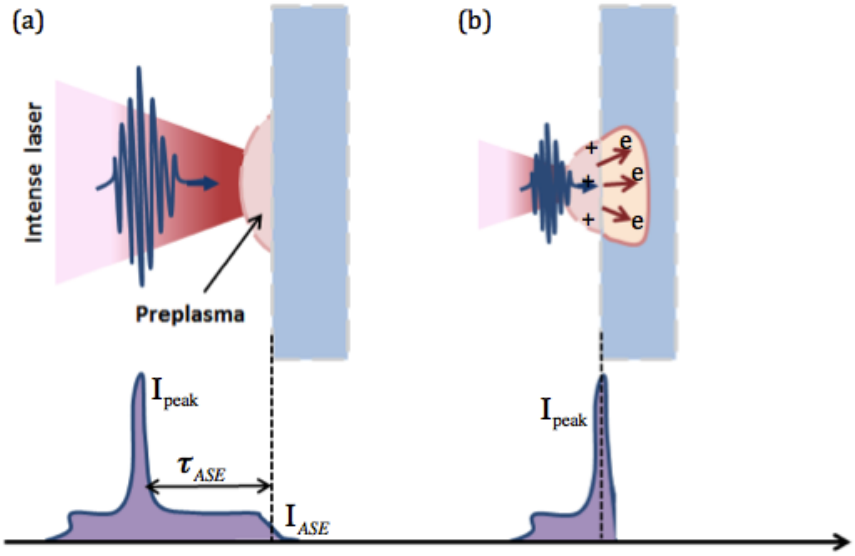

Figure 2.1: (a) The ASE intensity arriving at the target surface, prior to the peak intensity, creates a pre-plasma. (b) The peak intensity interacts with the pre-plasma, ponderomotively accelerating electrons into the target to relativistic speed. This figure is reproduced from [1].

The main feature of the short pulse laser in comparison with the long pulse laser, in addition to the intensity, is that there is not enough time for coronal plasma (high temperature, low density plasma) to form in front of the target during the interaction. The amount of plasma formed due to the short pulse-solid interaction is estimated by,

$$L_s = c_s \tau_L. \tag{2.1}$$

where τ_L is the pre-pulse duration and c_s is the adiabatic sound speed [8],

$$c_s = \left(\frac{Z_{eff}k_BT_e}{m_i}\right)^{1/2} \simeq 3.1 \times 10^7 \left(\frac{T_e}{\text{keV}}\right)^{1/2} \left(\frac{Z_{eff}}{A}\right)^{1/2} \text{cm s}^{-1} \tag{2.2}$$

where Z_{eff} is the effective ion charge, k_B is the Boltzmann constant, T_e is electron temperature, m_i is ion mass and A is the atomic mass number. For example, if a 500 fs pulse heats an Al target to 300 eV and assuming that $Z_{eff} = 9$, a very steep density profile would be formed of $L_s \approx 0.05$ μm [8]. This is less than the laser wavelength of an ultra-intense laser, which is usually 1 μm. Because of this steep gradient, the laser deposits its energy at critical density γn_{crit} as shown in Figure 2.2,

$$n_{crit} = \frac{\epsilon_0 m_e c^2}{e^2 \lambda_L^2}. \tag{2.3}$$

where $\gamma = 1/(1-\beta_s^2)^{1/2}$ is the Lorentz factor, $\beta_s = v/c$, v is the electron velocity, c is the speed of light, ϵ_0 is vacuum permittivity, m_e is the electron mass, e is charge and λ_L is the wavelength of the laser in vacuum. As shown in Figure 2.2, the laser interacts with the steep density gradient and it is reflected at the turning point. However, the laser electric field can tunnel beyond this point to γn_{crit}, i.e. the laser beam propagates to a density that is increased by the γ factor, depending on the absorption mechanisms. This is due to the fact that at intensities of $> 10^{18}$ Wcm^{-2}, where the electric field exceeds 10^{13} Vm^{-1}, electrons oscillate at relativistic velocities. This increases the electron mass to γm_e, which reduces the ability of the electrons to generate a current in the plasma that reflects the laser light more readily. Thus, an intense laser beam penetrates deeper into the plasma. The strength of the relativistic effects is usually indicated via the normalised vector potential of a laser beam [9,33],

$$a_0 = \frac{P_{osc}}{m_e c} = \frac{\gamma v_{osc}}{c} = \frac{eE_L}{m_e c \omega_L} = \sqrt{\frac{I_L \lambda_L^2}{1.3 \times 10^{18}}} \tag{2.4}$$

where $P_{osc}(v_{osc})$ is the transverse quiver momentum (velocity) of the electron in

the laser field, E_L is the peak electric field of the laser, ω_L is the frequency of the laser and I_L is the laser intensity. Thus if $a_0 >> 1$, the oscillation of the electron in the electromagnetic field of the laser becomes relativistic. For $\lambda_L = 1\ \mu$m, $E_L \approx 10^{13}$ Vm^{-1} [34] and $I_L \approx 5 \times 10^{20}$ Wcm^{-2}, $a_0 \approx 20$.

This thesis presents a study of the fast electron transport that is generated via a high-power short pulse laser where the intensity reaches 10^{20} Wcm^{-2}.

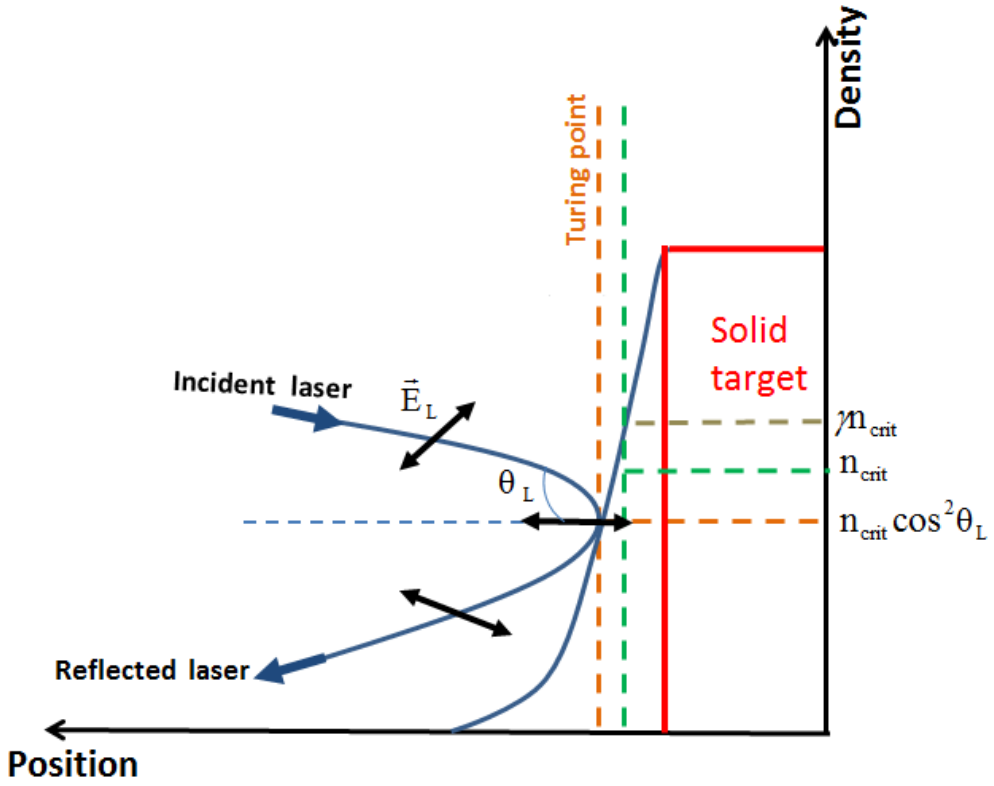

Figure 2.2: Sketch of the density profile of the laser beam incident at θ_L. Part of the electric field of the laser, that is parallel to ∇n_e at turning point, can tunnel to the critical surface depending on the absorption mechanisms.

2.2 Fast electron generation and its temperature scaling

When $I\lambda_L^2 > 10^{18}$ Wcm^{-2} interact with a target, its front surface exhibits a steep density gradient. Two main mechanisms are important here: vacuum heating and relativistic $\mathbf{J}\times\mathbf{B}$ force. These mechanisms act to convert a significant fraction of laser energy into kinetic energy of fast, relativistic electrons. It has been experimentally demonstrated that 20 % [35] to 50 % of the laser energy will be converted to fast electrons at critical density [36].

The vacuum heating mechanism was first introduced by Brunel [37]. It occurs near to the vacuum-plasma interface and in experiments with very high contrast lasers. The electrons, which are near to the target edge, get pulled away from the target into the vacuum. However, because the laser's electric field oscillates as it changes direction the electrons are accelerated back into the dense plasma where $n_e >> \gamma n_{crit}$, carrying the laser energy into the target.

The ponderomotive $\mathbf{J} \times \mathbf{B}$ force mechanism is similar to the vacuum heating, except that the electrons are driven in the direction of the laser propagation by the Lorentz force. This force depends on the spatial gradient in the laser light near vacuum-plasma interface and oscillates the electrons with frequency $2\omega_L$ [9, 38, 39]. The ponderomotive force can be derived by considering non-relativistic electron motion in the wave of an electromagnetic field, as shown below following Ref. [34],

$$m_e \frac{d\mathbf{v}}{dt} = -e[\mathbf{E}(r) + \mathbf{v} \times \mathbf{B}], \tag{2.5}$$

where the electric field has the following waveform: $\mathbf{E}(r) = E_0(r)\cos(\omega_0 t)$ and $E_0(r)$ is the spatially varying amplitude. The (2.5) can be written in the non-linear second order approximation as,

$$m_e \frac{d\mathbf{v}_2}{dt} = -e[(\delta\mathbf{r}_1.\nabla)E|_{r=r_0} + \mathbf{v}_1 \times \mathbf{B}_1], \tag{2.6}$$

The term $(\delta\mathbf{r}_1.\nabla)E|_{r=r_0}$ comes from expanding $\mathbf{E}(r)$ during its motion at r_0 using the Taylor expansion rule. $\delta\mathbf{r}_1$ is electron displacement in the electric field and $\mathbf{v}_1$ is the velocity. The velocity and displacement can be obtained from (2.5) by ignoring $\mathbf{v} \times \mathbf{B}$ term (since this is for the first order) and integrating. The first integration obtains the velocity, and the second integration obtains the displacement,

$$\mathbf{v}_1 = \frac{-e}{m_e\omega_0}\mathbf{E}_0 \sin(\omega_0 t), \tag{2.7}$$

$$\delta\mathbf{r}_1 = \frac{e}{\omega_0^2 m_e}\mathbf{E}_0 \cos(\omega_0 t), \tag{2.8}$$

The magnetic field can be derived from Maxwell's equation $\nabla \times \mathbf{E}(\mathbf{r}) = -\partial\mathbf{B_1}/\partial t$ by integration,

$$\mathbf{B}_1 = -\frac{1}{\omega_0}\nabla \times \mathbf{E_0} \sin(\omega_0 t), \tag{2.9}$$

Substituting equations from (2.7) to (2.9) into (2.6) and using the waveform of the electric field and averaging over time, then using identity $\nabla E_0^2 = 2E_0 \times \nabla \times E_0 + 2E_0(\nabla.E_0)$, the ponderomotive force is obtained,

$$\mathbf{F}_{pond} = m_e < \frac{d\mathbf{v}_2}{dt} >= -\frac{1}{4}\frac{e^2}{m_e\omega_0^2}\nabla E_0^2. \tag{2.10}$$

If the ponderomotive force is generated by an electrostatic wave, the first term in (2.6) will be dominant. If the electron quiver velocity becomes relativistic, the second term in (2.6) dominates the ponderomotive force. In the context of intense laser-plasma interactions, this expression is relativistically corrected to [9],

$$\mathbf{F}_{pond} = -\nabla(\gamma - 1)m_e c^2. \tag{2.11}$$

On the other hand, the fast electron temperature, T_f, is not easy to determine due to these various absorption processes and the complex distribution of the fast electron mean energy. The fast electron temperature indicates mean energy of the

fast electron population [38]. Beg law provides a rough indication of the expected fast electron temperature at intensities up to 10^{19} Wcm^{-2} [40] and defined as,

$$T_{Beg} \approx 200 \left(\frac{I_L \lambda_L^2}{10^{18} \text{ Wcm}^{-2}} \right)^{1/3} \text{ keV}. \tag{2.12}$$

Wilks ponderomotive law gives another rough indication at intensities above 10^{18} Wcm^{-2} and defined as [33],

$$T_{pond} \approx 511 \left[\sqrt{1 + \frac{I_L \lambda_L^2}{1.38 \times 10^{18} \text{ Wcm}^{-2}}} - 1 \right] \text{ keV} \tag{2.13}$$

where λ_L in μm in both scales.

Recently, Sherlock [41] showed numerically that the ponderomotive scaling should be reduced by a factor of 0.4, i.e. $T_f = 0.6 T_{pond}$, since fast electrons undergo deceleration due to moving out of the absorption region and into the dense plasma. Also, Kluge *et al.* [42] introduced new scaling laws derived from the Lorentzian steady state distribution function for electron energy. In their model, they assumed high intense-laser contrast without taking into account the increase in temperature due to fast electron refluxing. Their scaling predicted that the fast electron mean energy is in the same order as Beg's law (2.12). Within the scope of fast electron transport modelling, Robinson *et al.* [27] have stated that recent 3D Particle-In-Cell (PIC) simulations in line with relativistic electron mean energy given by Wilks's ponderomotive scaling (2.13). In this thesis, the reduced ponderomotive scaling as shown by Sherlock [41] has been used in our modelling using the ZEPHYROS code (Section 2.4).

2.3 Fast electron transport

2.3.1 Fast electrons properties

When an intense laser beam interacts with a solid target, part of the laser's energy is reflected and another part is transferred to electrons, which then propagate away from the injection region into the target. Based on energy conservation, the energy flux balance can be applied [8], which yields,

$$\beta I_L = n_f v_f \bar{\epsilon_f} \tag{2.14}$$

where β is the fraction of laser energy coupled into the fast electrons, I_L is the laser intensity in Wm^{-2}, n_f is the fast electron density in m^{-3}, v_f is the fast electron velocity in ms^{-1} and $\bar{\epsilon_f}$ is the mean energy of the fast electrons in J, which exhibit Wilks ponderomotive law (2.13) [33]. This balance states that the absorbed flux of the laser's energy is approximately equal to the heated electrons' energy flux. As the fast electrons are not atomically bounded [27] , one can estimate from (2.14) fast electron properties as follows:

The fast electron density can be estimated if one considers, for example, that a laser intensity is 10^{24} Wm^{-2} (note here the unit change to SI) with wavelength of 1 μm interacts with the target and only 30 % of the laser's energy is transferred to fast electrons. Thus, the density of the fast electrons is $n_f \approx 2 \times 10^{27}$ m^{-3} and with a mean energy of $\bar{\epsilon_f} \approx 4$ MeV . In addition, the fast electron current density can be obtained from,

$$\mathbf{j}_f = e n_f v_f. \tag{2.15}$$

where v_f is approximately the speed of light. This gives $\mathbf{j}_f \approx 1 \times 10^{17}$ Am^{-2}. Furthermore, assuming that the fast electrons propagate as a uniform beam with radius of the laser spot size of FWHM of 5 μm, the fast electron current can be

estimated by multiplying both sides of (2.14) by $e\pi r_{spot}^2$,

$$I_f = \frac{\beta e P_L}{\bar{\epsilon_f}}. \tag{2.16}$$

where r_{spot} is the beam radius, I_f is the total fast electron current, e is electron charge and P_L is the power of the laser ($P_L = \pi r_{spot}^2 I_L$). This would yield $I_f \approx 6$ MA.

2.3.2 Current balance approximation

The electric field growth in time t can be estimated from Maxwell's equation in 1D in vacuum, $E \approx -\mathbf{j}_f t/\epsilon_\circ$. This would give $E \approx 10^{16}$ Vm^{-1} in just 3 ps using the current density value estimated in the previous section. This large electric field is sufficient to halt MeV fast electrons in a timescale of a few femtoseconds and within a few μm of the absorption region [21]. In addition, large self-generated magnetic fields at the surface, which arise due to charge separation, will reverse the flow of the beam and prevent the propagation of fast electrons above the Alfven-Lawson current limit [38, 43, 44],

$$I_A = \frac{4\pi\gamma\beta_s m_e c}{e\mu_0} = 1.7 \times 10^4 \gamma\beta_s \text{ A} \tag{2.17}$$

This implies that the maximum current would be in the kA range, which is lower than the fast electron current in the range of multi-MA current. To demonstrate how the fast electrons are transported into the target, the concept of the current balance approximation is needed [21],

$$\mathbf{j}_f + \mathbf{j}_b \approx 0. \tag{2.18}$$

where $\mathbf{j}_f$ is the fast electron current density and $\mathbf{j}_b$ is the background electron current density. This states that the plasma will supply a background (return) current to limit magnetic field and allow the fast electron beam to propagate. The return

current is provided by target ionisation and will be drawn back by the electric field into the absorption region. The current balance approximation is reasonable for high plasma densities ($n_b \geq 10^{29}$ m^{-3}) as the charge neutrality occurs in $\Delta t \approx 2\pi/\omega_{pe} \approx 10^{-16}$s where $\omega_{pe} \approx 56.4\sqrt{n_b}$ rad.m^{-1} is the plasma frequency. Then the non-neutrality of fast electrons occurs within distance $x \cong c\Delta t \leq 0.1$ μm [45]. However, the current neutralisation must be co-spatial such that the net current density is nearly zero at any point otherwise the self-generated magnetic field, due to current imbalance, would destroy the beam. It is worth mentioning that the number of fast electrons is much less than the number of background electrons as the target electron density far exceeds the electron density at which the laser energy absorbed. As a consequence, the background electron speed is lower compared to the fast electron speed. This has huge consequences for target interaction physics and target heating which is discussed in the following sections.

2.3.3 Collision and resistivity

Dense plasma, if sufficiently cool, is in strongly coupled state. This means that the strength of the plasma particle interactions is very strong and the potential energy is comparable to, or dominates over, the thermal kinetic energy. The strong Coulomb coupling parameter is defined as,

$$\Gamma = \frac{1}{4\pi\epsilon_0}\frac{e^2}{r_s k_B T_e}. \tag{2.19}$$

where ϵ_0 is permittivity, $r_s = (3/4\pi n_i)^{1/3}$ is the interatomic spacing, n_i is the ion density, k_B is the Boltzmann constant and T_e is the electron temperature. The strong Coulomb coupling and small number of particles in a Debye sphere can significantly affect the properties of the system such as the equation of state and the transport processes, since strong collisions and scattering become dominant in this system [6, 7]. As the background current has a much slower velocity than the fast electrons,

it undergoes more energy exchange with the background ions by collisions. Thus, the heating of the target is mainly due to the background current. The background electron-ion collision rate is given by [8],

$$\bar{\nu}_{ei} \simeq 2.91 \times 10^{-6} Z n_b \ln\Lambda \; {T_b}^{-3/2} \; \mathrm{s}^{-1}. \tag{2.20}$$

where n_b and T_b are the background electron density and temperature respectively, $\mathrm{In}\Lambda = \mathrm{In}(\lambda_D/b_{min})$ is the Coulomb logarithm, λ_D is the Debye length and b_{min} is the minimum impact parameter, which is usually the classical electron radius or the half of de-Broglie wavelength at high energy [46]. According to formula (2.20), the collision rate drops with increasing temperature. This can be explained as the temperature increases, the probability of collisions will decrease as the Coulomb cross-section decreases. The background electron collisions have a significant effect on the fast electron transport as demonstrated by Guerin *et al.* [47] as they found numerically, using a PIC code, that the occurrence of collisions limits the mobility of the background electrons and thus they are less able to provide a return current which balances the fast electron current.

With regards to the fast electrons, it is reasonable to assume that they do not strongly collide since their collision mean free path is much greater than the target size. The collisional scattering time of the fast electron can be estimated from [48],

$$\tau_{\mathrm{scatter}} = 60 Z^{-1} \frac{n_b}{10^{29} \; \mathrm{m}^{-3}} \sqrt{\frac{I_L \lambda_L^2}{10^{22} \; \mathrm{Wm}^{-2}}} \; \mathrm{ps} \tag{2.21}$$

where λ_L in μm. This collisional scattering time is longer than the laser pulse duration and in Copper solid density can reach ≈ 20 ps. This assumes that $n_b = 10^{29}$ m^{-3}, $I_L = 10^{24}$ Wm^{-2} with $\lambda_L = 1$ μm.

On the other hand, the resistivity of a material is a measure of the extent to which the background electrons collide with the background ions as they move through

them while carrying a current. It is defined as,

$$\eta = \frac{m_e \bar{\nu}_{ei}}{n_b e^2}, \tag{2.22}$$

Substituting (2.20) into (2.22), the classical Spitzer resistivity is obtained [44],

$$\eta = 1.03 \times 10^{-4} \frac{Z \mathrm{In}\Lambda}{T^{3/2}} \ \Omega.\mathrm{m}. \tag{2.23}$$

The Spitzer relation can be applied when the thermal velocity of the electrons is much greater than the drift velocity, by linearising the momentum equation of the electrons [48]. It is well-known that Spitzer relation overestimates the resistivity by a factor of 100 at solid density and low temperature, leading to larger background heating than may be expected [26, 46]. Therefore, Spitzer resistivity is applicable to high temperature plasmas. An alternative, the Lee and More resistivity model [46] is used in fast electron transport calculations.

2.3.3.1 Lee and More resistivity

Lee and More [46] developed a useful model of resistivity which is applicable across a wide range of densities and temperatures. Their model is based on the Thomas-Fermi ionisation model and does not take into account the effects of atomic structure. The Lee-More calculation of the electron-ion collision rate from the Coulomb logarithm reflects the strong coupling and electron degeneracy effects [6]. Electron degeneracy is a quantum effect that dominates the behaviour of high density plasmas. It occurs due to the de-Broglie wavelength of electrons becoming comparable to the interatomic spacing. Lee-More resistivity takes the following form [46],

$$\eta = \frac{m_e}{n_b e^2 \tau_e} [A^\alpha (\mu / k_B T_e)]^{-1}. \tag{2.24}$$

where n_b is the background electron density, A^α is a coefficient function which depends on the degree of electron degeneracy and this coefficient takes the following

form [26],

$$A^{\alpha}(\mu/k_BT_e) = \frac{4}{3}\frac{F_2}{[1+\exp(-\mu/k_BT_e)](F_{1/2})^2}. \tag{2.25}$$

where μ is the chemical potential, F_2 and $F_{1/2}$ are the Fermi integrals. The electron relaxation time τ_e takes the form,

$$\tau_e \approx 0.6\frac{{m_e}^{1/2}(k_BT_e)^{3/2}}{(Z^*)^2e^4n_i\ln\Lambda_{ei}}[1+\exp(-\mu/k_BT_e)]F_{1/2}. \tag{2.26}$$

where Z^* is the ionisation level and n_i is the ion density. The Lee-More Coulomb logarithm is,

$$\ln\Lambda_{ei} = \max\left(2, \frac{1}{2}\ln[1+\Lambda^2]\right) \tag{2.27}$$

where $\Lambda >> 1$ for weakly coupled plasma. The values of (2.27) for dense plasma is typically in the range 2 to 10 [6, 46].

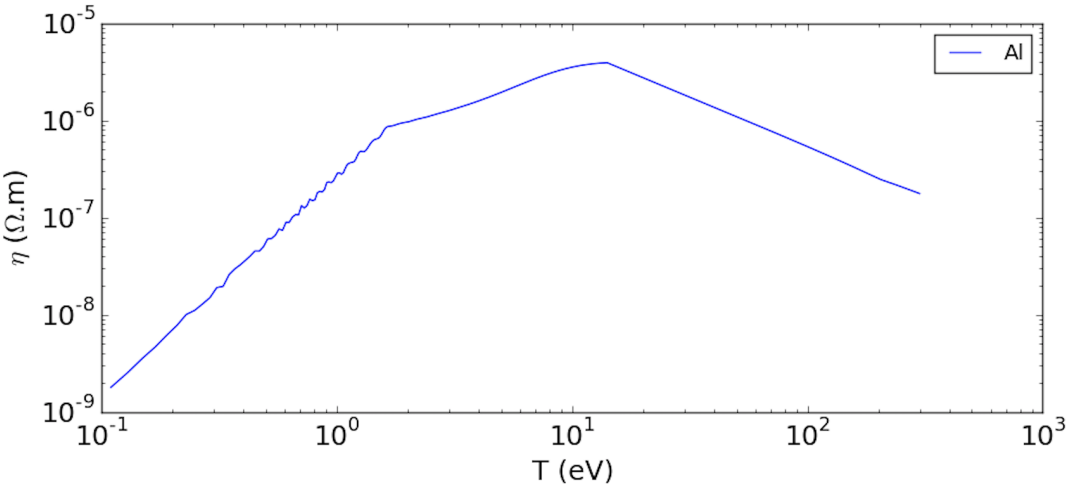

Figure 2.3: Plot of Al resistively ($\Omega.m$) vs temperature (eV) in solid density.

Figure (2.3) shows an example of an Al resistivity curve at solid density that is generated using simple model of the Lee and More. In this simple model, the temperature range is from 0.1 to 300 eV which is divided into 15000 data points in order to observe more details in the curve. The interatomic distance is 1.6×10^{-10} m and the melting temperature is 0.11 eV. The Z^* is determined by a simple Thomas-Fermi ionisation model. As shown, the resistivity reaches a peak as electron

scattering maximises, this is the region of the minimum mean free path (at ≈ 20 eV in the Figure (2.3)) and it displays Spitzer-like resistivity at high temperatures. Notice that the resistivity curve is not accurate at temperature range from 0.1 eV to ≈ 2 eV, i.e. the warm dense matter region. This is due to the fact that the ion-ion correlations effect is not included in the Lee and More model. This effect has a significant impact on the electron collision frequency and mean free path, and thus the resistivity at this region. There are considerable efforts to understand this effect on the resistivity of the materials and attempts to improve the resistivity model for WDM regions, see for example [49–51].

2.3.4 Ohmic heating and drag collisional heating

The background current passing through the plasma resistively heats the plasma. This resistivity is produced by electrons that are driven by the electric field when they collide with ions [52]. This is known as Ohmic heating. The relation between the electric field and resistivity can be obtained from a simplified Ohm's law which ignores the magnetic field,

$$\mathbf{E} = \eta \mathbf{j_b}, \tag{2.28}$$

where $\mathbf{j}_b$ is the background current density. To illustrate how Ohmic heating occurs, the power density per unit volume is given as,

$$P = \mathbf{j}_b \mathbf{E}, \tag{2.29}$$

Using the current balance approximation in both of the equations and substituting (2.28) into (2.29), the Ohmic heating power per unit volume is defined,

$$P_{heat} = \eta \mathbf{j}_f^2, \tag{2.30}$$

Now, the power (or energy density) per unit volume due to the change in the internal energy is given,

$$P = \frac{\partial U}{\partial t} = \frac{3}{2} n_b k_B \frac{\partial T_b}{\partial t}, \tag{2.31}$$

where U is the internal energy. Comparing (2.31) with (2.30), the following relationship is obtained,

$$\frac{\partial T_b}{\partial t} = \frac{2}{3 k_B n_b} \eta \mathbf{j}_f^2. \tag{2.32}$$

This explains that the heating of the target is sensitive to the resistivity of the material. Also, this relationship shows that the Ohmic heating per femtosecond is signifcant, reaching to $\partial T_b/\partial t \approx 4.3$ eVfs^{-1} in the case of fixed resistivity of Cu $\eta_{cu} = 10^{-8}$ Ω.m, $\mathbf{j}_f = 1 \times 10^{17}$ Am^{-2} and $n_b = 10^{29}$ m^{-3}. The influence of the fast electron temperature on the background temperature can be added to (2.32) as follows [53, 54],

$$\frac{\partial T_b}{\partial t} = \frac{2}{3 k_B n_b} \eta \mathbf{j}_b^2 + \frac{n_f}{n_b} \frac{T_f}{\tau_{f-b}}. \tag{2.33}$$

where T_f is the fast electron temperature and τ_{f-b} is the fast-background electron collision time [54],

$$\tau_{f-b} = \frac{3\sqrt{3}}{8\pi} \frac{{m_e}^{1/2} {T_f}^{3/2}}{n_b \, e^4 \, \ln\Lambda} \tag{2.34}$$

The second term in the RHS of (2.33) shows the rate of fast electron energy loss to the background electrons. It should be noticed here that the fast electron temperature does not change significantly with time. This is due to their large mean free path as explained in Section 2.3.3. The fast electron collision time with the background will determine the amount of energy that transfer to the background. Equation (2.33) is known as the "two group" electron model [54].

Drag collisional heating occurs when the fast electrons lose their energy to the background via collisions as they propagate into the solid density target. Their energy is transferred in the form of ionisation, excitation and bremsstrahlung radiation. The contribution of the radiation emission to the target heating can be neglected due to a small absorption cross section of the emitted radiation. The

average collisional energy loss per unit path length [25] is given by the Bethe-Bloch theory [55, 56],

$$\left(\frac{dE}{dx}\right)_{collisions} = \frac{-e^4 n_e}{8\pi\epsilon_0^2 m_e v_f^2} L_d \tag{2.35}$$

where L_d is,

$$L_d = \left[\ln\frac{(\gamma-1)(\gamma^2-1)}{2(J/m_e c^2)^2} + \frac{1}{\gamma^2} - \frac{2\gamma-1}{\gamma^2}\ln 2 + \frac{1}{8}\frac{(\gamma-1)^2}{\gamma^2}\right] \tag{2.36}$$

and J is the mean ionisation potential. The rate of change in the temperature of the target due to this heating is,

$$C_v\left(\frac{\partial T_b}{\partial t}\right)_{collision} = \left\langle \frac{\mathbf{j}_f}{e}\left(\frac{dE}{dx}\right)_{collisions}\right\rangle \tag{2.37}$$

where C_v is the volumetric specific heat capacity. As shown from (2.32) and (2.37), the Ohmic heating and the collisional heating scales as $\mathbf{j}_f^2$ and $\mathbf{j}_f$ respectively.

2.3.5 The resistive magnetic field generation

The concept of current balance approximation assumes that the background electrons respond immediately to the fast electrons. This is an important assumption for understanding the generation of resistive magnetic fields. The fourth Maxwell equation shows that the current densities of the background electrons and the fast electrons produce a magnetic field as follows,

$$\nabla \times \mathbf{B} = \mu_\circ(\mathbf{j}_b + \mathbf{j}_f), \tag{2.38}$$

The cancellation of the fast electron current by the background current is clear if one assumes that $\mathbf{j}_b + \mathbf{j}_f = 0$. Thus $\mathbf{j}_b + \mathbf{j}_f = (\nabla \times \mathbf{B})/\mu_\circ = 0$.

If this is not the case, the effect of resistivity is included in this model by multi-

plying both sides of the equation by η and using the simple form of Ohm's law [57],

$$\eta \nabla \times \mathbf{B} = \mu_\circ(\mathbf{E} + \eta \mathbf{j}_f), \tag{2.39}$$

$$\mathbf{E} = -\eta \mathbf{j}_f + \frac{\eta}{\mu_\circ} \nabla \times \mathbf{B}, \tag{2.40}$$

Equation (2.40) shows that the generated electric field opposes the fast electron current density. Substituting (2.40) into the second Maxwell equation yields the magnetic field,

$$\frac{\partial \mathbf{B}}{\partial t} = -\nabla \times \mathbf{E}, \tag{2.41}$$

$$\frac{\partial \mathbf{B}}{\partial t} = (\nabla \times \eta \mathbf{j}_f) - \nabla \times (\frac{\eta}{\mu_\circ} \nabla \times \mathbf{B}), \tag{2.42}$$

The first term in (2.42) explains how an azimuthal magnetic field is generated, which is the key element of the work covered in Chapter 5 of this thesis. The second term shows the resistive diffusion of the magnetic field, which is usually neglected. The reason for this is that at high temperatures, this diffusion is small during the laser pulse duration. This reduces (2.42) to,

$$\frac{\partial \mathbf{B}}{\partial t} = (\nabla \times \eta \mathbf{j}_f), \tag{2.43}$$

$$\frac{\partial \mathbf{B}}{\partial t} = \eta(\nabla \times \mathbf{j}_f) + (\nabla \eta) \times \mathbf{j}_f. \tag{2.44}$$

This azimuthal magnetic field if sufficiently strong can collimate fast electrons. The growth of the magnetic field can be estimated from (2.43). It yields 100 T in 1 ps if the radius of the beam is 10 μm, $\eta_{cu} = 10^{-8}$ Ω.m and $\mathbf{j}_f = 1 \times 10^{17}$ Am^{-2} . Each term of the (2.44) has a role in the generation of the magnetic field as follows:

The term $\eta(\nabla \times \mathbf{j}_f)$ implies that the generated magnetic field forces fast electrons towards higher fast electron current-density regions. The magnetic field develops due to the spatial variation in the current density. As the fast electron current beam density is highest on the target axis, the resulting radial force leads to the

self-pinching of the fast electron beam [58]. In a plasma with Spitzer resistivity, self-pinching occurs if the ratio of the radius of the beam R to the Larmor radius of the fast electrons $\mathbf{r}_g = \gamma m_e v_f / e\mathbf{B}$ is greater than the square of the half-divergence angle $R/r_g > \theta_d^2$ [59]. By substituting the Larmor radius into the relation $R/r_g > \theta_d^2$ collimation parameter is obtained,

$$\Gamma_{\mathrm{Col}} = \frac{eRB(t)}{\gamma m_e v_f \theta_d^2}. \tag{2.45}$$

Collimation occurs when Γ_{Col} is greater than 1. In addition, the radial force can act on the small variations within the beam, resulting in breakup of the beam into filaments [38]. This is discussed in the next section.

The term $(\nabla\eta)\times\mathbf{j}_f$ on the RHS of (2.44) implies that the generated magnetic field forces the fast electrons towards higher resistivity regions. This term results in the Ohmic heating of the target. Assuming that the fast electron beam has a Gaussian profile, the Ohmic heating is higher in the centre of the beam. This leads to a large degree of Ohmic heating along the target axis. Therefore, it can be excepted that the resistivity is lower along the beam axis compared to transversely across the target. This could lead to hollowing of the electron beam [51]. The structured resistive guiding target [60] exploits the second RHS term to collimate the fast electrons by designing targets with tailored resistivity. The theory of resistive-guiding targets is discussed in Chapter 5, where we examine the effect of grading the atomic number Z at the interface of a guiding structure on fast electron guide heating.

2.3.6 Transport instabilities and filaments

From Sections 2.3.3 and 2.3.5, it can be argued that the transport of fast electrons is controlled more by the electric and magnetic fields than by the collisions. This can be seen from the effects of three different beam-plasma instabilities on fast electrons transport. These instabilities are the Weibel [61], the two-steam [52] and

the filamentation instabilities [24,62]. They are classified according to their unstable wave vector's **k** directions with respect to the fast electron beam and to the electric field as shown in Figure 2.4 [39, 62].

The Weibel instability depends on a the background temperature. If the background temperature is high, the growth rate aligns with high-order modes of the instability, resulting in small-scale filaments on a spatial scale of the order of skin depth c/ω_{pe}. If the background temperature is low, however, this can align the growth with low-order modes, resulting in a small number of larger filaments [39].

Both two-stream and filamentation instabilities depend on the fast electron beam density and are found on the same dispersion relation branch. However, the fast-growing mode is intermediate between the two and is known as TSF mode, where "TSF" stands for Two-Stream and Filamentation [62]. This is given as,

$$\gamma_{TSE} = \frac{\sqrt{3}}{2^{4/3}} \left(\frac{\alpha_n}{\gamma} \right)^{1/3} \omega_{pe} \tag{2.46}$$

where $\alpha_n = n_f/n_b$, $\gamma = 1/\sqrt{1-(v/c)^2}$ which is the Lorentz factor associated with the fast electron velocity; and ω_{pe} is the plasma frequency. This process produces density perturbations and filaments [63].

In reality, the fast electron beam experiences all these instabilities at the same time. The most unstable process mainly shapes the beam while the other instabilities start to grow exponentially [62]. The main evolution of the transport instabilities has been observed as the splitting of the fast electron beam into filaments. Filamentation onset is when there is a small fluctuation in the transverse magnetic field. The magnetic term in the Lorentz force $-ev \times B$ bends the oppositely directed beams towards spatially different points. This produces a nonzero current that induces the magnetic field, concentrating the current density. This evolves ultimately into a filament [39, 64].

Experimentally, a number of diagnostic approaches have been employed in order to investigate these filaments. For example, Storm *et al.* [65] used a spatially-resolved

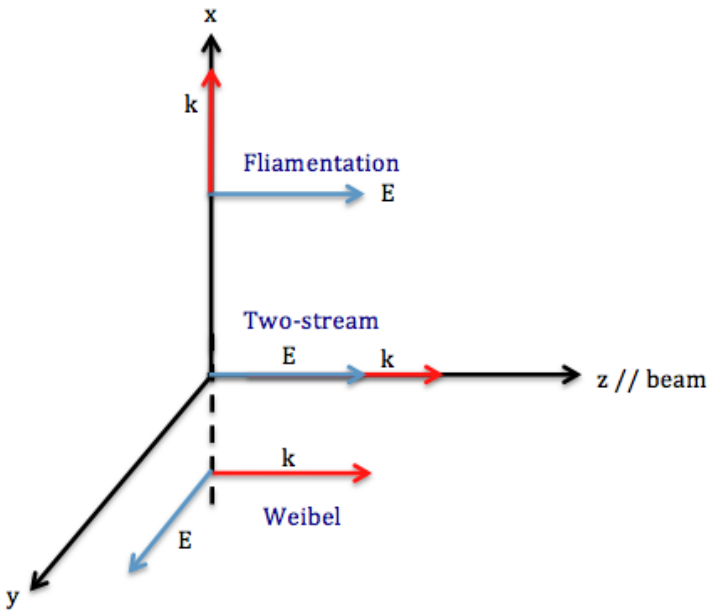

Figure 2.4: The Weibel, two-steam and flimanetation modes.

coherent transition radiation (CTR) imaging technique. The CTR is emitted when the beam crosses the rear surface of a target and is imaged using a scientific-grade CCD camera. The images contain small-scale structures indicating the presence of filaments. Another example of a different diagnostic approach is that of proton emission [66]. This emission is from the rear surface of the target and is detected and imaged using a stack of radiochromic films (RCF) placed behind the target. All these diagnostic approaches indicate that filaments occurs in both conductive and insulating materials. The growth of filaments inside of the target implies that the target is being strongly heated non-uniformly. However, non-uniform heating is not desirable in most situations. This is the case in the hydrodynamics experiments as explained in Chapter 6.

2.3.7 Fast electron heating literature review

Fast electron beam transport and its consequences on target heating across the target depth is of interest. Ohmic resistive heating and drag collisional heating depend on the ability of the fast electrons to penetrate the target. However, both

collisions and electric fields can slow down fast electron penetration which reduces the heating across the target depth. The reduction in heating has been experimentally observed in [19,67] as temperature gradients across the target depth. Volpe *et al.* [68] have shown experimentally that the electric field effect becomes important at intensities of the order of 10^{17} Wcm^{-2} depending on the material while it is dominant over the collisional process at intensities of the order of 10^{19} Wcm^{-2}. The effect of electric fields on penetration was experimentally observed by Key *et al.* [69] who noted a strong reduction in fast electron penetration and heating on a CH target. They attributed this to electric field inhibition, a phenomenon first proposed by Bell *et al.* [21]. Pisani *et al.* found [70] experimentally clear evidence of this inhibition in a CH target (insulator) compared to an Al target (metal). A CH target, which has high resistivity, needs to be initially ionised to provide a return current, while in an Al target, where resistivity is low, the return current is established by the free electrons. In addition, Pisani *et al.* [70] also compared between the electric field inhibition and collisional effect using a Monte Carlo code, which takes into account only the collisions. It was found that the experimental fast electron penetration in CH target was shorter than predicted by the code while an agreement is obtained in case of Al target. The results of this experiment showed the adverse impact of electric field on fast electron penetration.

A large angular spread is another effect which reduces penetration and this has been explored in many experimental studies, for example see [22,23,71]. The increase of the angular spread is due to several complex mechanisms and it increases with increasing the transverse dimension of the target. The use of large transverse plane in targets to more than 50 μm is unavoidable due to the limited pointing stability [72]. The adverse effect of angular spread on penetration led [60] to propose the use of resistive magnetic fields [73] to collimate the beam with a resistive guide. Although the resistive guide idea has mainly been proposed in the case of Fast Ignition, it recently becomes of interest to improve the heating of extended targets for the sake

of hydrodynamic experiments [74, 75].

Fast electron refluxing mechanism can improve the heating in a target that has a finite depth, i.e. a few tens of microns, [28] and as a result isochoric heating can be obtained [76]. This mechanism can transfer $\approx 90\%$ of the fast electron energy into the thermal plasma before any hydrodynamic disassembly [77]. The difficulty of heating increases with increasing target depth as the resistivity evolution at low temperature can lead to annular transport as shown by MacLellan *et al.* [51]. Filamentation instabilities [24, 62] also spoil the heating with depth, especially when the thicker target has large transverse directions and is heated with a pulse of a few ps.

On the other hand, there has been recent debate concerning the main fast electron heating mechanism. The numerical work of Kemp *et al.* [78] in 2006 shows that fast electron energy transfers at solid density by Ohmic resistive heating followed by diffusion and drag collision between the fast electrons and the background electrons. However, Sherlock *et al.* [20] using a PIC code found that large amplitude of plasma waves induced by the fast electrons is another important source of heating. The collisional damping of these waves significantly heats the background plasma and the heating rate exceeds the Ohmic resistive heating by a factor of ≈ 3. The work in this thesis does not take into account this newly discovered source of heating.

2.4 Fast electron transport code: ZEPHYROS

ZEPHYROS is a 3D Cartesian-grid, particle-hybrid code developed by A. P. L. Robinson. The hybrid approximation in the context of fast electron transport means that a distinct population of electrons, i.e. fast electrons, is treated kinetically, while a distinct population of background electrons is treated as a fluid. Splitting the population of the fast electrons and the background electrons is a reasonable approximation for two reasons. Firstly, the number of fast electrons is much less than the number of background electrons $n_f << n_b$. Secondly, the mean energy of the fast

electrons is much greater than the mean energy of the background electrons [27]. This split serves to simplify the numerical simulation, as otherwise the disparate lengths and time scales between the fast and background electrons would make the system computationally expensive. To handle difference in scale between the fast electrons and background electrons, such as in temperature, density, mean free path, a hybrid approximation is employed. This allows the use of larger time-steps and cell sizes, which are computationally efficient.

Fast electron kinetics can be described using the Fokker-Planck equation [27],

$$\frac{\partial f}{\partial t} + \mathbf{v}.\frac{\partial f}{\partial \mathbf{x}} - e(\mathbf{E} + \mathbf{v} \times \mathbf{B}).\frac{\partial f}{\partial \mathbf{p}} = (\frac{\partial f}{\partial t})_{\text{collisions}} \tag{2.47}$$

where $f = f(\mathbf{x}, \mathbf{p}, t)$ is fast electron distribution and $\mathbf{x}$ and $\mathbf{p}$ are the phase-space position and momentum respectively. This equation is solved using standard PIC methods, except the collisional term on the RHS is treated using Monte-Carlo methods but with the collisional term operator includes angular scattering and drag (energy loss through collisions) due to the background electrons and ions [27, 57, 79]. The background electron motion is ignored in the kinetic treatment, as the speed of the fast electrons is much greater than the mean speed of the background plasma.

The hybrid code is based on an "Ohmic approximation" since the electric and magnetic fields are resistively generated. Also, it uses a reduced form of Maxwell's equations (see Sections 2.3.4 and 2.3.5). The magnetic field is given by the induction equation (2.42). The electric field is obtained by substituting Ohm's law into the Ampere-Maxwell equation, ignoring the displacement current to give (2.40). Ignoring displacement current relies on the assumption that the change in the electric field, $\partial \mathbf{E}/\partial t$, is slow. Indeed, comparing the electric field and magnetic field terms, in the Ampere-Maxwell equation, using dimensional analysis gives,

$$c^2 \nabla \times \mathbf{B} = \frac{\mathbf{j}}{\epsilon_0} + \frac{\partial \mathbf{E}}{\partial t} \tag{2.48}$$

$$\frac{\partial \mathbf{E}/\partial t}{c^2 \nabla \times \mathbf{B}} \approx \frac{\eta \mathbf{j}/\tau_L}{c^2 \eta \mathbf{j} \tau_L / L^2} \approx \frac{L^2}{c^2 \tau_L^2} \tag{2.49}$$

where L is the beam width and τ_L is the laser pulse duration. Thus, the assumption of ignoring the displacement current is valid if $L << c\tau_L$. This assumption excludes electromagnetic phenomena, for example modelling the laser pulse.

The background plasma is treated as a static fluid. This fluid is subject to heating, ionisation and change in resistivity. The background plasma heating evolves due to Ohmic heating (Section 2.3.4) and collisional drag, and both are included into the background electron energy equation. The resistivity is temperature dependent and based on that of Lee-More resistivity (Section 2.3.3.1). In the Lee-More resistivity model in ZEPHYROS, the Fermi integrals are constant terms and the chemical potential is calculated using the Thomas-Fermi ionisation model.

Hybrid codes rely on current balance approximation, as discussed in Section 2.3.2. Therefore, the response of the background fluid to the fast electrons ensures quasi-current neutrality. The interaction between the background electrons and fast electrons is via collisions and electromagnetic fields. ZEPHYROS is a powerful tool as it allows a lot of the features of physics to be included. Among the features used in this thesis is a simple model of bremsstrahlung emission. This allows the background to cool down under the assumption of the optically thin plasma. More details on using the different features can be found in Ref. [74, 80].

As the laser pulse is not modelled in ZEPHYROS, the fast electrons are injected via energy dump transversely over the laser spot of a few cells' depth as a Gaussian profile. The energy at this region promotes electrons from the fluid into fast electrons (treated as macroparticles). If macroparticles fall below about $5 - 10$ keV then they are reabsorbed into the background electrons. However, neither the promotion nor the absorption process is dependent on the background temperature. The fast electrons move and interpolate to a computational grid, obtaining current density and evolving electric and magnetic fields. The distribution of the fast electron energy

is given as,

$$f(E) = \exp\left[-\frac{E}{T_f}\right]. \tag{2.50}$$

where T_f the fast electron temperature as determined by the reduced Wilks scaling (2.13). In this thesis, all the fast electron transport calculations are performed using ZEPHYROS.

2.5 Summary

This chapter provides an introduction to fast electron transport and its properties which are given after a brief review of the petawatt laser and fast electron generation. The current balance approximation, Ohmic heating, resistive magnetic field generation and transport instabilities are discussed. The physics of the hybrid ZEPHYROS code used in this thesis to study the fast electron transport is also outline. More details on fast electron transport can be found in the recently published topics review [25, 27].

Chapter 3

Rayleigh-Taylor instability and Radiative losses

This chapter presents an overview of some of the areas of physics relating to the work of Chapter 6, which concerns a computational investigation of a Rayleigh-Taylor (RT) instability experiment driven in a fast-electron-heated target. As stated in Section (2.1), the interaction time between the target and the short-pulse laser is faster than hydrodynamic timescales. After the end of heating, the plasma pressure leads to expansion. With suitable target materials, it is possible to arrange this expansion to drive the RT instability. The RT instability is of great significance in laser-plasma interactions as it has implications for degrading the performance of compression of the capsules in inertial confinement fusion (ICF) [81]. It is also the subject of ongoing research in astrophysics, since it occurs in certain astrophysical objects such as young supernova remnants [82].

In this Chapter, section 3.1 introduces RT instability and gives a brief review of literature on its effect in laser-plasma interactions. This is followed by an analytical derivation of the RT growth rate formula as used in laser-plasma interaction studies. Then section 3.2 discusses some of the physics of radiation losses, including material opacity and radiative cooling rate. Finally, section 3.3 describes the physics of the standard laser-plasma hydrodynamic code, followed by description of the 1D

hydrodynamic HYADES and HELIOS codes.

3.1 Rayleigh-Taylor instabilities

The Rayleigh-Taylor (RT) instability [83,84] is a fluid instability which occurs at the interface between two fluids, when a high-pressure, low-density fluid accelerates a lower-pressure, higher-density fluid. This can also occur in plasmas and is of particular interest at high-energy-density [12]. Perturbations at material interfaces are susceptible to RT instability growth if the following condition is present,

$$\nabla P \bullet \nabla \rho < 0 \tag{3.1}$$

This implies that the pressure P and density ρ gradients are of the opposite sign. As an example of this (3.1) condition, Figure 3.1 shows pressure (left axis, solid curve) and density (right axis, dashed curve) profiles at the interface (red-solid line) between two plasmas. Here, the gradients in pressure and density across the interface are opposite in direction. If the interface is structured with small amplitude perturbations, the amplitudes of these perturbations will grow. Spikes of dense material will penetrate into the lower-density plasma, and while the lower-density plasma will grow as bubbles into the higher-density plasma [6].

It is often convenient to describe the interface surface of the perturbations as a Fourier series of the sum of a large number of sinusoidal modes. A standard treatment of linear theory for single-mode sinusoidal perturbations is considered in this thesis; a review of which was given by Sharp [16]. The linear theory of RT for the growth of small single-mode perturbations at the interface between two incompressible fluids can be expressed as [83, 85],

$$\frac{d^2\zeta(t)}{dt^2} - \gamma_{RT}^2 \zeta(t) = 0 \tag{3.2}$$

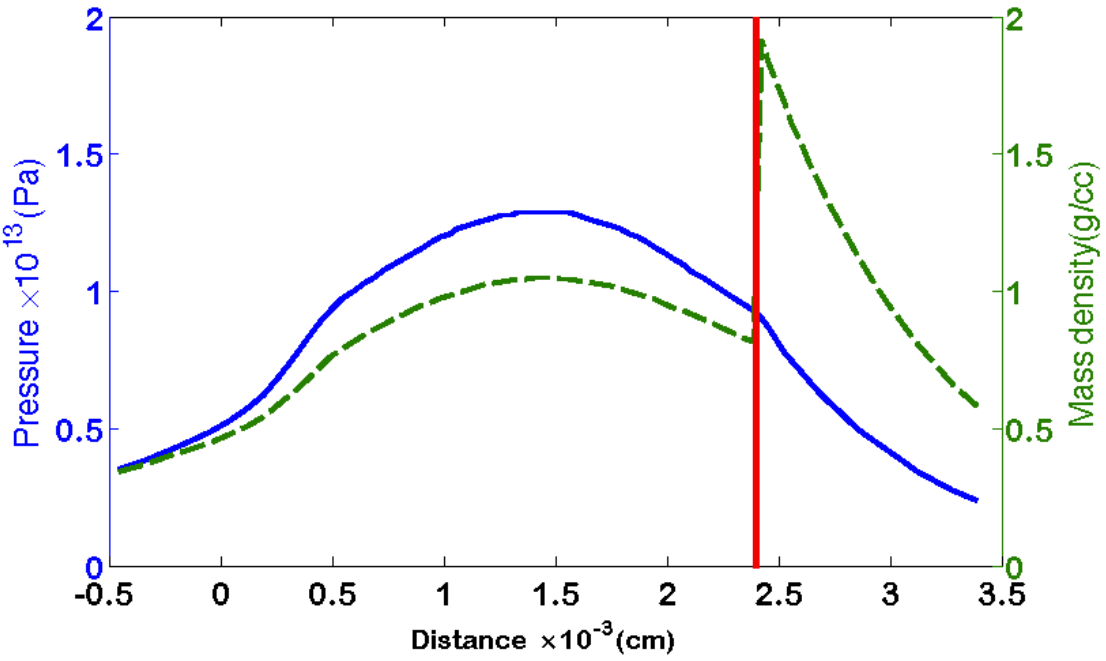

Figure 3.1: Sample pressure (left axis, solid curve) and density (right axis, dashed curve) profiles versus position of two-plasmas of different Z subjected to RT instability from HELIOS simulation. The red-solid line indicates the interface between the two different Z materials. The gradients of pressure and density across the interface are opposite in direction, so at this interface the amplitudes of the perturbations are susceptible to growth.

where ζ is the spatial amplitude of the single-mode of the perturbation and γ_{RT} is the growth rate of this perturbation. In the linear theory, the growth of perturbations exponentially increases with time from their initial amplitudes ζ_0 which are assumed much less than the wavelength of the perturbations ($\zeta_0 \ll \lambda$). When the amplitude of the growing perturbations becomes comparable to the wavelength, the growth starts to slow down and the sinusoidal perturbations become asymmetric [12]. This is the weakly non-linear stage which will not be investigated here.

In the next two subsections, a brief literature review of RT instability in laser-plasma interaction is given. Then the analytical derivation of the RT growth rate formula is discussed in a configuration similar to target used in the laser-plasma experiment to seed RT instability.

3.1.1 Rayleigh-Taylor instability in laser-plasma interaction

The RT instability was named after work by Rayleigh [83] and later Taylor [84]. Rayleigh considered only the effect of the gravitational field, whereas Taylor added the acceleration induced by a pressure gradient, and they both studied this instability in a linear regime. The RT instability has been excellently reviewed by Kull (1991) [86]. This review presents a theoretical study of the RT instability based on potential flow theory for plane and spherical geometries under various conditions. Haan (1991) [87] studied the coupling modes theoretically using the perturbation theory solution and stated that the coupling leads to bubbles and spikes. Haan's model is only valid during early weakly nonlinear RT instability. A study of coupling mode of weakly nonlinear the RT instability is also performed by Ofer *et al*. (1992) [88] using a 2D hydrodynamic code. They found that mode-mode interaction affects the amount of mixing.

In the context of high-power laser laboratories, the RT instability can be driven at very short time scales. For example, a long-pulse high-power laser depositing its energy in a small region of the target will create low-density and high-pressure plasma at the front of the target. This plasma is directly next to and accelerating a high-density and low-pressure plasma. The RT instability growth arises as the low-density plasma starts to push the high-density plasma. The required time for the amplitude of the perturbed interface between the two plasmas to increase by a factor of e (e-folding growth time) is [86],

$$\tau_{e-folding} = \sqrt{\frac{\lambda}{2\pi g}} \approx 1ns \tag{3.3}$$

where it is assumed that the wavelength of the perturbation λ is 100 μm and $g = 10^{15}$ cms^{-2} [34]. The classical RT growth rate is inversely proportional to (3.3), i.e. $\gamma_{RT} \propto 1/\tau_{e-folding}$. This formula suggests that for the small perturbations, a short wavelength grows more rapidly than a long one. The effect of a continuous

density gradient was added by Lelevier *et al.* (1955) [89] and subsequently other physical effects have been included in RT studies depending on the conditions and circumstances that lead to the RT instability. For example, the process of material ablation reduces the growth rate. This is discussed by Bodner (1974) [90] and described by the Takabe formula (1985) [91].

The design of the RT experiment changes depending on the main purpose of the investigation, for example whether the focus is on the ICF aspects or on astrophysical objects. In all cases, however, these experiments are challenging as the time scale of RT production is short and during this time measurement of the perturbation growth needs recording [16]. The first clear experimental evidence of RT instability using laser-driven targets was obtained in 1982 by Cole *et al.* [92]. In this experiment, an Al target of 3 μm thickness was shot by three laser beams with 32 J and 1.2 ns of pulse duration. An initial ripple of wavelength 20 μm and amplitude 0.5 μm was machined at the surface of the target. A Cu target was set behind the Al target and irradiated by another laser beam to create an X-ray backlighter beam. The experiment showed that the average growth rate is lower than both the classical and simulated values. However, the lack of high resolution made it difficult to determine the real reason for this reduction [12, 92].

Of particular importance is the adverse effect of RT instability on the symmetric compression of a spherical target in inertial confinement fusion (ICF) (see e.g. Lindl [81]). The initial perturbations are seeded either by manufacturing defects of the outer surface of the spherical target, by the laser or radiation non-uniformities in "direct" and "indirect" drive approaches respectively. Two types of RT instability occur in ICF. The first type is the "ablative RT" instability, which occurs at the early stage of the interaction, i.e. acceleration phase, at the target surface where part of the heated material is ablated away. The second type is the "classical RT " instability, which occurs at the inner surface of the spherical target when it is being decelerated late in time by the hot, but relatively low density, spot (deceleration

phase). Nuckolls and Wood (1972) [93] predicted that the heated ablated material in ablative RT instability will remove a significant fraction of the perturbations. However, their model proved to be optimistic, as the first numerical investigation performed by Lindl and Mead (1975) [94] showed that the growth rate is much higher than Nuckolls and Wood's prediction. Lindl (1995) [81] describes the RT instability in context of indirect drive ICF. In 1996, Budil *et al.* [95] conducted the first experiment to directly observe and compare these two different types of RT instability, i.e. ablative and classical RT, in a planar and indirect dirve geometries. Two different target designs were used for each type of instability. The first was similar in configuration to that of Cole *et al.* [92] for ablative RT, while the second was similar to the configuration in Figure 3.2 for classical RT. Both targets were irradiated by identical radiation source whilst different perturbation wavelengths were tested. The measurement of the growth factors showed that the ablative RT growth rate is lower than the classical growth due to the fact that the heated materials ablate away from the target surface. The velocity of the ablated material is of the order of 10^5 cms^{-1} with the results described by Takabe [91]

$$\gamma_{RT} = \pm\sqrt{(\frac{A_t kg}{1+kL})} - \beta_{ablate} k v_a. \tag{3.4}$$

where A_t is Atwood number, k is the wave number and L is the density scale length. These parameters are discussed in the next section. Here β_{ablate} is an adjustable factor which depends on the details of the investigation and v_a is the ablation velocity. The influence of a finite target thickness in these experiments is negligible. Betti *et al.* (1998) [96] estimated the growth rate of ablative RT instability by including the effects of thermal conduction and the Froude number (a dimensionless number gives the ratio of ablation velocity to the product of acceleration and ablation front thickness). They estimated two expressions for ablative RT growth, one for a large Froude number and one for a small Froude number. In 2000, Lobatchev and Betti [97] showed that the RT instability in the deceleration phase is not a pure

classical phenomenon as mass ablation from the spherical target's inner surface significantly reduces the classical RT growth rate. This mass ablation is caused by the heat flux from the hot spot towards the inner surface. They estimated the ablation velocity using standard hot-spot parameters and found this to be of the order of 17 μmns^{-1} for typical direct-drive National Ignition Facility (NIF) target. Martinez *et al.* (2015) [98] successfully managed to image the non-linear bubble-merger regime at the ablation front for the first time in an indirect drive experiment at NIF. Furthermore, The RT induced magnetic field is currently an ongoing topic of investigation, see e.g. [99, 100]. The gradients in temperature and density created by RT growth instability generate magnetic fields near the unstable interface. The strength of these fields depends on the hydrodynamic conditions and on the plasmas.

The presence of the RT instability in a short-pulse high intensity laser-solid experiments system was identified by Lancaster *et al.* in 2009 [67]. This experiment was designed to study electron transport by measuring the longitudinal temperature gradient using a transverse optical shadowgraphy. Bi-layered targets were used, e.g. a CH-Cu target, where the Cu layer use for Cu K_α imaging. To explain the results, it was necessary to include RT in the analysis. It was found that the 1 μm of Cu can rapidly cool by radiation emission dropping its pressure and then be pushed by the lower-Z CH materials. The influence of the RT effect was inferred from the temperature measurement. Without including the RT effect into the temperature calculation, the CH temperature was unrealistically high by a factor of 2 or 3 and did not agree with other published temperature data [19,101]. The emergence of the RT instability was unexpected. These findings led Rossall *et al.* [4] to develop an experiment to specifically drive the RT instability in a fast electron heated target. This experiment is computationally studied in Chapter 6.

3.1.2 The analytical derivation of RT growth rate

The growth rate formula for the classical RT instability in the case of finite depths for two fluids is derived following the procedure in Landau and Liftshitz [102]. Figure 3.2 shows the sketch of a heavier fluid, with density ρ_h and depth h_h, which is supported by a lighter fluid, with density ρ_l and depth h_l, in accelerating field $\mathbf{g}$. The interface between the two fluids along the x-axis has a sinusoidal perturbation of amplitude $z = \zeta(x,t)$. Assume the following conditions to simplify this complex situation,

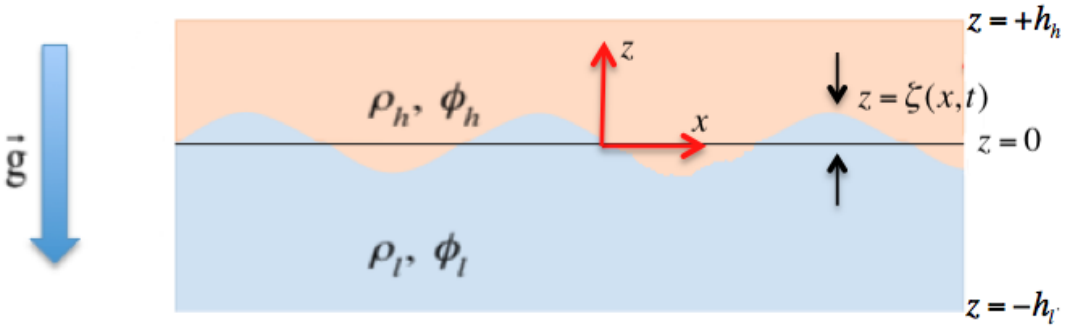

Figure 3.2: Schematic of heavier fluid, with density ρ_h, sits on the top of the lighter fluid, with density ρ_l. Both fluids have finite depth denoted as h_h and h_l. A sinusoidal perturbation along the x-axis, given by $z = \zeta(x,t)$, has been introduced at the interface between the two fluids.

1. Both fluids are incompressible, which means the density is constant. This assumption reduces the mass continuity equation to $\nabla.\mathbf{u} = 0$, where $\mathbf{u}$ is the fluid velocity, which implies that the volume of both fluids is constant.

2. The flow in both fluids is irrotational, i.e. $\nabla \times \mathbf{u} = 0$. Thus, the velocity can be represented as $\mathbf{u} = \nabla\phi$, where ϕ is the velocity potential. Since it is assumed that the fluids are also incompressible, the continuity equation $\nabla.\mathbf{u} = 0$ will satisfy the Laplace equation,

$$\nabla^2\phi = 0. \tag{3.5}$$

3. The upper heavy fluid boundary at $z = +h_h$ and the lower lighter fluid bound-

ary at $z = -h_l$ are stationary at their surfaces. These conditions at the boundary are essential to solve (3.5). The boundary conditions can be expressed as,

$$\frac{\partial \phi_h}{\partial z} = 0 \quad \text{at} \quad z = +h_h \tag{3.6}$$

$$\frac{\partial \phi_l}{\partial z} = 0 \quad \text{at} \quad z = -h_l \tag{3.7}$$

4. As the flow is incompressible and irrotational, the linearised momentum equation, including the term of the accelerating field in 1D, can be written after the integration as,

$$P = -\rho \frac{\partial \phi}{\partial t} - \rho g z \tag{3.8}$$

where P is the fluid pressure.

5. At the interface where $z = \zeta(x, t)$, the pressure must be continuous across the interface (i.e. $P_l = P_h$). So (3.8) is written as,

$$\rho_h \frac{\partial \phi_h}{\partial t} + \rho_h g \zeta = \rho_l \frac{\partial \phi_l}{\partial t} + \rho_l g \zeta \tag{3.9}$$

6. Assuming the perturbation ζ is small at the interface, i.e. $\zeta << \lambda$, it is possible to assume that the vertical component of the velocity u_z at the interface where $z = \zeta(x, t)$ is simply the time derivative of this perturbation. This implies,

$$u_z = \frac{\partial \phi_{l,h}}{\partial z} = \frac{\partial \zeta}{\partial t} \quad \text{at} \quad z = \zeta \tag{3.10}$$

7. Finally, the fluid velocities must be the same for each fluid at the interface position at $z = 0$,

$$\frac{\partial \phi_h}{\partial z} = \frac{\partial \phi_l}{\partial z} \tag{3.11}$$

Using these conditions, the stability of the interface between the two fluids can be estimated as follows. The separable solution to (3.5) of the form of propagating

wave along x-axis is,

$$\phi = f(z)\cos(kx - wt) \tag{3.12}$$

where w is the frequency of the wave, $k = 2\pi/\lambda$ is the wave number, λ is the wavelength of the sinusoidal perturbation and $f(z)$ is the function determining the variation of the velocity of the wave with depth. Substituting (3.12) into (3.5), gives,

$$\frac{d^2 f(z)}{dz^2} - k^2 f(z) = 0 \tag{3.13}$$

The solution of (3.13) is,

$$f(z) = Ae^{kz} + Be^{-kz} \tag{3.14}$$

where A and B are constants. Substitution of this solution into (3.12) gives the following general solution for the velocity potential,

$$\phi = (Ae^{kz} + Be^{-kz})\cos(kx - wt) \tag{3.15}$$

This solution has to satisfy the boundary conditions defined in (3.6) and (3.7) for heavier fluid and lighter fluid. This leads to re-writing (3.15) as,

$$\phi_h = C_1 \cosh k(z - h_h)\cos(kx - wt) \tag{3.16}$$

$$\phi_l = C_2 \cosh k(z + h_l)\cos(kx - wt) \tag{3.17}$$

where ϕ_h and ϕ_l is the solution of the heavier fluid and lighter fluid and C_1 and C_2 are new constants with following values $2Ae^{kh_l}$ and $2Ae^{-kh_h}$ respectively. Applying the conditions (3.10) and (3.11) into (3.9) gives,

$$(\rho_l - \rho_h)g\frac{\partial \phi_l}{\partial z} = \rho_h \frac{\partial^2 \phi_h}{\partial t^2} - \rho_l \frac{\partial^2 \phi_l}{\partial t^2} \tag{3.18}$$

Substituting both (3.16) and (3.17) into (3.18) and (3.11) gives two linear equations,

$$\omega^2 = \frac{kg(\rho_l - \rho_h)C_2 \sinh(kh_l)}{\rho_l C_2 \cosh(kh_l) - \rho_h C_1 \cosh(kh_h)} \tag{3.19}$$

$$C_2 \sinh(kh_l) = -C_1 \sinh(kh_h) \tag{3.20}$$

Multiplying both the numerator and denominator in (3.19) by $(C_2 \sinh(kh_l))^{-1}$ and then using (3.20), the dispersion relation that describes the stability of the interface between the two fluids is,

$$\omega^2 = \frac{(\rho_l - \rho_h)kg}{\rho_l \coth(kh_l) + \rho_h \coth(kh_h)} \tag{3.21}$$

As shown in Figure 3.2 the lighter fluid accelerates the heavier fluid so the initial perturbations will grow. Multiplying both numerator and denominator of (3.21) by $\rho_h + \rho_l$ and then taking the square root, the rate of this growth is,

$$\gamma_{RT} = \pm\sqrt{A_t kgf} \tag{3.22}$$

where where $A_t = (\rho_h - \rho_l)/(\rho_h + \rho_l)$ is the Atwood number and f a fluid factor which accounts for the finite thickness of materials,

$$f = \frac{(\rho_h + \rho_l)}{\rho_l \coth(kh_l) + \rho_h \coth(kh_h)} \tag{3.23}$$

In the laser-produced plasma context, a planar target has a configuration similar to Figure 3.2, however the situation is more complex as the target is subject to expansion leading to a density gradient at the interface. This expansion can reduce this growth as illustrated in Figure 3.3. The density gradient scale length L is defined [85],

$$L = \frac{\rho_{avg}}{|(\frac{\partial \rho_{avg}}{\partial z})|} = \rho_{avg}|\frac{\partial z}{\partial \rho_{avg}}| \tag{3.24}$$

where ρ_{avg} is the density at the interface. Thus the density is reduced by a factor of e^{-kL}. Using Taylor expansion on this factor and ignoring higher orders terms gives,

$$e^{-kL} = \frac{1}{(1+kL)} \quad \text{for} \quad kL << 1 \tag{3.25}$$

Including (3.25) into (3.21) with re-arrangment gives the growth rate γ_{RT},

$$\gamma_{RT} = \pm\sqrt{\left(\frac{A_t kg}{1+kL}\right) f} \tag{3.26}$$

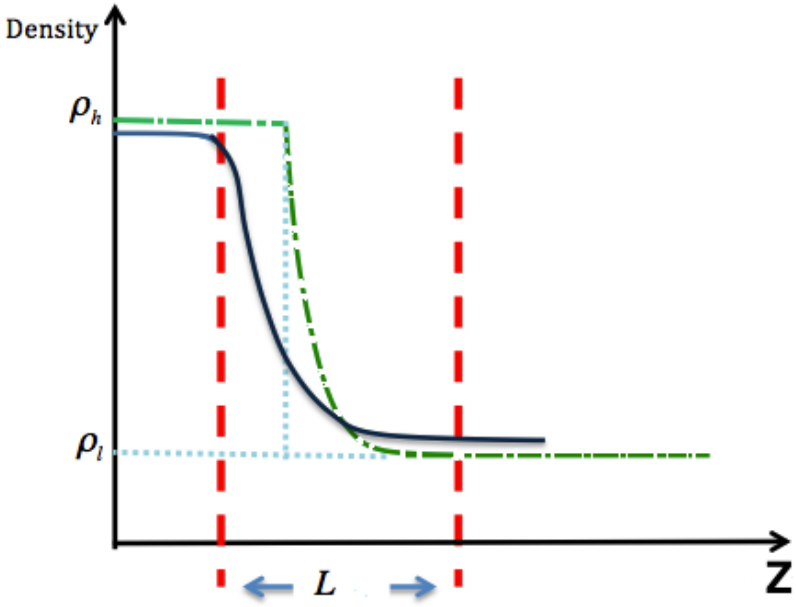

Figure 3.3: The density profile at the interface between the two fluids. The dot-dashed green curve shows the initial density profile while the solid blue curve shows the density gradient profile after the target expansion. L refers to the density gradient scale length (3.24).

As seen (3.26), one of the roots is positive, which indicates the growing perturbations. Both density gradient L and finite thickness of the fluids f reduce this growth. In the case that A_t becomes negative, this would imply that a perturbation oscillates around its initial amplitude. Therefore, A_t needs to be of a positive order to make the perturbation grow.

In the case of very deep fluids (i.e. $kh_l, kh_h >> 1$) and ignoring the effect of a density gradient, (3.26) reduces to the classical RT form $\gamma_{RT} = \pm\sqrt{A_t kg}$. In the work of Chapter 6, the growth rate of the form of (3.26) is used as this form best represents the situation of the RT instability in non-ablating laser-plasma experiments [85, 95].

There are other terms which can be added into (3.26) which will reduce the RT instability growth. These are surface tension, viscosity and ablation. However, in the scope of the laser-plasma experiments, both surface tension and viscosity are negligible since the plasma acceleration is high [12,103]. Typically the acceleration is in the order of 10^{15} cms^{-2} in a long-pulse laser experiment [34] and potentially much higher for high intensity experiments. Nevertheless, these effects may be important at very short wavelength [12]. Although ablation has a significant stabilising effect in for example ICF capsules [81], it will not significantly contribute if the target has a configuration similar to Figure 3.2.

It is worth mentioning that in the above derivatavation, the fact that plasma is a compressible fluid is not taken into account. The debate of the role of compressibility in RT growth has not been determined yet [104]. However, (3.26) shows good agreement with many laser-plasma experiments, for example the experiment of Ref. [95], which addresses whether compressibility stabilises or destabilises the growth. The conclusion is that the effect is relatively small [12]. Furthermore, in RT unstable situation in high energy density matter radiation loss can act to stabilise the instability growth by reducing the pressure gradient. In the experiment described latter in Chapter 6, radiation losses lead to a RT stable configuration becoming unstable (by reversing the pressure gradient) and then back to a RT stable through reversing the pressure gradient again. Thus, Radiation can modify the RT growth rate via the changing the pressure gradient. The RT stabilisation due to strongly radiative shocks is discussed by Huntingdon et al. [105].

3.2 Radiative losses in dense plasma

The plasma hydrodynamics can be strongly influenced by radiation transport. Within the plasmas, the photons can interact with bound and free electrons by absorption, emission and scattering processes. This interaction involves exchanges of momentum and energy. Therefore, the methodology of calculating opacity and the inclusion of atomic processes and radiation transport into hydrodynamic simulation codes are essential to compute accurately the hydrodynamics of the plasmas. The exact analytical solutions to the complete form of the non-linear radiative transfer equation, which is a kinetic equation for photons [38], are difficult to obtain since the radiation field is a function of position, time, energy and propagation angle [38,106]. Hence, the equation is approximated using a multi-group diffusion approach [107]. This method allows the radiative transfer equation to be solved within a specific range of photon frequency domain. Good approximation is obtained when the mean free path of the photons λ_ν is very short compared to the hydrodynamic length scales [38]. The basic idea of the multi-group approach is to split the frequency spectrum into a finite number of groups. So the detailed spectrum and opacities are averaged in separate groups and the resulting opacities are given as group-averaged opacities [107].

The plasma emits radiation via free-free, bound-free and bound-bound emission processes. The free-free (bremsstrahlung) and bound-free (radiative recombination) transitions result in a continuous emission spectra while the bound-bound (radiative de-excitation) transition results in line spectra. The emitted radiation from the hot plasma is an important diagnostic tool of the plasma as it contains information about the plasma temperature and density [6, 108]. During the hydrodynamic simulation relating to the work of Chapter 6, the effect of accurate theoretical opacities data has great impact on predictions of radiative cooling, which in turn affects target hydrodynamics and the growth of the RT unstable perturbations. The following subsections cover opacity and radiative cooling in more depth.

3.2.1 Opacity

The opacity is a measure of the extent to which a plasma is opaque or transparent to radiation due to absorption (or emission) and scattering processes. When radiation with frequency ν, travels a distance s in the direction z through plasma of mass density ρ, the spectral radiation intensity I_ν is [6],

$$I_\nu = I_{\nu 0} \exp\left[-\int_0^s \rho\ \kappa_\nu\ \mathrm{d}z\right] \tag{3.27}$$

where $I_{\nu 0}$ is the initial spectral intensity at $s = 0$, $\kappa_\nu = \mu_\nu/\rho$ is opacity and μ_ν is the absorption coefficient. The spectral intensity I_ν is the transported energy through area dA during time dt and frequency $d\nu$ [38]. The ratio of I_ν to $I_{\nu 0}$ gives the transmission T_ν [11] while the integral in (3.27) gives the optical depth τ_ν. If $\tau_\nu >> 1$, the plasma is optically thick which means that the mean free path of the photons (λ_ν) is much less than the plasma thickness while if $\tau_\nu < 1$, the plasma is optically thin and λ_ν is comparable or greater than the plasma thickness. However, the optical depth τ_ν varies with frequency which means that the plasma may be optically thin at one wavelength and optically thick at another [6]. The mean free path of the photons λ_ν is given by,

$$\lambda_\nu = \frac{1}{\rho\ \kappa_\nu} \tag{3.28}$$

The λ_ν gives the average distance of the photon flight into the plasma before it becomes absorbed or emitted.

Opacity depends highly on the composition and conditions (i.e. temperature and density) of the plasmas. There are various processes that contribute to the total absorption (or emission) of photons, i.e. the free-free, bound-free and bound-bound processes [108].

Two main approaches to the spectral averaging of opacities are the averaged Planck mean $\kappa_{<\nu>p}$ and the averaged Rosseland mean $\kappa_{<\nu>R}$ opacities. The former

normalises the Planck blackbody as the weighting function then averages the opacity values directly, while the latter uses the temperature derivative of the Planck curve as the weighting function then averages the inverse of the opacities. The Planck mean opacity yields correct values for optically thin plasmas, and the Rosseland mean in the case of optically thick. Both methods are defined respectively, as [109],

$$\kappa_{<\nu>p} \equiv \frac{\int_0^\infty \kappa_\nu B_\nu d\nu}{\int_0^\infty B_\nu d\nu}. \tag{3.29}$$

$$\kappa_{<\nu>R} \equiv \frac{\int_0^\infty \frac{1}{\kappa_\nu}\frac{\partial B_\nu}{\partial T} d\nu}{\int_0^\infty \frac{\partial B_\nu}{\partial T} d\nu}. \tag{3.30}$$

where κ_ν is the monochromatic opacity and B_ν is the normalised Planck black-body function.

Creation of theoretical opacity data needs accurate calculation of the radiative properties of plasmas. This is difficult due to the large amount of atomic data that has to be taken into account such as transitions, populations and photoionisation cross-sections as well as spectral line shapes [110]. Considerable effort has been made to generate theoretical opacity data such as TOPS [111], IMP [112] and PROPACEOS [113].

In this thesis, two different types of opacity are used in the hydro-codes: opacity that is based on the screened hydrogenic atomic model in HYADES [114] and tabulated PROPACEOS opacities [113] based on the detailed configuration accounting (DCA) atomic model. In the screened hydrogenic atomic model, the wave function of each electron is calculated as a hydrogen-like atom. The electric field of the nucleus determining the orbit of each electron is shielded by the other electrons' charge. A set of screening constants is usually used to mimic the effect of the other electrons. Thus, the accuracy of the model depends on these screening constants [115]. In the context of opacity, the main problem is that this model is missing a description of the line splitting of n-shells into n, l and j states. This splitting occurs for single electron states due to the relativistic fine structure. These configurations need to be

taken into account in the opacity for intermediate and high-Z materials [12]. The splitting has recently been included in a screened hydrogenic model [116]. On the other hand, the detailed configuration accounting (DCA) atomic model provides details of different excitation states and occupations in the plasma. These details include the sub-shell levels, continuum lowering and spectral line transport [112]. In this model, the spin-orbit interactions (i.e. j-j coupling) are included in opacity calculations. This is time-consuming in the case of high-Z materials due to the high number of levels which need to be computed. So the results are tabulated rather than calculated inline with hydrodynamic simulations.

Both of the above atomic models can be calculated in local thermodynamic equilibrium (LTE) or non-LTE models. The assumption of LTE simplifies the solution of rate equations by considering that the electrons and ions are in equilibrium while the photons are not. There are two conditions that have to be satisfied in order to assume that the plasma is in LTE. Firstly, the plasma needs to be dense enough so that the collisional processes dominate over the radiative processes and secondly, all transition processes are in detailed balance, i.e. each transition is balanced by its inverse [6].

Both opacity models are compared to TOPS opacities later in Chapter 6 [111]. TOPS opacity is calculated using the LEDCOP code which is based on Detailed Term Accounting (DTA) atomic model. This model includes each possible transition and the details of the line shapes that arises from LS coupling with an atom. Therefore, it is computationally expensive and usually restricted to the study of lighter elements.

3.2.2 Radiative cooling rate

The radiative cooling rate is the rate of loss of thermal radiation by inelastic collisions with atoms, ions or molecules [117]. The cooling rate Q_{Emis} in terms of

multi-group opacities is given as [118],

$$Q_{Emis} = \frac{8\pi(k_B T_e)^4}{c^2 h^3} \sum_{g_i}^{N_f} \left(\kappa_{\nu p_{g_i}} \int_{x_{g_i}}^{x_{g_i+1}} \frac{x^3}{\mathrm{e}^x - 1} \mathrm{d}x \right), \; x = \frac{h\nu}{k_B T_e} \tag{3.31}$$

where g_i is the photon frequency group index, N_f is the number of frequency groups and $\kappa_{\nu p_{g_i}}$ is the mean Planck opacity for frequency group g_i that defined in (3.29). However, equation (3.29) can be written as function in emissivity η_ν in relation (3.31) as [118],

$$\kappa_{\nu p_{g_i}} = \frac{1}{\rho} \frac{\int_{x_{g_i}}^{x_{g_i+1}} \eta_\nu dx}{\int_{x_{g_i}}^{x_{g_i+1}} B_\nu(T) dx} \tag{3.32}$$

where ρ is the density and η_ν is the emissivity which depends upon temperature and degree of ionisation [34]. The emissivity follows Kirchhoff relation, i.e. $\eta_\nu = \mu_\nu B_\nu(T)$, only under the assumption of LTE. The cooling rate in (3.31) is in units of energy per unit mass per unit time. As shown in (3.31), radiative cooling is strongly dependent on temperature, which means that radiative cooling has a significant role in hot plasmas. Also, it depends on the opacity where different atomic processes are included. At high temperature, different ionisation levels contribute to the opacity and line radiation from different ions may significantly contribute to the opacity and emissivity. This emphasises the importance of inclusion the detailed atomic physics in hydro-codes although accounting for the details of these effects is challenging, especially for high-Z materials [118].

In a dense plasma, cooling occurs through ionisation, excitation and collisional processes, especially the three-body recombination collisional process. In this process, two free electrons enter into an ion sphere at the same time. One of them is captured by the ion while the other carries away the extra energy. Since this process requires the presence of two electrons, its rate is high in the dense plasmas and the density factor of this process contains n_e^2 which corresponds to the two

electrons [108]. Both temperature and density decrease rapidly with time and the target cools adiabatically due to its expansion into the vacuum [119]. As the density drops, the three-body recombination rate decreases. However, the emission and cooling can still have strong collisional dependence through collisional excitation and de-excitaition processes, which both scale linearly with electron density n_e [30].

3.3 Laser-plasma hydrodynamic codes

The standard laser-plasma hydrodynamic code simulates a plasma as two or three temperature quasi-neutral plasma and comprises a set of hydrodynamic equations as follows [8],

$$\frac{\partial \rho}{\partial t} + \nabla.(\rho \mathbf{u}) = 0 \tag{3.33}$$

$$\frac{\partial \rho \mathbf{u}}{\partial t} + \nabla.(\rho \mathbf{u}\mathbf{u}) + \nabla P - F_p = 0 \tag{3.34}$$

$$\frac{\partial \varepsilon_e}{\partial t} + \nabla. \left[\mathbf{u}(\varepsilon_e + P_e) + q_e - \frac{Q_{ei}}{\gamma_e - 1} \right] = \Phi_L + Q_{Abs} - Q_{Emis} \tag{3.35}$$

$$\frac{\partial \varepsilon_i}{\partial t} + \nabla. \left[\mathbf{u}(\varepsilon_i + P_i) + q_i + \frac{Q_{ei}}{\gamma_i - 1} \right] = 0 \tag{3.36}$$

Equation (3.33) is the continuity equation, where ρ and $\mathbf{u}$ are the mass density and velocity respectively . Equation (3.34) is the momentum equation, where P is the pressure and F_p is the ponderomotive force which is defined in (2.10). This term, which presents the way of laser-plasma coupling, acts only on the electrons since they respond effectively to the electric field of the laser. However, most hydrodynamic codes not include F_p and the laser-plasma coupling is due to inverse bremsstrahlung.

The energy equation is usually written twice; once for electrons (3.35) and once for ions (3.36), subscripts e and i respectively. This is to allow for thermodynamic imbalance between electrons and ions and to heat to a two temperature model. One for electron and one for ions. The energy density $\varepsilon_{e,i}$ is the sum of internal and

kinetic energies,

$$\varepsilon_{e,i} = \frac{P_{e,i}}{\gamma_{e,i} - 1} + \frac{1}{2}\rho u^2 \tag{3.37}$$

where $\gamma_{e,i}$ is the number of degrees of freedom for each species.

The terms $q_{e,i}$ in (3.35) and (3.36) describe the heat flow inside the plasma [6],

$$q_{e,i} = -\kappa_{eff} \nabla T_{e,i} \tag{3.38}$$

where,

$$\kappa_{eff} = \min \left\{ \kappa_{e,i}, f \frac{q_f^{e,i}}{|\nabla T_{e,i}|} \right\} \tag{3.39}$$

where $\kappa_{e,i}$ is the thermal conductivity coefficient for electrons and ions, respectively, $q_f^{e,i}$ is the free-streaming heat flux and f is the flux limit multiplier; the typical value in the case of high laser intensity is in the range of 0.03 [120] to 0.1 [121] although for NIF, a flux limiter of 0.15 seems to apply [122]. Equation (3.39) implies that the heat flow is limited and corrected. This is due to the fact that the classical theory of Spitzer and Harm [34] overestimates the heat flow in the case of steep temperature gradient. $\mathbf{Q}_{ei}$ is the electron-ion heat exchange rate [8],

$$Q_{ei} = \frac{2m_e}{m_i} \frac{n_e k_B (T_e - T_i)}{\tau_{ei}} \tag{3.40}$$

where τ_{ei} is the inverse of electron-ion collision time $\bar{\nu}_{ei}$ which is defined in (2.20).

Φ_L in (3.35) is the absorbed laser flux ($\Phi_L = \beta I_L$) which defines another way of laser-plasma coupling [8]. The β is the fraction of the laser energy coupling to electrons and I_L is the laser intensity. Q_{Abs} and Q_{Emis} are the radiation energy absorption and emission respectively [113] which usually computed using multi-group diffusion approach with tabulated opacities.

The above set of equations - (3.33) to (3.36) - is closed via an equation of state which connects pressure and temperature. If the plasma is at low densities, the ideal gas equation of state is used, (i.e. $P = k_B n T$), while if the plasma is at high

densities, the Thomas-Fermi statistical model is used. Typically, in high-energy density simulations, a tabulated equation of state is used for each material [8]. Description of the hydrodynamic codes that have been used in this thesis is given in the next subsections.

3.3.1 HYADES

HYADES is a 1-D Lagrangian radiation-hydrodynamic code written by Jon Larson [114]. As a Lagrangian code, the mesh moves with the plasma, which means that the mass is fixed within each cell. This helps to maintain the boundaries between the different materials which is useful in tracking the interface between them. The code can set up three different geometries; planar, cylindrical and spherical. The plasma is treated in the fluid approximation, in which electron and ions are treated separately; their velocities are described via Maxwell-Boltzmann statistics and the radiation is only coupled to the electrons. Temperature are calculated for electrons, ions and radiation field.

Two approximation methods are used in the radiative energy transport package; a gray diffusion approximation and a multi-group diffusion approximation. In the former, the photons have a pure Planckian distribution and the opacity is extracted from the SESAME data library. The multigroup model allows for a small departure from Planckian radiation distribution. Opacity data is generated using an internal algorithm based on the screened hydrogenic model and includes some atomic shell and simple x-ray line effects. The limit definition of radiation group is used to generate opacity data, a specific number of spectral groups with a minimum and maximum range of energy needs to be assigned. In both methods, the assumption of the type of spectral averaging of opacities (Planckian mean or Rosseland mean) is needed.

Different ionisation models are included in the code, starting with the Saha, LTE average-atom, non-LTE average-atom, Thomas-Fermi and fully stripped models. In

addition, the code has several ways to deposit the energy in the material such as lasers, radiative fluxes and other sources.

3.3.2 HELIOS

HELIOS is also a 1D Lagrangian hydro-code and was developed by Prism Computational Sciences Inc [113]. The hydrodynamic model and geometries are similar to HYADES. The laser energy is deposited by the inverse bremsstrahlung model. HELIOS differs from HYADES that both the equation of state and opacity data are obtained from the PROPACEOS code (Prism OPACity and Equation Of state code). The contributions of the bound-bound, bound-free and free-free processes to the multi-group opacity are computed using the DCA model. The absorption and emissivity are determined from the atomic level populations. Although using the DCA model for multi-group opacity calculations is computationally expensive, especially for intermediate atomic number such as Cu, as thousands of atomic energy levels are computed, it provides an accurate opacity data which is vital for radiative cooling calculation as shown in (3.31). The exchange of radiative energy with plasmas such as the radiative cooling rates Q_{Emis}, defined in (3.31), and Q_{Abs} are both computed using Planckian opacities while the transport term in the radiation diffusion equation is computed by using Rosseland mean opacities [123].

It worth mentioning that fast electron transport is not included in HYADES or HELIOS, all fast electron modelling in this thesis was done with the ZEPHROYS code (section 2.4). The temperature that results from the fast electron heating are used as initial inputs to both hydrodynamic model.

3.4 Summary

This chapter has given the background to RT instability and radiative losses in dense plasmas. The RT instability has been introduced, followed by a brief literature

review of RT instability in laser- plasma interaction. The RT growth formula has been derived and discussed in the context of laser-plasma interaction. The radiative losses in dense plasmas are discussed, including opacity and radiative cooling rates. Finally, the standard laser-plasma hydrodynamic code has been discussed with an introduction to the two hydro-codes, HYADES and HELIOS, which were used to study the RT experiment discussed in Chapter 6.

Chapter 4

Angular dispersion in fast electron heated targets

4.1 Introduction

This chapter includes a description of angular dispersion of a fast electron beam. Angular dispersion affects the longitudinal penetration of the fast electrons and target heating. This effect is compared to the electric field inhibition [21] which also limits electron beam penetration into extended targets. As presented in Chapter 2, multi-MeV fast electrons are generated at intensities above 10^{18} Wcm^{-2} due to the coupling of a significant fraction of laser energy to a dense target. The fast electrons set up a huge electric field close to the target surface due to charge separation. This field confines significant number of electrons to near the target surface [21]. It is stated in Section 2.3.2 that the fast electrons are transported into the target once they are neutralised by background electrons. However, the background electrons move slowly compared to the fast electrons and undergo a lot more scattering and collisions (see Section 2.3.3). This limits their mobility [47]. Further, the ability of the plasma to provide background electrons is restricted by time dependent target ionisation and conductivity [21, 124]. If there is a deficiency in the number of background electrons needed to balance the fast electrons, an

inhibition results [21, 45, 70] and is known as " electric field inhibition".

Another phenomenon limits electron penetration of a target, this is the new material set out in this chapter, and is angular dispersion. A comparison is made between the effect of angular dispersion and electric field inhibition, this shows that angular dispersion more strongly impedes fast electron penetration and impairs target heating. Further, the angular dispersion is significant even under extreme control of the fast electron spreading.

This chapter begins with a discussion of factors that hinder fast electron penetration and target heating (Section 4.2), followed by details of how the transverse fast electron spreading can be controlled (Section 4.3). Then an analytical and numerical investigation of the angular dispersion of the fast elections is presented (Section 4.4). A numerical comparison of the electric field inhibition and angular dispersion is then made (Section 4.5). Finally, the results of the chapter are discussed (Section 4.6).

4.2 Fast electron penetration and target heating

Section 2.3.4 states that the main mechanism of target heating is Ohmic heating. In this heating mechanism, the resistive background electron current heats the plasma as it flows to balance the opposite fast electron current. Due to this balance, the heating rate can be determined by the fast electron current density,

$$\frac{\partial T_b}{\partial t} = \frac{2}{3k_B n_b}\eta \mathbf{j}_f^2. \tag{4.1}$$

The full derivation of (4.1) is given in Section 2.3.4. Clearly, this heating rate depends on the fast electron density (since $\mathbf{j}_f = en_f v_f$). Therefore, if the fast electron density is reduced, the heating rate will reduce. Thus, the target heating depends on

- the ability of the fast electrons to penetrate a target; and

- the production of enough background current by target ionisation to satisfy current balance (Section 2.3.2).

Evans *et al.* [19] show that the resulting background temperature can reach 500 eV within a few picoseconds. This rapid heating is desirable in many applications, such as investigations into the atomic physics of dense plasma [125], the Fast Ignition approach [31] and the application describe in Chapter 6. There are three well-studied factors which impede fast electron penetration and consequently impair target heating. These are electric field inhibition [21], filamentation [24] and fast electron spreading [22]. Each of these factors affects the target heating in a specific direction with respect to the fast electron beam axis, as shown in Figure 4.1.

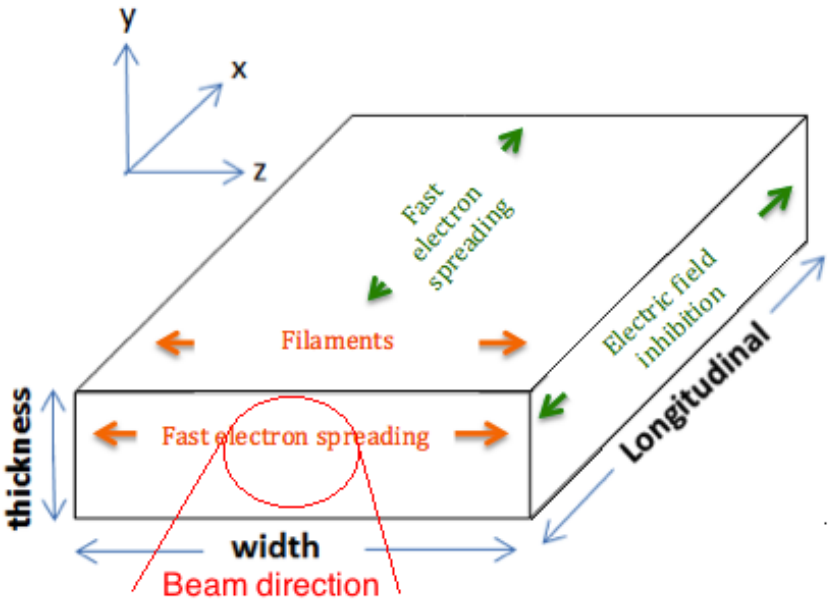

Figure 4.1: The mechanisms that affect the fast electron penetration with respect to the fast electron beam axis and target dimensions. The fast electron spreading and filaments reduce the fast electron penetration in the transverse directions (width and thickness in the Figure) while the fast electron spreading and electric field inhibition reduce the penetration in the longitudinal direction.

The electric field inhibition is greatest in the longitudinal direction (x in Figure 4.1), where the fast electrons move along the beam axis. The reason for it being greatest on-axis is that the laser intensity at this point would be expected to lead to higher current density [39]. This effect was identified by Bell *et al.* [21] and

experimentally demonstrated by Pisani *et al.* [70]. Using (2.40) with ignoring the magnetic field, if one assumes, for example, the fixed resistivity of Al $\eta \approx 10^{-6}$ Ω.m and $\mathbf{j}_f \approx 10^{17}$ Am^{-2}, electric field strength can reach $E \approx 10^{11}$ Vm^{-1}. Thus, the electric potential energy is about 1 MeV over a distance of 10 μm. This amount of energy is large enough to confine a significant number of the fast electrons that have a lower energy than this. This causes a rapid drop in the fast electron density with depth in the target.

Filamentation [24] occurs in the transverse directions (y and z in Figure 4.1). In these directions, the fast electrons move out of the beam axis. As discussed in Section 2.3.6, the filamentary structures occur due to transport instabilities. When small perturbations arise in the transverse magnetic field, the magnetic force bends the opposing currents, which eventually leads to the radial break-up of the fast electron beams into filaments. Consequently, the target is heated non-uniformly in these filaments. This heating is observed in the work of Chapter 6.

Fast electron spreading or divergence affects the fast electron penetration in the transverse directions and longitudinal direction as shown in Figure 4.1. The fast electrons spread outwards transversely due to several complex mechanisms which include scattering with ions and background electrons [45] and influence of the magnetic field near the critical surface [38]. Experimental evidence [22, 23] show that the fast electrons propagate in solid targets with large divergence angle usually characterised by the half-angle of divergence θ_d between 30° [23] and more than 50° [22]. Although there is as yet no full characterisation of this angular spread, the experimental measurement [23] states that the divergence angle increases with the laser intensity. This makes the fast electron beam radius size grow to several times the laser spot size [22]. The control of fast electron divergence has been subject on many studies, e.g. [126, 127], including the work by Robinson and Sherlock [60] on using the structured resistive-guiding. In the next section, control of the fast electron spreading is introduced which differs from the structured resistive-guiding

concept. This control of the fast electron spreading allows clear observation of the considerable impact of the angular dispersion on the longitudinal heating.

4.3 Controlling the transverse spreading of fast electrons

The fast electron divergence increases with the increased transverse dimensions of the target. Control of the fast electron divergence is possible using a narrow or wire shaped target under condition that the width and thickness of the target are comparable to the laser spot size. This gives excellent fast electron transverse confinement. Figure 4.2 shows a square cross-section target. Wire targets were experimentally used in [128,129] as nail-wire target and cone-wire target respectively. The nail head and cone aided laser coupling to the target. In this section, the spreading of the fast electrons is controlled from the early stages of the interaction and a high degree of laser pointing stability is assumed.

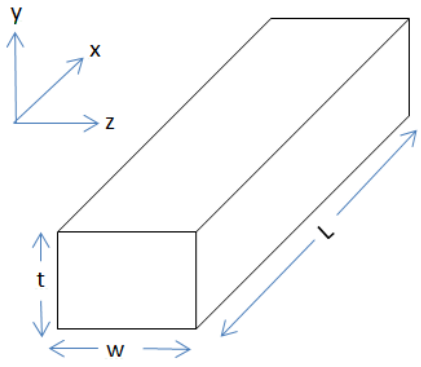

Figure 4.2: Wire-like target geometry, w refers to the width, t to the thickness and L to the length.

Fast electron transverse confinement was explored using ZEPHYROS. An Al wire-like target was designed using two different target dimensions; $200 \times 27 \times 27$ μm^3 and $200 \times 15 \times 15$ μm^3. These target dimensions are represented by $L \times w \times t$

respectively in Figure 4.2. The ratio of the laser diameter spot size to the $w \times t$ dimensions was 1:3 for $200 \times 27 \times 27$ μm^3 and 2:3 for $200 \times 15 \times 15$ μm^3, where the laser spot radius size, r_{spot}, was 5 μm. The cell size of the grid was 1 μm in each direction with 800 macroparticles injected into each cell. This helps to reduce the statistical noise. The convergence in ZEPHYROS is discussed in Appendix A. The laser irradiation intensity was 1.27×10^{20} Wcm^{-2} in a 500 fs duration pulse. The temporal profile of the fast electron beam is top-hat shaped and the transverse profile is $\propto \exp[-\frac{r^2}{2r_{spot}^2}]$. It was assumed that 30 % of the laser energy coupled to the fast electrons. The fast electron beam mean energy was 2.7 MeV. The background temperature was set initially to 1 eV everywhere. The resistivity is described by the Lee and More model. The minimum mean free path was taken as $5r_s$, where r_s is the interatomic spacing (Section 2.3.3). The fast electron angular distribution is uniform over a solid angle defined by the input of a divergence angle θ_d. Reflection boundary conditions were implemented. The main parameters, which are varied in the simulations, are summarised below in Table 4.1. Divergence angles of $\theta_d = 50^\circ - 60^\circ$ are used to match experimental observations at laser intensity that exceed 10^{20} Wcm^{-2} [22].

Target	target dimension (μm^3) ($L \times w \times t$)	θ_d (degree)
A	$200 \times 27 \times 27$	50
B	$200 \times 27 \times 27$	60
C	$200 \times 15 \times 15$	60

Table 4.1: Wire-like target dimensions and the half-angle divergence angle that used in each simulation.

Figure 4.3 shows a spatial plot of the background temperature along the x-direction at 700 fs for Targets A, B and C respectively. The temperature map uses a logarithmic colour scheme with $\log_{10}(\mathrm{T_b})$. The fast electron spreading is controlled in the transverse directions (y and z) and results in uniform transverse temperatures. Target C shows a higher background temperature compared to Targets A and B, since the ratio of the laser diameter spot size to the transverse directions is higher.

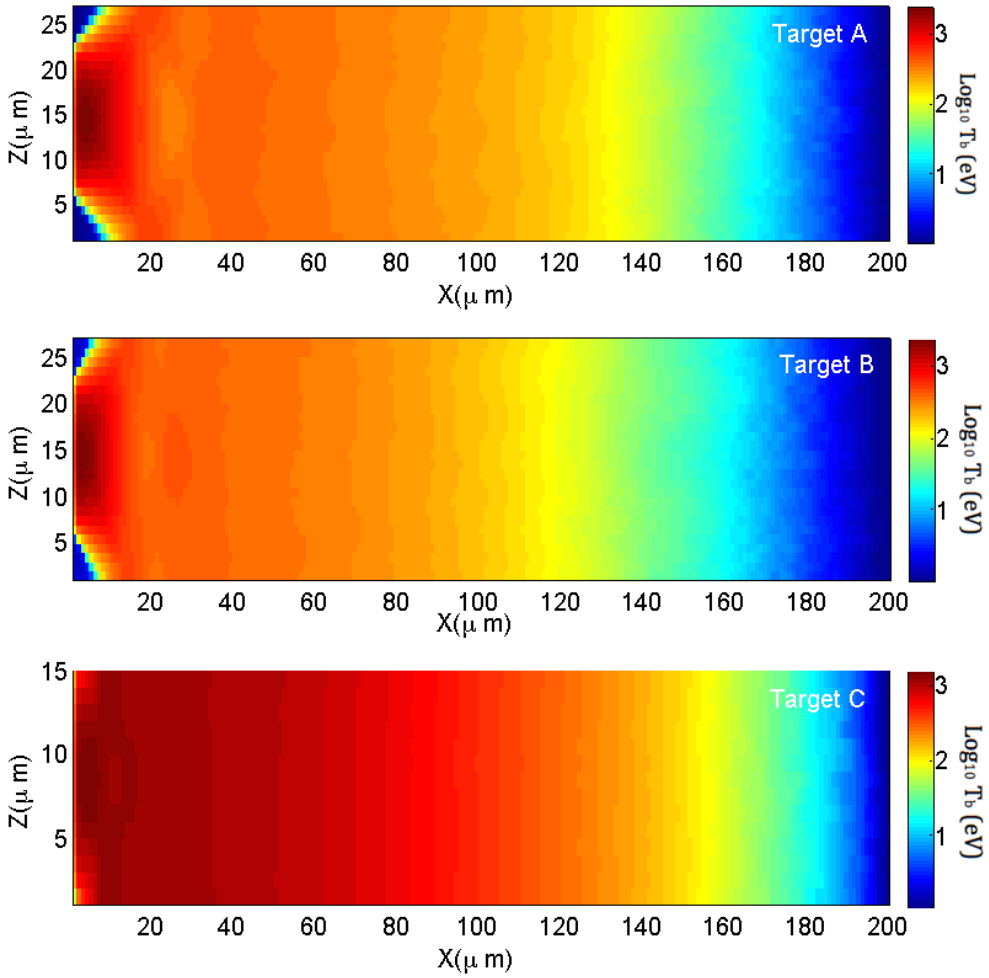

Figure 4.3: Plots of background temperature (eV) $\log_{10}$ along the x-direction at 700 fs (X-Z Slices). The longitudinal (x) and transverse (z) axes are defined in Figure 4.2. The half-angle divergence of Target A is 50° and that of Targets B and C is 60°.

On the other hand, even with this control of the spreading, there is a clear non-uniform heating with the depth in all three targets (x-axis in Figure 4.3). This non-uniformity of heating is seen in experiments as temperature gradient. One of the reasons for this gradient is the surface electric field inhibits penetration of the fast electrons. Notice the slight differences in the temperature gradients of Targets A and B. The simulation conditions of Targets A and B are identical, with the exception of the 10° difference in the divergence angle. This implies that the fast electron half-angle divergence has a role in the fast electron penetration, even with the target geometry controlling the transverse spreading. Figure 4.4 shows a line-out

of the background temperatures in eV of Targets A and B along the x-direction for $40 \leq x \leq 200$ μm at 700 fs. The most important point is that Target A is heated slightly more than Target B simply by reducing θ_d. This suggests that the fast electron penetration in Target B is reduced longitudinally due this slight difference in the angle compared to Target A. The electron density and current density are identical at injection. The electric field inhibiting electron penetration is the same in Targets A, B and C. The reduction of heating in Target B is due to the reduction in fast electron density across the target depth due to angular dispersion. This assumption is discussed in the following section.

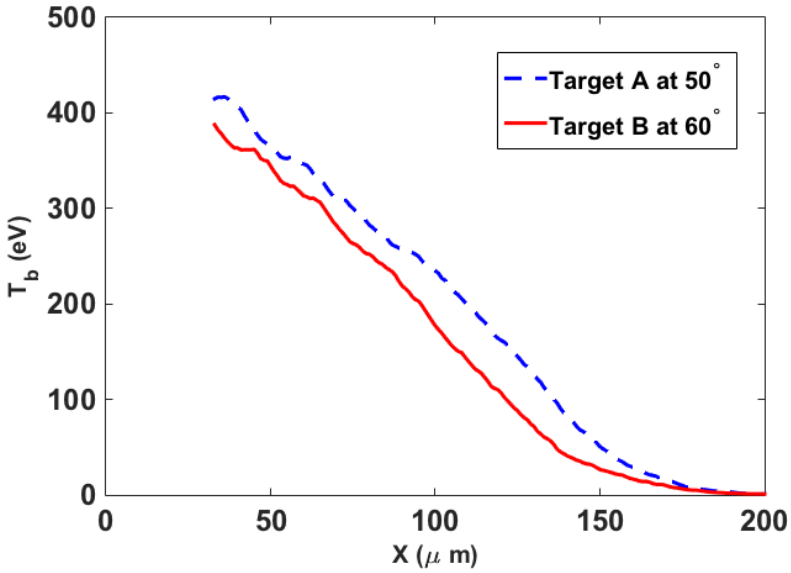

Figure 4.4: Line-out of background temperature in the unit of eV from Targets A and B along the x-direction for $40 \leq x \leq 200$ μm at 700 fs. The dashed blue line for Target A at 50° and the solid red line for Target B at 60°.

4.4 Angular dispersion of the fast electrons

All the electrons in the fast electron beam are relativistic and move with speed close to c. The divergence of the fast electron beam means that fast electrons acquire transverse and longitudinal velocity spread between c and $c \sin \theta_d$ and $c \cos \theta_d$ respectively. This causes an increase in the length of the fast electron beam with

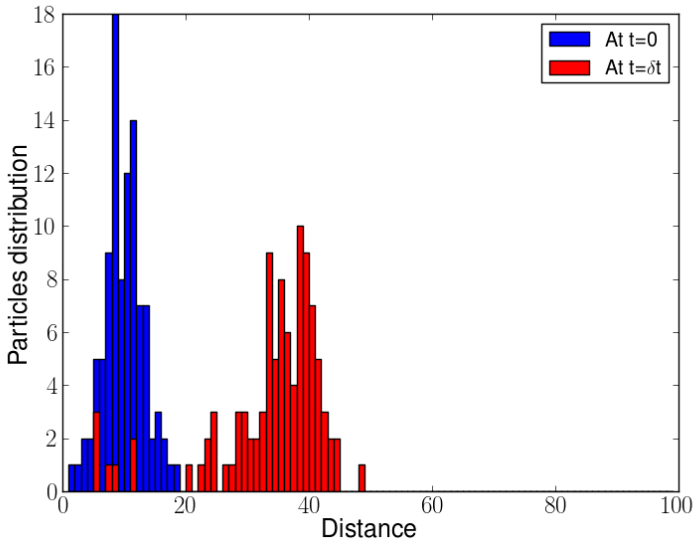

Figure 4.5: Schematic of Gaussian-like distribution function for particles at t=0 (blue bins). After the period of time δt , each particle gains a longitudinal velocity spread $c\cos\theta$ (red bins) which disperses the particles along of the path.

time and a spatial dispersion results from this velocity spread. The result is a drop in the fast electron density along the x-axis. Figure 4.5 shows a demonstration of the angular dispersion. Initially, a group of particles has a Gaussian distribution shown as blue bins. After a short period of time δt, this group is dispersed (red bins) as each particle acquires its own velocity and angle while moving a certain distance. Because of this, the length of the group increases with δt. This is analogous to what happens to a fast electron beam with a longitudinal velocity spread. The length of the fast electron beam increases in the longitudinal direction with time due to spatial dispersion caused by the velocity spread. In the next subsections, the effect of the angular dispersion on the target heating is discussed analytically and numerically.

4.4.1 Analytical model

Figure 4.6 shows a schematic of the fast electron trajectory inside the wire-like target. $c\tau_0$ is the length of the fast electron beam and ct is the propagation distance of the fast electron beam. As the fast electrons travel with θ_d due to the angular spread, the difference in travel between the fast electrons travelling with θ_d and the

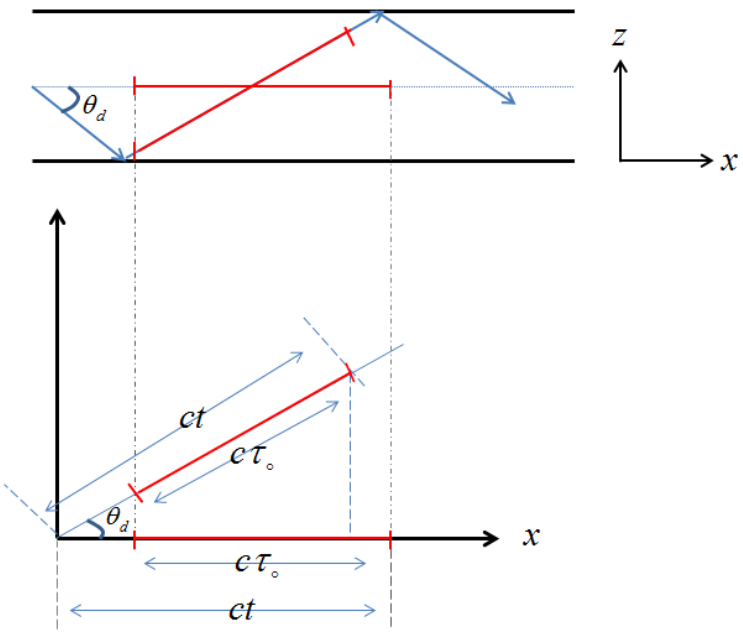

Figure 4.6: Schematic of fast electron trajectory inside the wire-like target in the x-z plane showing the difference in travel along the x direction. $c\tau_0$ is the length of the fast electron beam at injection and ct is the propagation distance the fast electron beam.

others travelling in the x-direction as shown in Figure 4.6 is ,

$$\delta x = ct(1 - \cos\theta_d) \tag{4.2}$$

Consider the spatial dispersion induced by the angular spread of the fast electrons θ_d. Let us denote the effect of the dispersion by α. The dispersion increases the fast electron beam duration, i.e. $\tau_0 \rightarrow \alpha\tau_0$. The length of the fast electron beam with dispersion is $c\tau_0 + \delta x$. Thus, the dispersion after a given time t is,

$$\alpha = 1 + \frac{t}{\tau_0}(1 - \cos\theta_d) \tag{4.3}$$

and the dispersion at a given depth is,

$$\alpha = 1 + \frac{x}{L_0} \tag{4.4}$$

where,

$$L_0 \approx \frac{c\tau_0}{1-\cos\theta_d} \tag{4.5}$$

L_0 is the fast electron penetration depth due to the beam divergence. Larger depth L_0 indicates more uniform heating. Clearly from (4.5), more uniformity in heating can be obtained with a lower divergence angle θ_d or a larger beam duration τ_0. This suggests more uniform heating using a 1 ps rather than a 100 fs laser pulse.

However, the dispersion decreases the fast electron density according to flux conservation, i.e. $n_f \rightarrow n_f/\alpha$, and this affects the Ohmic heating as follows. The Ohmic power heating per unit volume has been previously defined in (2.30) as,

$$P_{heat} = \eta \mathbf{j}_f^2 = \eta e^2 c^2 n_f^2 \tag{4.6}$$

where η is a fixed resistivity. Due to the dispersion, (4.6) becomes,

$$P_{heat} = \frac{\eta e^2 c^2 n_f^2}{\alpha^2} \tag{4.7}$$

This implies that the dispersion has a quadratic effect on the heating power. This means that the overall heating rate falls with the dispersion. Thus, although the dispersion increases the fast electron beam duration and as a result the beam can heat the target for longer, there is also a strong reduction in the fast electron density due to this effect.

4.4.2 Numerical demonstration

The effect of angular dispersion on the fast electron density is numerically investigated with parameters for Target A (see Table 4.1 Section 4.3), and with a beam duration and divergence angle of 100 fs and 30° respectively. The simulation includes electric field inhibition. Figure 4.7 shows a time sequence of the fast electron density. The increase in the longitudinal length of the fast electron beam over time

is seen in Figure 4.7 (a) - (e). There is a corresponding decline in the fast electron density as the beam increases in the length and as time progresses. The reduction of the fast electron density in the longitudinal direction is due to both electric field inhibition and the angular dispersion. Figure 4.7 shows that the dispersion becomes significant after the end of beam duration of 100 fs, as suggested by (4.3). In addition, the uniform distribution of the fast electron beam over a solid angle of 30° is shown in Figures 4.7 (a) and (b). In this distribution, more fast electrons at the edge of the cone than at its centre. The beam loses its original uniform distribution shape over time as shown in Figure 4.7 (b)-(e). This change in the shape of the injected beam provides another evidence of angular dispersion.

4.4.3 Effect of the divergence angle

Al wire-like targets in the Target A geometry were simulated with $\theta_d = 30°$ and 50°. The beam duration in both simulations was 500 fs. Figure 4.8 shows Y-Z slices of the fast electron density across $x = 30$ μm for $\theta_d = 30°$ at 700 fs and 1500 fs in (a) and (b) respectively and for $\theta_d = 50°$ at 700 fs and 1500 fs in (c) and (d) respectively. The fast electron density map uses a logarithmic colour scale. Due to sampling at $x = 30$ μm, it is possible to see electron ring-like structure for small divergence, e.g. 30°, to larger divergence, e.g. 50°, this is washed out by reflections off target surface. This is shown in Figures (a) and (c) 700 fs for 30° and 50° respectively. Furthermore, it is apparent that fast electron density is more slowly dispersed with 30° compared to with 50° as suggested by (4.4) and as shown in Figures 4.8 (b) for 30° and (d) for 50°. The fast electron density is higher at 30° than at 50° at the same time of 1500 fs.

4.4.4 Scale of the fast electron penetration

Equation (4.5) indicates that larger fast electron penetration depth L_0 implies higher temperatures to greater depth. This increased heating can also be obtained

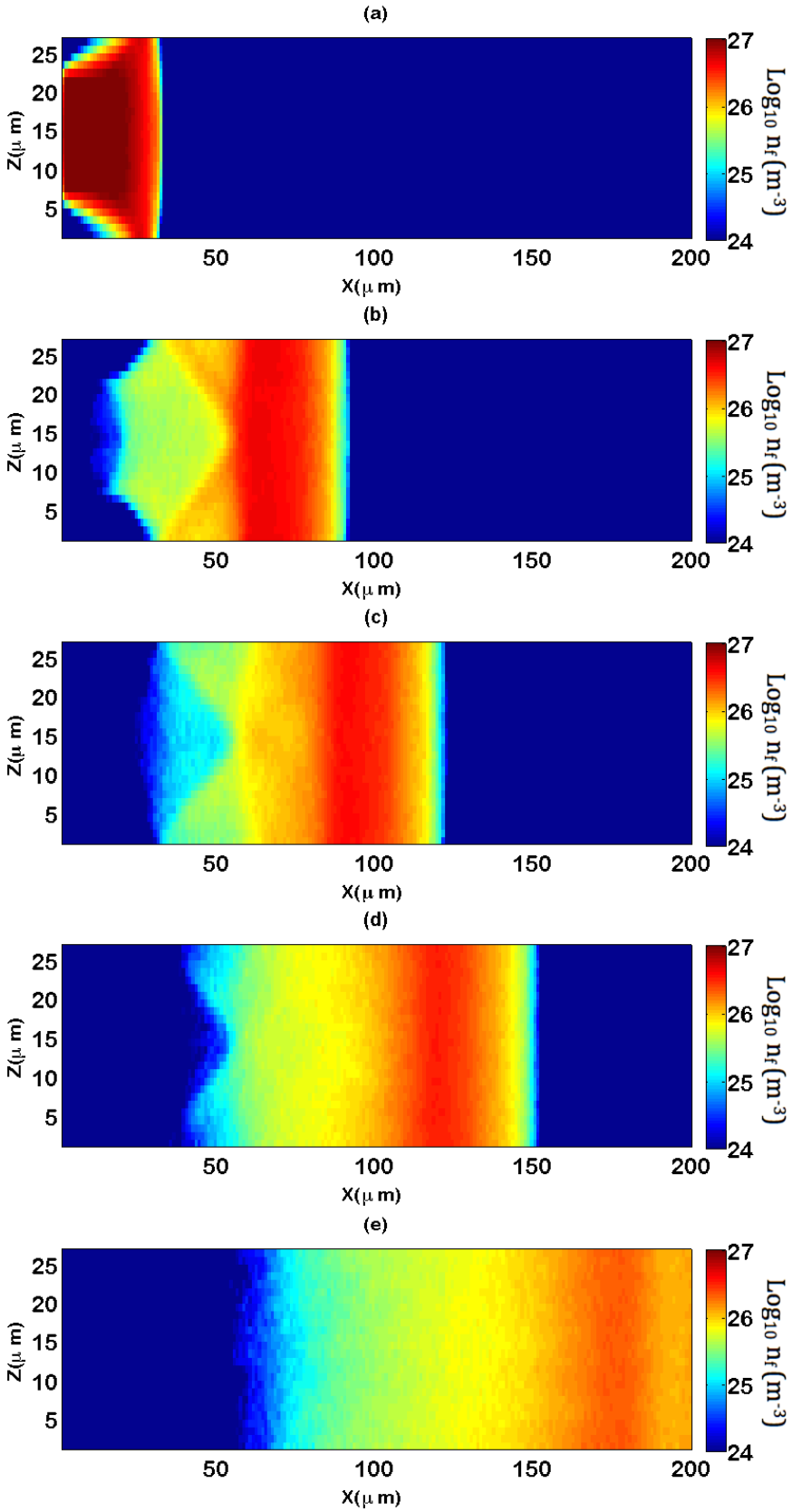

Figure 4.7: log_{10} fast electron density in (m^{-3}) at (a)100 fs, (b)300 fs, (c)400 fs, (d)500 fs and (e)700 fs respectively along x-direction of simulation box.

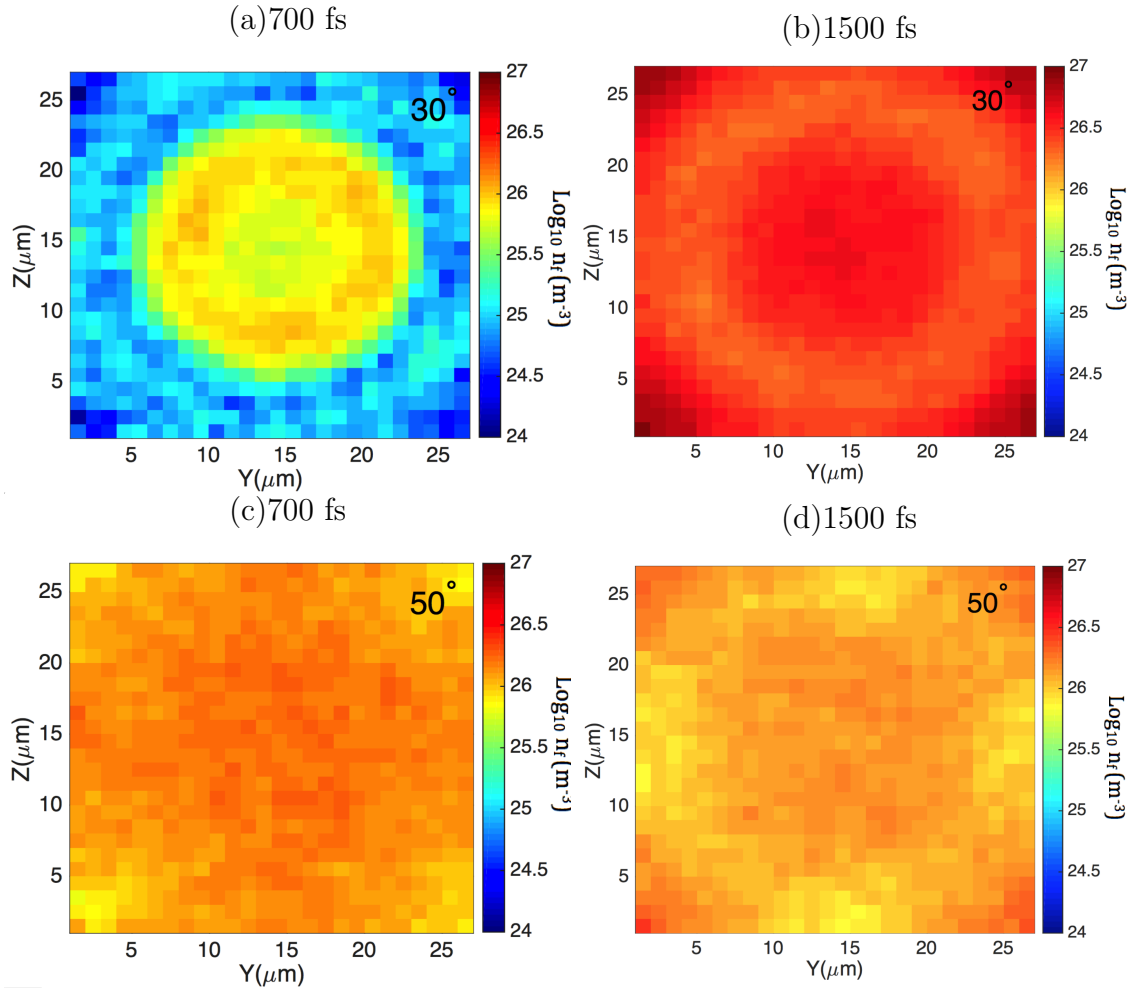

Figure 4.8: (a) Z-Y Slices of the fast electron density across $x = 30$ μm log_{10} in (m^{-3}) for $\theta_d = 30°$ and $50°$. Figures (a) and (b) for $30°$ at 700 fs and 1500 fs respectively whilst Figures (c) and (d) for $50°$ at 700 fs and 1500 fs respectively.

with a lower divergence angle. Based on (4.5), the penetration depth can reach $L_0 \approx 420$ μm and $L_0 \approx 300$ μm for Targets A and B respectively. However, these penetration depths exceed the longitudinal size of the target which is 200 μm, but despite this the heating in Figure 4.3 for Targets A and B is non-uniform. The reason for this is that the penetration depth in (4.5) does not take into account the effect of the reduction in the fast electron density due to the dispersion. This reduction is significant as suggested by (4.7). In addition, there is electric field inhibition which also has a role in the reduction of fast electron density across the depth in Targets A and B. Thus, the penetration depth (4.5) exceeds the longitudinal size of the target due to not including other effects that reduce the fast electron density. Both angular

dispersion and electric field inhibition are responsible for the significant temperature gradients and this is discussed later in Section 4.5.

4.4.5 Effect of angular dispersion on fast electron density

To precisely assess the role of angular dispersion on fast electron density, three simulations were performed using Target A geometry. All the simulations are, with $\theta_d = 50^\circ$ or $\theta_d = 0^\circ$, without including the magnetic field evolution since self-resistive magnetic field can cause a pinch for the fast electrons near the injection region. However, the electric field inhibition was included in these simulations and fast electron beam duration was 500 fs and the mean fast electron energy was 2.7 MeV. Two simulations, with $\theta_d = 50^\circ$ and $\theta_d = 0^\circ$, ignored the effect of the acceleration due to the Lorentz force and the effects of scattering and drag collision. The third simulation is with $\theta_d = 0^\circ$ but with including the effects of the Lorentz force, scattering and drag collision. The purpose of the third simulation is to assess the role of these latter effects on the fast electron density along x-direction. The results are shown in Figure 4.9. This Figure shows the behaviour of fast electron densities along the x-direction plotted using a logarithmic density scale. Generally, there is a reduction in the fast electron density when $\theta_d = 50^\circ$ is used. The difference in this reduction is 70% at $x = 50$ μm compared to $\theta_d = 0^\circ$ (black dot-dashed line-Test 1). Some of the fast electrons are confined near the injection region at $x = 10$ μm in all simulations. This is due to the electric field inhibition.

The electric field potential energy $\Delta\Phi$ was estimated in these simulations with respect to the front target surface at 500 fs using,

$$\Delta\Phi = e \int_1^{160} E dx \tag{4.8}$$

where e is the electron charge and $x = 160$ μm is the maximum distance that the fast electrons reach at 500 fs. The integration of (4.8) over x was performed using

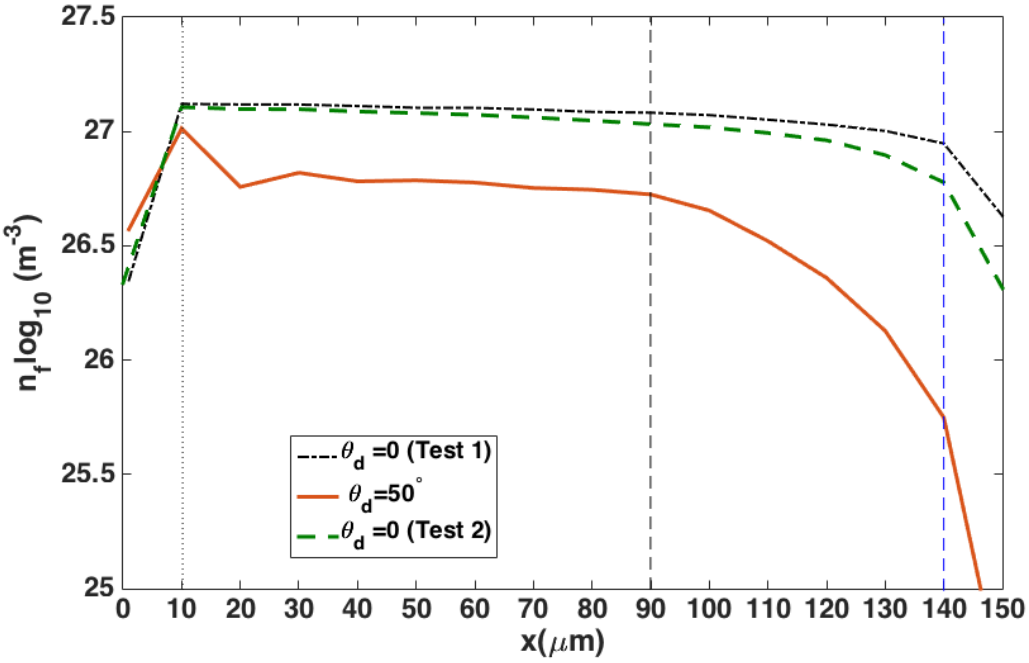

Figure 4.9: Plot of the fast electron densities at 500 fs in the longitudinal direction using Target A geometry. The black dot-dashed line shows the densities when $\theta_d = 0$ (Test 1) and the red solid line when $\theta_d = 50°$. Neither simulation includes the resistive magnetic field, the Lorentz force or drag and scattering. The green dashed line shows the density when $\theta_d = 0$ where Lorentz force, drag and scattering are included (Test 2). The black dotted line at $x = 10$ μm shows the peak of the fast electron densities and where the electric field inhibition effect is dominant. The black dashed line at $x = 90$ μm shows at which distance the reduction in the fast electron density becomes significant. The blue dashed line at $x = 140$ μm shows the end of the length of the fast electron beam.

the trapezoidal integration method. It was found that $\Delta\Phi \approx 0.55$ MeV in all the simulations. The 0.55 MeV of electric field potential energy indicates that energetic electrons with energy lower than ≈ 0.55 MeV are confined at this region. Beyond $x = 10$ μm as shown in Figure 4.9, the fast electron density remains high along the x-direction when $\theta_d = 0$ (black dot-dashed line - Test 1), the Lorentz force, scattering and drag collisions cause a slight reduction (green dashed line - Test 2). A strong reduction with slight fluctuations between $x = 10 - 40$ μm is noticed when $\theta_d = 50°$ (red solid line). The reduction in red solid line is due to the angular dispersion since this is the only effect included in this simulation. More noticeable reduction occurs beyond $x = 90$ μm in the red solid line ($\theta_d = 50°$) compared to the black dot-dashed

and green dashed lines ($\theta_d = 0°$) again due to angular dispersion. The difference between the fast electron density without angular dispersion (black dot-dashed and green dashed lines) increases with distance due to Lorentz force, drag and scattering effects. These effects reduce the fast electron density along x-direction but not as large as the angular dispersion. After $x = 140$ μm, a steep drop in the fast electron density was noticed. This steep drop is expected since the length of the fast electron beam using 500 fs duration is $c\tau_0 = 150$ μm. However, this drop is steeper when angular dispersion is significant.

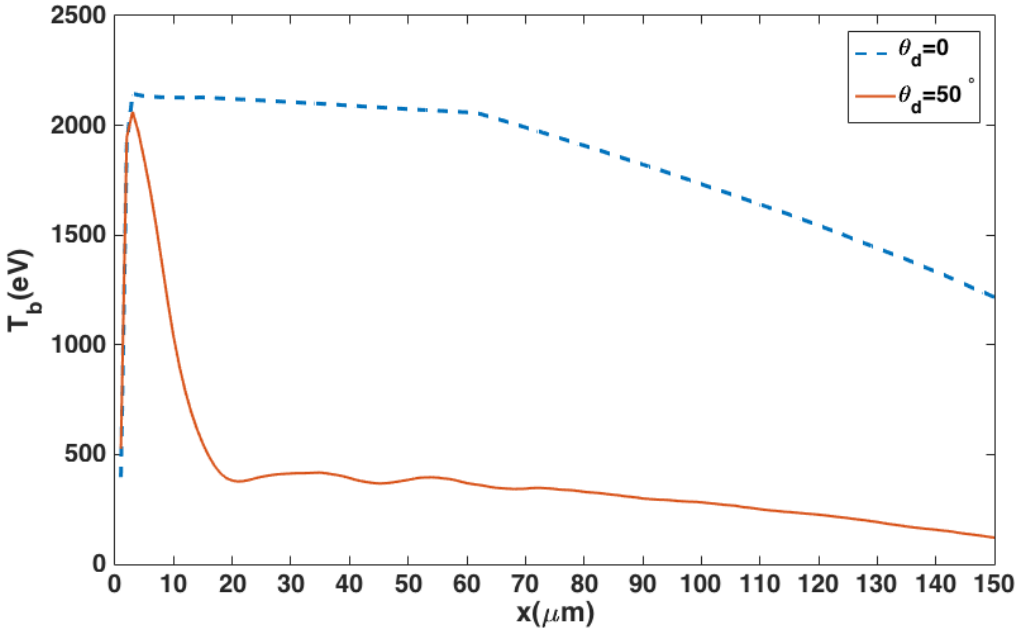

Figure 4.10: Line-out of background temperature in the units of eV from the simulation with $\theta_d = 0$ (blue dashed line) and $\theta_d = 50°$ (red solid line) along x-direction from the target surface until $x = 150$ μm at 700 fs.

The effect of the dispersion on the target heating is shown in Figure 4.10. This Figure shows a line-out of the background temperature in eV from $\theta_d = 0°$ (Test 1) and $\theta_d = 50°$, i.e. with and without angular dispersion, along the x-direction at 700 fs. The very large reduction in background temperature is due to angular dispersion. This reduction is about a factor of 4 compared to without angular dispersion (blue dashed line).

4.5 Longitudinal effects impeding the fast electron penetration

As described in Section 4.2, the electric field inhibition impedes fast electron penetration along the laser beam axis. In Section 4.4, the angular dispersion also reduces the fast electron density and heating power more strongly than the effects of Lorentz force, drag and scattering. The angular dispersion effect was inferred from the increase in the length of the fast electron beam (see Figure 4.7). In all of the simulations in this chapter the fast electron spreading was controlled by restricting the transverse size of the target and making this size comparable to the source diameter size. Therefore, the reduction in the fast electron density in the longitudinal direction is mainly due to electric field inhibition and an angular dispersion. In this section, a numerical study is presented to determine which of the electric field inhibition and angular dispersion has the more significant effect.

The drop in fast electron density due to the large growth of the electric field has been estimated analytically by Bell *et al.* [21] as,

$$n_f = n_0 \left(\frac{t}{\tau_L} \right) \left(\frac{x_0}{x + x_0} \right)^2 \tag{4.9}$$

where n_0 is the fast electron density at source, t is the time after the end of the laser pulse, τ_L is the laser pulse duration, x is the distance from the target surface and x_0 is the fast electron penetration depth, which is given in the case of the Al target as,

$$x_0 = \beta^{-1} \left(\frac{I_L}{10^{18}\ \mathrm{Wcm^{-2}}} \right)^{-1} \left(\frac{T_f}{0.2\ \mathrm{MeV}} \right)^2 \left(\frac{\eta}{10^{-6}\ \Omega.\mathrm{m}} \right)^{-1} 12\ \mu\mathrm{m} \tag{4.10}$$

where β is the fraction of laser energy coupled to the fast electrons. The depth x_0 in (4.10) depends on the resistivity and is inversely proportional to the resistivity. The electric field inhibition becomes dominant when the resistivity is near to its peak [21, 70]. This model is estimated using fixed temporal and spatial resistivity.

Therefore, the level of electric field inhibition anticipated in an experiment is numerically assessed by predicting the time-dependent electric field and resistivity. From this, the fast electron density and the associated electric field are computed along the x direction. Target A geometry was used in this study.

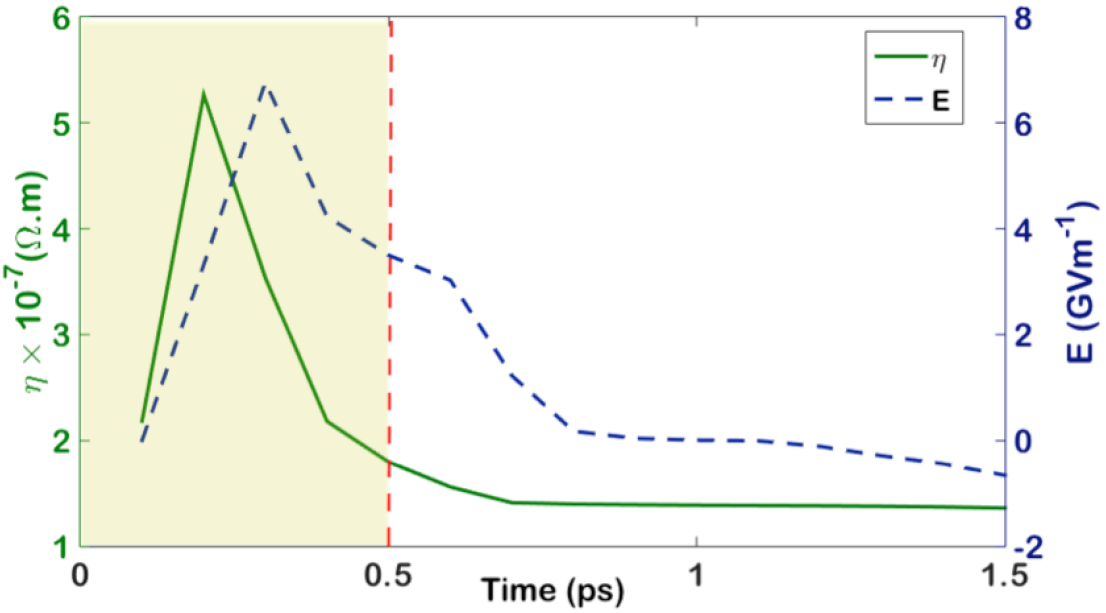

Figure 4.11: Plot of the mean of the resistivity (left axis, green solid line) and of the mean of electric field (right axis, blue dashed line) as function of time at $x = 50$ μm and mid y-axis. The red dashed line at t = 0.5 ps indicates the end of the laser pulse duration.

Figure 4.11 shows both the mean of the resistivity (left axis, green solid line) and of the electric field (right axis, blue dashed line) as a function of time at $x = 50$ μm and in mid y-direction. The resistivity rises quickly during the laser pulse. This is indicated by the shadow area in the Figure. This rise is due to the strong collisions. The resistivity reaches a peak of $5 \times 10^{-7}\Omega.m$ at 200 fs. After this, it drops over time and then remains nearly constant just after the end of the laser pulse of 500 fs. This time dependent is driven by target heating at $x = 50$ μm. The electric field rises during the laser pulse, reaching a peak of ≈ 7 GVm^{-1} at 300 fs. Then it decreases gradually, reaching a new low constant value after 700 fs. It can be seen that the electric field is high during the laser pulse and peaks ≈ 100 fs after the resistivity. Then its strength drops and more slowly than the resistivity. Therefore, the electric

field as inhibitor is limited in Al target due to the reduction in the resistivity. This is experimentally observed in [70].

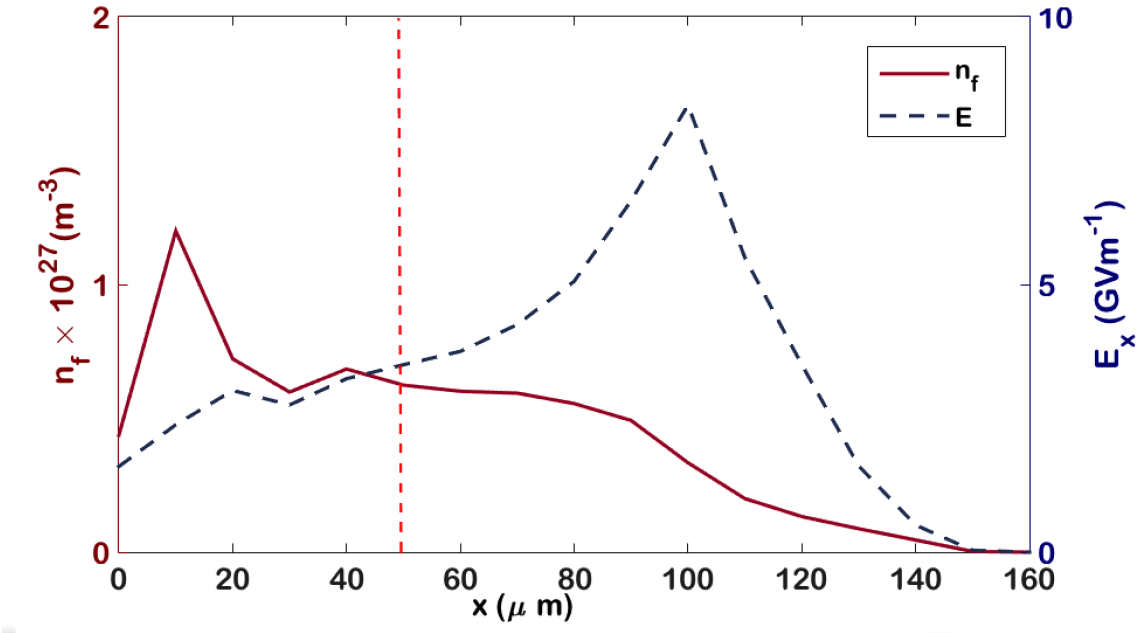

Figure 4.12: Plot of the mean of the fast electron density (left axis, solid line) and of the electric field (right axis, dashed line) and in the longitudinal direction at 500 fs. The red dashed line at $x = 50$ μm indicates the position of the information of Figure 4.11.

To assess this limitation as function in distance, both the longitudinal fast electron density (left axis, solid line) and the longitudinal electric field (right axis, dashed line) are plotted along the x-axis at 500 fs, i.e. at the end of the laser pulse, and shown in Figure 4.12. At this time of 500 fs, the mean of electric field strength and of resistivity are 3.5 GVm^{-1} and $2 \times 10^{-7} \Omega.m$ respectively. The fast electrons penetrate from the left to the right in this Figure. Some of the fast electrons are peaked 10 μm. This is near the target surface. The fast electron density penetrate longitudinally to a distance of ≈ 150 μm. In addition, there is a spike of the electric field, which is about ≈ 8 GVm^{-1} moves into the target and that is close to the fast electron penetration front. This front moves with a velocity of 2×10^8 ms^{-1}. The existence of the fast electron peak at 10 μm indicates the confinement of some of the fast electrons in this region. Using (4.8) with same integration limits, the electric

field potential energy $\Delta\Phi$ at 500 fs is ≈ 0.55 MeV. This energy is low compared to the fast electron mean energy (2.7 MeV). This means that only the fast electrons that have less energy than the electric potential energy will be confined near the target surface. This is illustrated in Figure 4.12, where some of the fast electron density reaches 150 μm, i.e. a distance that is more than half length of the target.

Another test was performed to assess the role of the resistivity in Target A geometry but with resistivity reduced to 30%. The longitudinal fast electron density for a reduced resistivity (black dashed line) and Target A (green solid line) are shown in Figure 4.13 (a) in logarithmic scale. The fast electron densities in both simulations show almost the same behaviour after 20 μm. There is a significant difference in the first 20 μm. This is the region where the electric field inhibition is able to confine the lower energetic fast electrons. According to (4.10), the fast electron penetration depth scales $x_0 \propto \eta^{-1}$ and so with this reduction in resistivity, more fast electrons should penetrate and the fast electron density should remain high. Figure 4.13 (a) shows, however, the differences in the fast electron density with depth are minor despite the large reduced resistivity. The major difference occurs near the injection region. Further, Figure 4.13 (a) also shows that the fast electron density decreases with the depth, even though the resistivity is low. This reduction is attributed to the angular dispersion. Notice that the $\theta_d = 50^\circ$ in these simulations. If angular dispersion is not important, then the fast electron density should remain high in the reduced resistivity case.

Furthermore, Figure 4.13 (b) shows the fast electron density along the x-direction in Target A (green solid line) and the information of Figure 4.9, $\theta_d = 0$ (Test 1) which is shown here as a blue dashed line and $\theta_d = 50^\circ$ shown as red dot-dashed line, where all resistive magnetic fields, acceleration due to Lorentz force, drag and scattering are turned off and only the effect of the angular dispersion and electric field inhibition are included. Notice that all these effects are included in Target A (green solid line). The red dot-dashed line shows the results when $\theta_d = 50^\circ$ and the

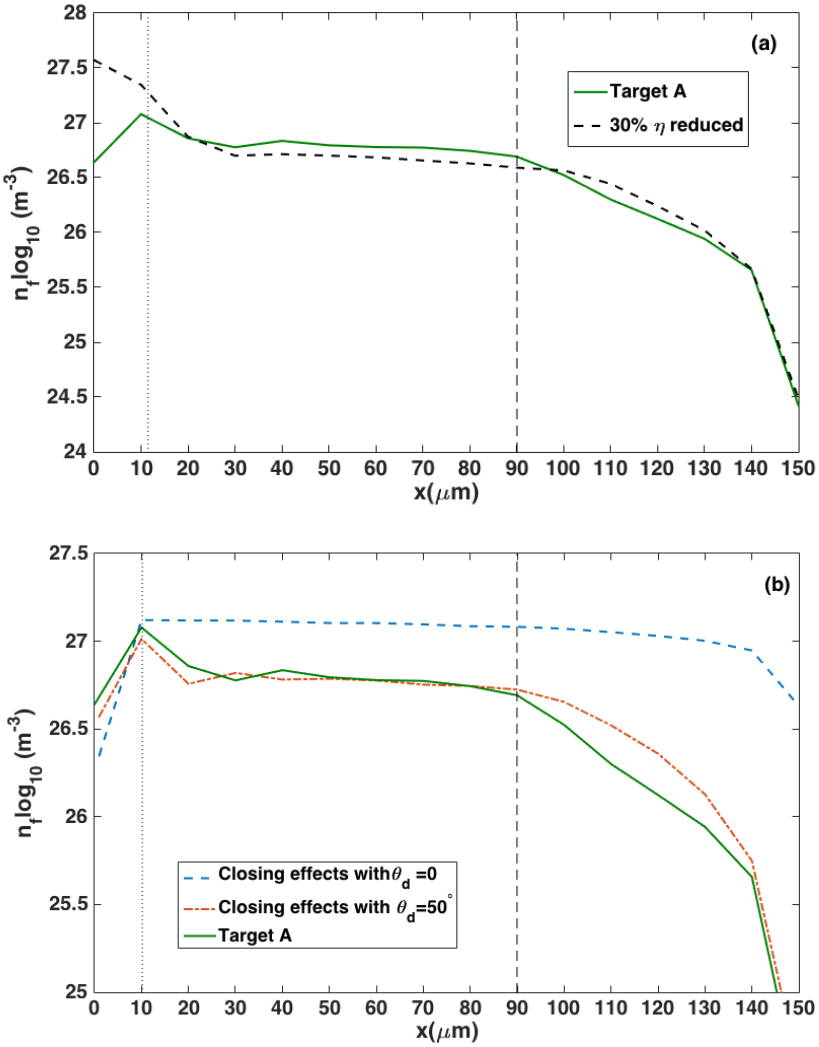

Figure 4.13: (a) Plot of the fast electron densities log_{10} at 500 fs in the longitudinal direction. The black dashed curve shows the simulation with 30% reduction in resistivity using Target A geometry whilst the solid green curve shows simulation of Target A. (b) Plot of the fast electron densities log_{10} at 500 fs in the longitudinal direction. The blue dashed and red dot-dashed curves show the simulation without effects of Lorentz force, scattering, drag collisions and self-resistive magnetic field with $\theta_d = 0°$ and $\theta_d = 50°$ respectively whilst the green solid curve shows simulation of Target A. In both Figures (a) and (b), dotted line at $x = 10$ μm shows where the electric field inhibition is dominant and the dashed line at $x = 90$ μm shows where the angular dispersion effect becomes significant.

blue dashed line when $\theta_d = 0°$. The fast electron densities in the green solid and red dot-dashed lines show almost the same behaviour at the first 90 μm. There is a difference after 90 μm. The fast electron density in Target A (green solid line) is reduced slightly more due to including these effects. However, the reduction is

not large in the comparison with the blue dashed line, where there is no dispersion. We can conclude from this Figure that the main factor reducing the fast electron density is the angular dispersion. From Figures 4.13 (a) and (b), the conclusion is that angular dispersion drives the temperature gradient in fast electron heated target.

4.6 Discussion of the results

The work of this chapter can be divided into three main points:

1. Controlling the fast electron spreading using wire-like target design with transverse directions comparable to the laser diameter spot size:

   The simulations show (Figure 4.3) that this design provides excellent fast electron transverse confinement since fast electron spreading is controlled in the early stages of the interaction. The more comparable the ratio between the transverse directions and the laser diameter spot, the more control of the fast electron spreading is obtained. The transverse uniform heating can be obtained. This could solve the problem of non-uniformity in the transverse directions, since a significant transverse temperature gradient is experimentally observed in these directions even in very thin foil [130]. This design of wire-like target facilitated the heating with depth. Over long propagation distances filamentation can break-up the beam even in these geometries, especially when the beam duration is in the order of ps. This will impair the heating uniformity.

2. Studying the effect of angular dispersion on longitudinal fast electrons penetration and target heating:

   The angular dispersion of the fast electrons is significant, especially after the end of the beam injection or equivalently the end of the laser pulse (4.3). Larger penetration depth L_0 due to the beam divergence is obtained when a

lower divergence angle and longer beam duration are used. This provides more uniformity in heating. However, the dispersion also has a quadratic effect on Ohmic heating, which reduces the heating rate significantly (4.7). Since L_0 in (4.5) does not include the effect of this reduction in n_f, (4.5) overestimates the actual penetration depth. This needs to be corrected in the theory and is ongoing work. Excepting (4.5), the analytical work agrees with the simulation in Sections 4.4.2 and 4.4.3 and with the temperature plots in Figure 4.3. The dispersion reduces the longitudinal heating rate and results in strong temperature gradients. The effect of dispersion on the fast electron density is also studied, where the resistive magnetic fields, the Lorentz force and the drag and scattering are all turned off. It was found that the reduction on the fast electron density is massive with $\theta_d = 50^\circ$ compared to an identical simulation with $\theta_d = 0$, especially after 90 μm. The angular dispersion in this case reduces the heating by a factor of 4.

3. Investigating both electric field inhibition and angular dispersion to determine which is more significant:

   The electric field inhibition was assessed numerically in wire-like geometry and any reduction in the fast electron density with the depth of the target is due to both the electric field inhibition and angular dispersion. Figure (4.12) shows that fast electrons are confined near the target surface or injection site at 10 μm. This is the region where the electric field inhibition is dominant. The electric field is able to inhibit fast electrons with energy below the electric potential energy. Reduction in the resistivity to 30% does not increase the penetration of the fast electron density and the behaviour of the fast electron density along the x-direction is almost the same as in the target that is anticipated in an experiment. If the angular dispersion is not important, then the fast electron density should remain high in the case of reduced resistivity. The reduction in fast electrons is mainly due to the angular dispersion since

we found the effect of the resistive magnetic field, the Lorentz force, drag and scattering taken all together reduce the fast electron density, but not as much as does in the angular dispersion.

4.7 Summary

In this chapter, the concept of extreme fast electron transverse confinement has been introduced along with a numerical demonstration. Then the angular dispersion of the fast electrons is investigated and compared to the electric field inhibition effects in terms of their effects on the longitudinal fast electron penetration and target heating.

The discussion in this chapter indicates that the angular dispersion of the fast electrons must not be neglected in the fast electron transport calculations and indeed requires thorough consideration. This dispersion has great implications for the longitudinal target heating and is the most significant cause for strong temperature gradient along the propagation direction for extended targets. This could affect, for example, fast ignition if any significant dispersion occurs prior to the coupling of the compressed fuel and fast electrons.

Chapter 5

Resistive interface guiding of fast electron propagation

5.1 Motivation

In the preceding chapter, a wire-like target was used to control the spreading of a fast electron beam with significant divergence. This design creates excellent transverse confinement of the fast electrons when the transverse directions of the wire-like target are comparable to the laser diameter spot size (Section 4.3). Similar control of fast electron spreading is possible using a resistive guiding structure [60, 74]. This structure is based on exploiting resistivity gradients produced by using different Z materials in order to guide and focus fast electrons. This is beneficial to applications such as Fast Ignition [31] where the energetic fast electrons need to be transported through stand-off distance of 100 μm [27] and deposited into the compressed core of DT plasma. Recently, the resistive guide use has also been suggested as a driver in hydrodynamics experiments [74]. However, more work needs to be done to improve the fast electron propagation and heating along the depth of the guide. The formation of the magnetic field within the guide close to the axis is observed in [74, 75, 131] independent the guide geometry. The development of these " interior" fields in the target interior is due to inhomogeneous propagation of the

fast electrons. These interior fields produce a strongly annular transport pattern which leads to heating only the outer surface of the guide while its middle remains relatively cold. This affects the attempt to produce uniform heating. Although the results of [74] show that using a guide with a radius comparable to the laser spot radius can mitigate to some extent this problem and improve the heating, this condition might be impractical if one considers the problem of the limited pointing stability of the laser systems [72]. If the laser hits the edge of the resistive guide rather than its centre, the guide will not achieve its aim as a collimator and the fast electrons will transport into the surrounding material. Therefore, a larger radius guide is needed.

There are two types of resistive guide have been investigated in [60, 74]; standard and multilayered resistive guides. A standard resistive guiding scheme [74] is based on embedding a pure, high-Z material in terms of wire or strip into the core of a pure low-Z target (i.e. solid substrate) whilst a multilayered resistive guide [60] uses materials of different atomic number Z in such a way that gradient in resistivity is created from the core of the wire to its cladding and this wire is embedded into pure, low-Z solid substrate. Hitherto, a sharp interface is produced by engineering between the guide and solid substrate in these both schemes. The work of this chapter shows numerically that grading the atomic number at the interface between the guide and solid substrate of these schemes minimises the formation of the interior magnetic field, leading to improvement in heating of guide core. This solves the problem of poor heating into a larger guide radius. In addition, more powerful, faster confining magnetic fields can be obtained with this graded interface configuration. Higher magnetic flux density is obtained in standard resistive guide while larger magnetic field width is obtained in multilayered resistive guide in case of using graded interface configuration. In this chapter, the focus is on improving the uniformity of the fast electron propagation and subsequently the heating in these schemes using the graded interface configuration.

The chapter begins with a discussion of the theory of resistive guide. This is followed by a summary of the results of recent published numerical investigations attempting to improve resistive guide heating [74, 75]. Then the effect of grading the atomic number at the interface between the guide and the solid substrate is numerically investigated in both standard and multilayered resistive guide schemes. A general discussion of the chapter results is given, followed by a summary of the chapter.

5.2 Resistive guiding concept

5.2.1 The theory

Plasma resistivity induces a significant magnetic field inside an overdense plasma when a resistivity gradient or shear in the fast electron current density exists. This is described (see Section 2.3.5) by the following induction equation in the hybrid approximation [73]:

$$\frac{\partial \mathbf{B}}{\partial t} = \eta(\nabla \times \mathbf{j}_f) + (\nabla\eta) \times \mathbf{j}_f \tag{5.1}$$

Resistive guiding concept was initially introduced by Robinson and Sherlock [60] to enable the magnetic collimation of fast electrons. They proposed fabricating a solid target in which a high-resistivity material is embedded into the core of a low-resistivity solid target as a strip or a wire, as shown in Figure 5.1. This creates a resistivity gradient in a direction which is transverse to that of the fast electron beam propagation. Thus, according to the second term on the right-hand-side of (5.1), an azimuthal magnetic field will be produced at these gradients. This will collimate the fast electrons to the higher resistivity region and guide them along the core.

The dynamics of the collimation process are as follows: at the early stages of the laser interaction, the $(\nabla\eta) \times \mathbf{j}_f$ term initiates collimation of the fast electrons by producing a strong azimuthal magnetic field. This pushes the fast electrons into

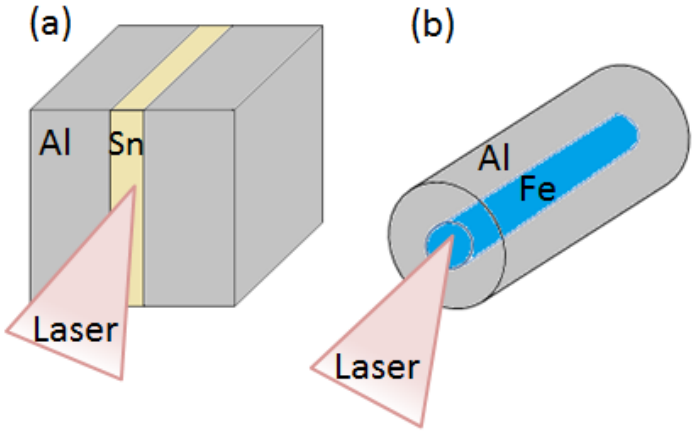

Figure 5.1: A diagram of the structured resistivity guiding. (a) shows the design used by Kar *et al.* [2] and (b) shows that used by Ramakrishna *et al.* [3].

a higher resistivity region. The temperature of the guiding region increases to over 100 eV due to return current heating and the collimation of the fast electrons. Because of this, the resistivity of the guide, which follows Spitzer (2.23), reduces and as it becomes less than that of the surrounding target. The$(\nabla\eta) \times \mathbf{j}_f$ term reduces and eventually reverses. This reduces the magnetic field and could expel the fast electrons from the guide when the magnetic field reverses. However, the collimation due to $(\nabla\eta) \times \mathbf{j}_f$ causes a shear in the fast electron current density inside the guide $\eta(\nabla \times \mathbf{j}_f)$. This collimation offsets the magnetic reversal and reinforces the collimated magnetic field, prolonging the collimating effect. Solodov *et al.* [132] found numerically that the reversal of the resistivity gradient effect occurs less than 0.5 ps after the beginning of the laser pulse. They embedded a Cu wire into an Al wire-like target. However, even with this reversal, they stated that around 65% of the injected fast electrons collimated up to 150 μm depth. Robinson and Sherlock [60] show that in the case of low-Z guiding embedded into a high-Z target, a decollimating magnetic field is generated. This magnetic field expels the fast electrons from the guide. The concept of resistive guiding has been experimentally demonstrated by Kar *et al.* [2] and by Ramakrishna *et al.* [3]. In the experiment of Kar *et al.*, a tin (Sn) strip layer was placed between two large Al slabs (shown in Figure 5.1(a)). Ramakrishna *et al.*

used an iron (Fe) wire embedded into an Al cylindrical geometry (shown in Figure 5.1(b)). Both experiments show evidence of fast electron collimation along the path of the guide, regardless of the target geometry.

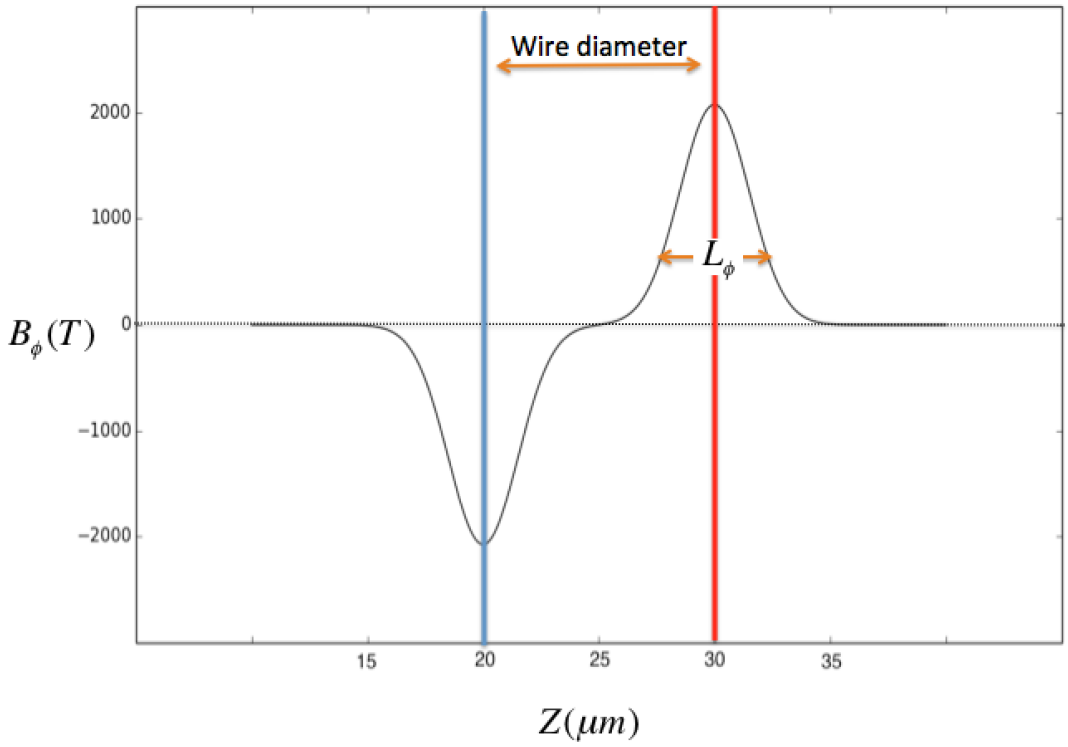

Figure 5.2: A diagram of the azimuthal magnetic field B_ϕ in (T) and its width L_ϕ in (μm) as function of distance. The red and blue lines at $z = 20$ μm and $z = 30$ μm show the direction of the field.

The ability of the guide to confine the fast electrons depends on the ratio of the fast electron Larmor radius r_g to the generated azimuthal magnetic field width L_ϕ. It is assumed that the azimuthal magnetic field of the guide B_ϕ has a uniform Gaussian profile as shown in Figure 5.2 and its width L_ϕ is the FWHM of this profile. The red and the blue lines $z = 20$ μm and $z = 30$ μm respectively show the positive (counter clockwise) and negative (clockwise) direction of the azimuthal magnetic field respectively. The guide diameter is also shown in the Figure 5.2. The fast electrons travel on a helical trajectory inside the guide with a radius that is

defined as,

$$r_g = \frac{\gamma m_e c}{eB_\phi} \tag{5.2}$$

where γ is the Lorentz factor and B_ϕ is the uniform azimuthal magnetic flux density. Thus, the confinement condition of the fast electrons along the guide is,

$$B_\phi L_\phi \geq \frac{\gamma c m_e}{e}(1 - \cos\theta_d) \tag{5.3}$$

This implies that the product of $B_\phi L_\phi$ needs to be larger than the fast electron momentum ($P_f = \gamma c m_e$) to reflect the fast electrons back towards the guide axis. The limit to confinement ensures that the fast electron circular segment just touches the far side of the confining region. The typical value of the product $B_\phi L_\phi$ to confine the fast electrons is about 10^{-3} Tm [74]. This $B_\phi L_\phi$ product and (5.3) condition are studied in the two schemes in this chapter.

5.2.2 The heating

Strong heating occurs where the beam is collimated. As the fast electrons are confined into a guide, the material is rapidly heated due to Ohmic heating to over 100 eV over a distance without significant heating of the surrounding materials. Robinson *et al.* [74] have investigated analytically and numerically the most significant parameters that improve the heating of a pure Z resistive guide with a sharp interface. The geometry of the guide in their investigations was a pure Al cylindrical wire embedded into a CH_2 target. The CH_2 target dimensions were $300 \times 100 \times 100$ μm and a 10 μm Al wire was centred in the mid y and z directions. They expressed the relation between the heating parameters in term of pressure as,

$$P_{wire} \propto \frac{Z n_i^{3/5} \beta^{4/5} I_L^{2/5} \tau_L^{2/5}}{\lambda_L^{4/5}} \tag{5.4}$$

where P_{wire} is the electron pressure produced in the guide, n_i is the ion density, β is the fraction of the laser energy coupled to the fast electrons, I_L is the laser intensity, τ_L is the laser pulse duration and λ_L is the wavelength of the laser.

In their analytical work of (5.4), they have assumed that the main heating mechanism is Ohmic heating with resistivity provided by the Spitzer model (2.23) and the fast electrons are perfectly confined by the guide. To support their analytical conclusion (5.4) several simulations were run and the following results were obtained,

- Shorter λ_L improves the heating with the depth by a factor of 3 if $\lambda_L = 0.5$ μm is used rather than $\lambda_L = 1$ μm [74].

- A lower divergence angle θ_d increases the heating with depth since the confinement of fast electrons is easier to obtain with lower θ_d compared to larger θ_d.

- Matching the wire radius size to the laser spot radius size, i.e. $r_{wire} = r_{spot}$, gives better heating than the case of $r_{wire} > r_{spot}$. This is due to the fact that the rate of the confining magnetic field becomes higher when $r_{wire} = r_{spot}$.

- Lower intensity and longer laser pulse duration is favoured for good heating.

- Heating is improved linearly with Z only if the material follows the Spitzer resistivity. The effect of the low-temperature resistivity limits the heating in high-Z materials.

- Although (5.4) states that the heating can be improved as it is proportional to $\beta^{4/5}$, optimising β is still an experimental challenge.

Although the relation (5.4) demonstrates the parameters that can improve heating with depth, it does not guarantee any uniformity. The annular heating pattern in the background temperature profiles is observed [74], especially in the case of $r_{wire} > r_{spot}$.

Robinson *et al.* [75] recently proposed using the conical guide structure [133] to heat extended targets. They found that adding an inverse conical taper onto an embedded wire target improves the heating with depth since this structure reduces the angular spread of the fast electrons. Better heating is obtained when the length of the inverse conical taper is large and its half-angle is small.

5.3 Grade interface in Z for the resistive guide

Figures 5.3 and 5.4 show the target Z profile along with the shape of the boundary for the resistive guides that are investigated for standard and multilayered designs respectively. The resistive guide is a cylindrical wire in both schemes. The left-hand columns of Figures 5.3 (a) and (b) show a taken slice from the target Z-profile in the mid y-direction at $10 \leq z \leq 40$ μm for the standard design of the resistive guide. The materials used in Figures 5.3 (a) and (b) are pure Al wire (Z = 13) embedded into a CH (Z = 3.5) solid substrate. The shape of the boundaries between the wire and the solid substrate are shown in the right-hand column of Figures 5.3(a) and (b). As shown, the standard resistive guiding has a sharp interface in Z between the Al wire and CH solid substrate. The difference between Figures 5.3(a) and (b) is only in the wire diameter size, which is 10 μm and 5 μm for (a) and (b) respectively. Figure 5.3(c) in the left-hand column shows a similar design to Figures 5.3(a) and (b), i.e. pure Al wire (Z = 13) embedded into a CH (Z = 3.5) solid substrate, except that the boundary between the wire and the solid substrate is graded in Z. The shape of this grading is shown in the right-hand column of Figure 5.3(c). As shown, the overall diameter of the wire is 10 μm. Between 5 μm and 10 μm, a finite gradient in Z is introduced. This is located between the wire and the solid substrate. Both Figure 5.3(b) and the core in Figure 5.3 (c) have the same mass of Al and thus the heating can be compared between the two designs. However, the design in Figure 5.3(c) provides more tolerance to the pointing stability process since the wire diameter in (c) is twice that in (b).

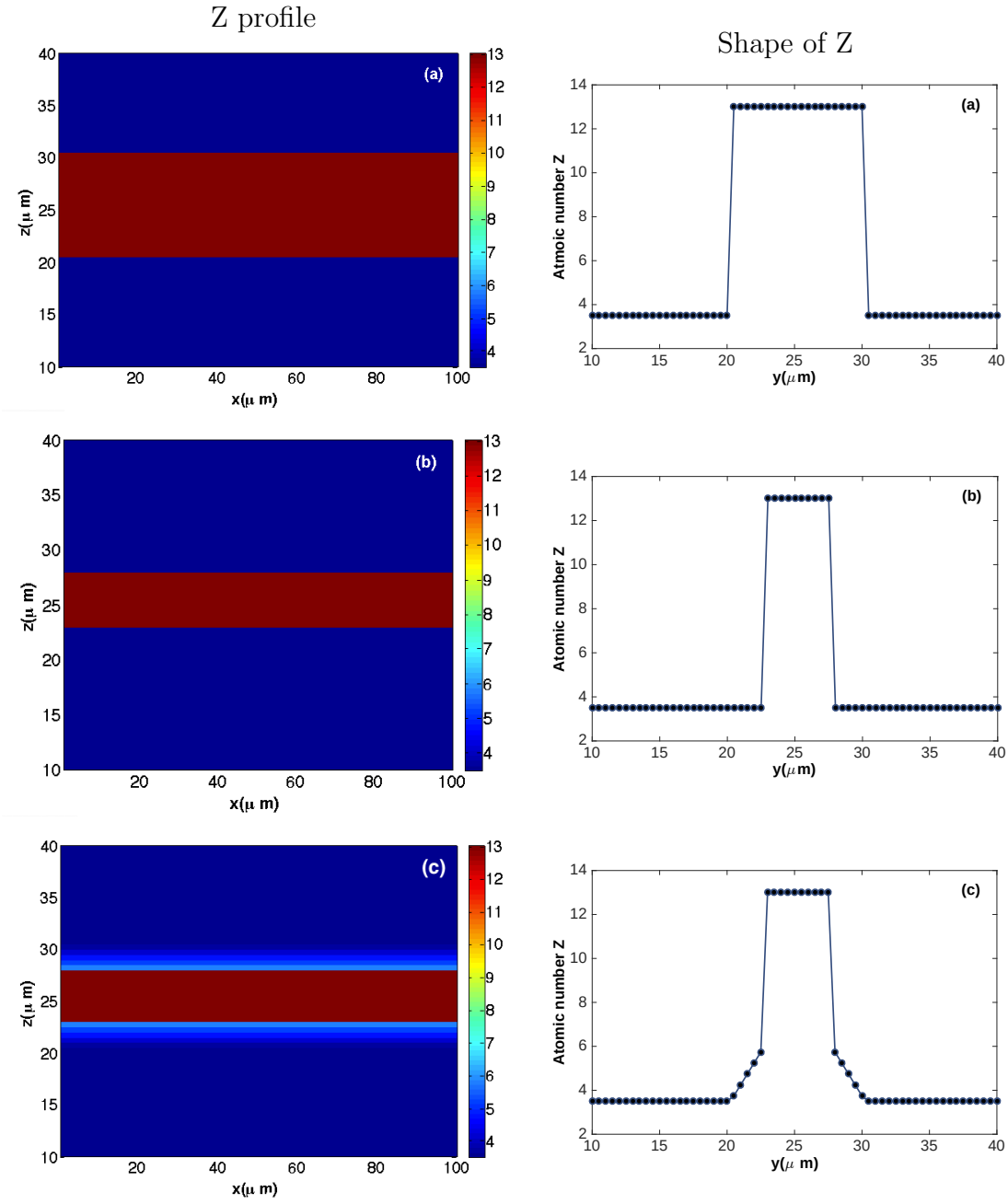

Figure 5.3: The left-hand column shows slices taken for the target Z profile in the mid y-direction at $10 \leq z \leq 40$ μm. The right-hand column shows the shape of the boundary in Z between the wire and solid substrate in the x-z midplane. Designs (a) and (b) are the standard resistive guide with sharp interface. The wire diameter is 10 μm and 5 μm respectively. Design (c) is the standard resistive guide with graded interface in Z. The total wire diameter is 10 μm while the wire diameter that is not graded in Z is 5 μm. The black circles indicate the graded in Z with position.

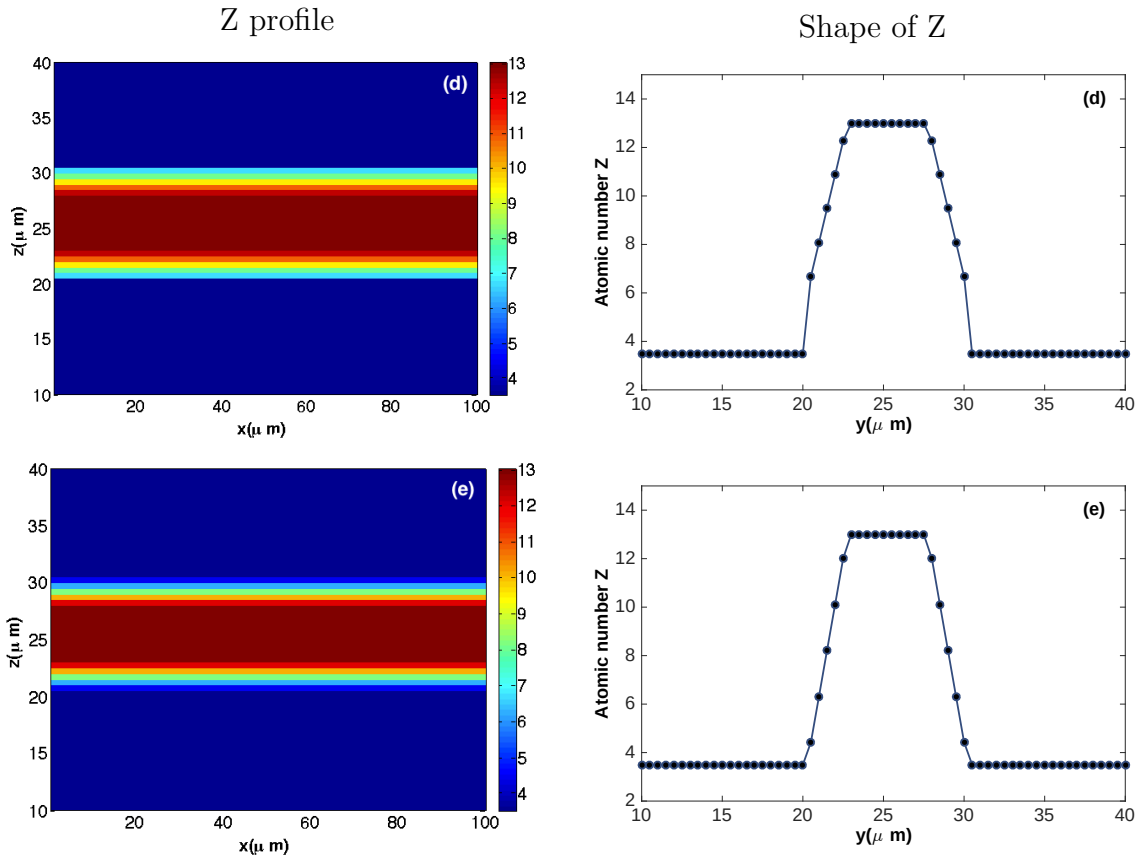

Figure 5.4: The left-hand column shows slices taken for the target Z profile in the mid y-direction at $10 \leq z \leq 40$ μm. The wire diameter in both (d) and (e) is 10 μm. The difference between the two is the shape of boundary in Z shown in the right-hand column, taken in the x-z midplane. Design (d) has a sharp interface while (e) has a graded interface. The black circles indicate the grade in Z with position.

In addition, the effect of grading the interface is also investigated in a multilayered resistive guide design proposed in [60] and it is shown in Figure 5.4. In this design, different Z materials are used in such a way that a gradient in resistivity is created in the wire between the core and the cladding. The composition of the wire is varied between the two different Z materials according to [60],

$$n_i = n_h\psi + n_l(1-\psi) \tag{5.5}$$

$$Z = Z_h\psi + Z_l(1-\psi) \tag{5.6}$$

where h and l are denoted as a high-Z material and low-Z material respectively and ψ is a mixed fraction of materials h and l. The materials used are Al (Z=13) and C (Z=6) for Figure 5.4 (d) and Al(Z=13) and CH(Z=3.5) for Figure 5.4 (e). The form used for ψ is,

$$\psi = \begin{cases} \text{Al} & \psi = 1 \\ \text{C or CH} & \psi = 0 \\ \text{linear interpolation} & 0 < \psi < 1 \end{cases} \tag{5.7}$$

The left-hand column diagrams in Figures 5.4 show a simulation slice of the target Z-profile in the mid y-direction at $10 \leq z \leq 40$ μm for this multilayered scheme. The shape of the boundary between the multilayered-Z wire and the surrounding material can be seen in the right-hand column of Figures 5.4. Figure 5.4 (d) shows a target with a sharp wire-substrate interface and the gradient in Z between Al (Z=13) and C (Z=6) whilst Figure 5.4 (e) shows a grade profile down to CH (Z=3.5),i.e to the substrate. The boundary in this case is shown in the right-hand column of Figure 5.4 (e). Both wires in Figure 5.4 (d) and (e), have the same diameter and a gradient in Z between the core and the cladding. The core in both designs has a 5 μm diameter and is ungraded in Z.

To achieve the best performance from the graded interface configuration, which

is used in (c) in Figure 5.3 and (e) in Figure 5.4, the following relationship needs to be satisfied,

$$\chi = \frac{r_{core}}{r_{spot}} < 1 \tag{5.8}$$

where χ is the ratio of the radius of the core r_{core} to the laser radius spot r_{spot}. r_{core} is the part of wire that has not been graded. The ratio (5.8) needs to be less than 1 for the scheme to achieve its aim, otherwise the confined fast electron beam will break up into filaments inside the guide which will result in transverse non-uniform heating of the wire.

5.3.1 Simulation set-up

Simulations were performed using the 3D particle hybrid code ZEPHYROS. A $200 \times 100 \times 100$ grid was used with a 0.5 μm cell size in each direction. The number of macroparticles injected into each of these cells was 126 to reduce the statistical noise. This is discussed in the Appendix A. The target consisted of a CH substrate within which a wire of radius r_{wire} was embedded. The construction of the wire and its boundary with the CH substrate in each run are summarised in Table 5.1. This wire was co-linear along the x-axis and centred on $y = z = 25$ μm. The laser irradiation intensity was 1.27×10^{20} Wcm^{-2} with a pulse duration of 2 ps, the laser wavelength is 1 μm. It is assumed that 30% of the laser energy was coupled to the fast electrons. The temporal profile of the fast electron beam is top-hat shaped and the transverse profile is $\propto \exp[-\frac{r^2}{2r_{spot}^2}]$, where $r_{spot} = 3.5$ μm. The fast electron angular distribution is uniform over a solid angle and defined by the half-angle of divergence 50°. The energy distribution of the fast electrons is from the reduced Wilks' ponderomotive scaling (2.13), giving $T_f = 2.7$ MeV. The resistivity uses the Lee and More model and a minimum mean free path as $5r_s$.

From Table 5.1, it can be seen that Runs A, C, D and E have $r_{wire} > r_{spot}$. This means the whole of the electron beam source is put into the wire. This is not the case in Run B where $r_{wire} < r_{spot}$. The purpose of performing Run B is to compare

Run	r_{wire} (μm)	r_{core} (μm)	$r_{\text{grade interface}}$ (μm)	χ (5.8)	Target Z Profile (shown in Figures 5.3 and 5.4 respectively)
A	5	5	0	1.4	(a)
B	2.5	2.5	0	0.7	(b)
C	5	2.5	2.5	0.7	(c)
D	5	2.5	0	0.7	(d)
E	5	2.5	2.5	0.7	(e)

Table 5.1: Table of wire geometric parameters.

it with Runs C - E as they have the same r_{core}, i.e. the same mass of Al, although the r_{wire} in Runs C -E is twice that in Run B.

5.3.2 Results

The discussion of the results is divided into three sections as follows. The effect of interface design on the generated azimuthal magnetic fields is investigated first. Then the effect of the resulting azimuthal magnetic field on the guide heating is discussed, and finally, the maximum kinetic energy and largest Larmor radius that confined within each guide is estimated.

5.3.2.1 The azimuthal magnetic field rate

Figure 5.5 shows an x-z slice taken of the magnetic field in units of T in the y midplane at 2.2 ps for Runs A - E. Generally, a strong azimuthal magnetic field has been generated at the interface between the wires and the CH substrate at $20 \leq z \leq 30$ μm. This field provides collimation for the fast electron beam. Radial expansion on the fast electron beam is evident from the formation of the magnetic field outside the wire at the CH substrate.

Some features of a magnetic field are formed within the wire close to the axis noticeable mainly in Runs A and D. Both Runs A and D have $r_{wire} > r_{spot}$ and their wire boundaries with the CH substrate are sharp. The formation of this magnetic field in both runs is due to the inhomogeneous propagation of the fast electrons. In

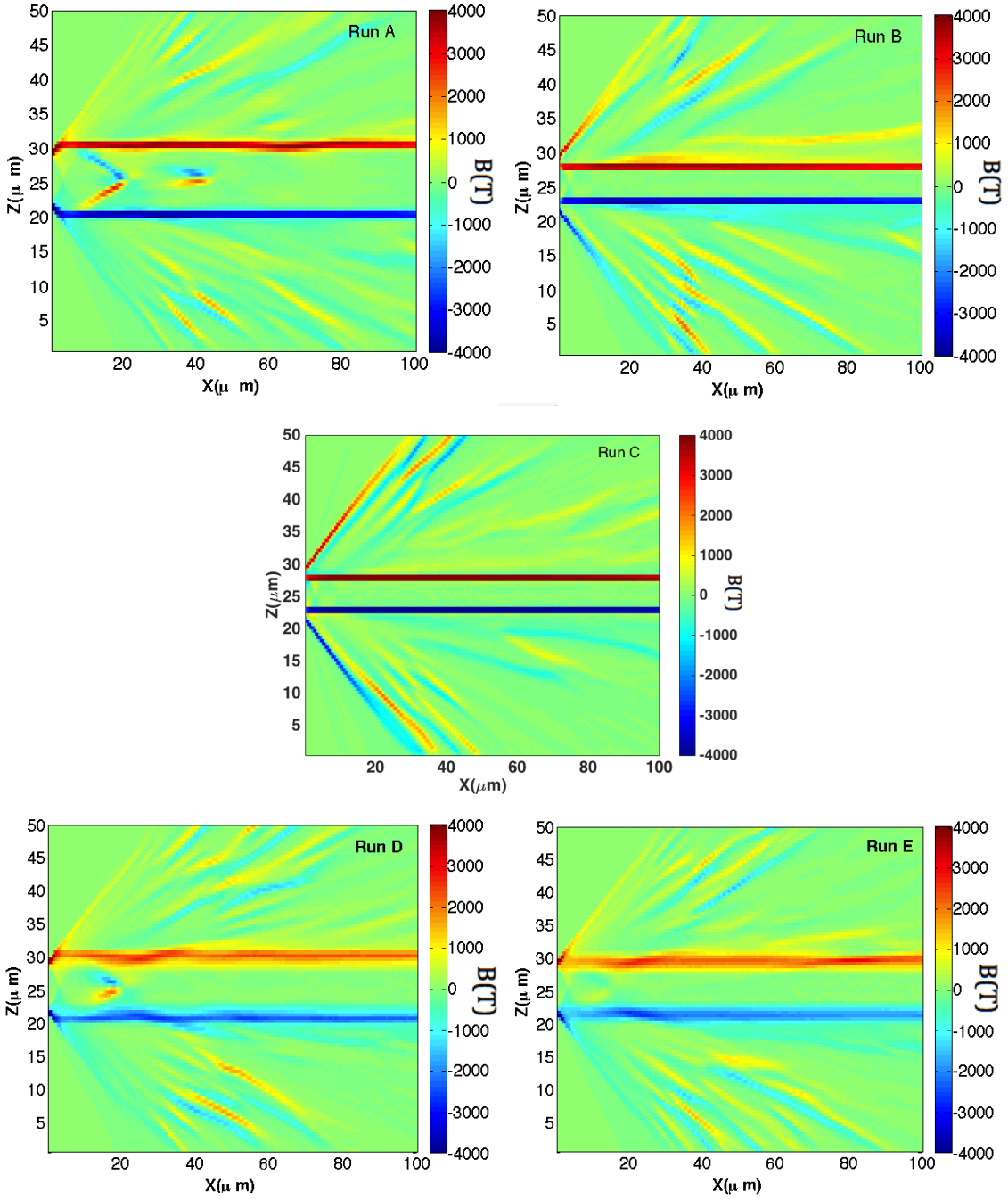

Figure 5.5: x-z Slices taken of the magnetic field in (T) in the y midplane at 2.2 ps. The design of each run and Target Z profile is shown in Figure 5.3 for Runs A-C and in Figure 5.4 for Runs D and E. The wire parameters are summarised in Table 5.1.

the case of Run A, this field is observed at $x = 20$ μm and $x = 40$ μm while it is only observed at $x = 20$ μm in Run D. The difference in the formation of these 'interior' magnetic fields between the two wires is due to the difference in the wire construction

between Run A (pure-Z guide) and Run D (multilayered-Z guide). The generation of these fields within the wire is undesirable and is considered to be inhibiting factor in obtaining uniform fast electron heating in the transverse direction across the guide. The effect of these fields on heating will be discussed in Section 5.3.2.2. The interior magnetic field is not observed in the case of Runs B and C and only weakly observed in Run E. This implies that improved uniformity of the fast electron propagation is obtained in these wires.

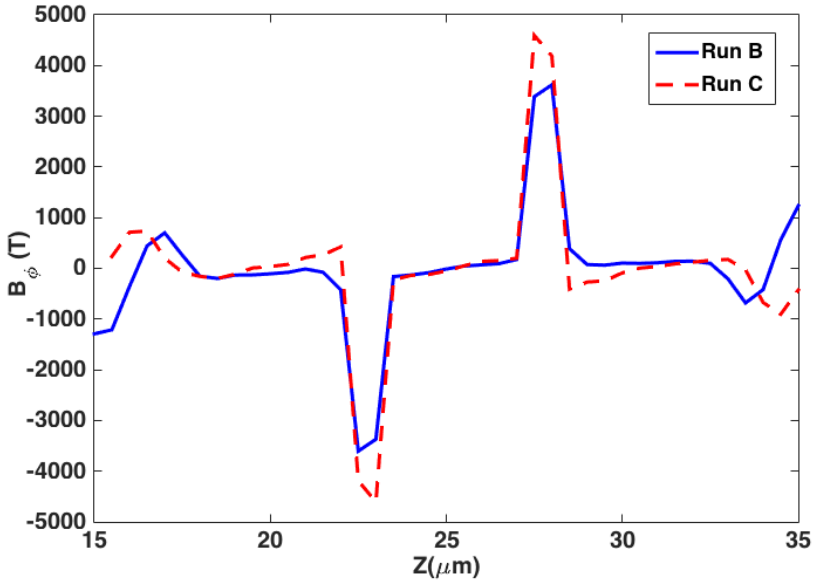

Figure 5.6: Plot of the magnetic field near the head of the wire for run B (solid line) and run C (dashed line), $x = 10$ μm, at $15 \leq z \leq 35$ μm and in the y midplane 2.2 ps.

In addition, the azimuthal magnetic fields in Runs B and C looks similar in Figure 5.5 although the wire radius in Run C is twice that in Run B, see Table 5.1. In Figure 5.5, the diameter of the wire in Run C looks smaller than its actual diameter size (10 μm). The azimuthal magnetic field is generated along the graded region of the wire. The formation of the magnetic fields so close to the core of the wire leads to the azimuthal magnetic being located along the inner edge of the wire. To assess the difference in the azimuthal magnetic field between Runs B and C, line-outs of the azimuthal magnetic fields are taken from each run near the head of the wire, $x = 10$ μm, at $15 \leq z \leq 35$ μm and in the y midplane at 2.2 ps. This is

shown in Figure 5.6. The reverse in the azimuthal magnetic field direction is shown as the positive (counter-clockwise) and negative (clockwise) values. The variation in the magnetic field at $z < 20$ μm and $z > 30$ μm is due to the magnetic fields that are generated by the fast electron expansion in the radial direction. In this Figure, the peak of B_ϕ in Run C (graded interface) is higher than in Run B (sharped interface) by about 1000 T. The difference in the magnetic flux density is calculated at the end of the laser pulse (2 ps) and is found to be higher in Run C than in Run B by 24%. This figure also shows that the FWHM of the magnetic field widths L_ϕ for both Runs B and C are similar. Thus, grading the interface increases B_ϕ and has a minor effect on the width of the azimuthal magnetic field L_ϕ.

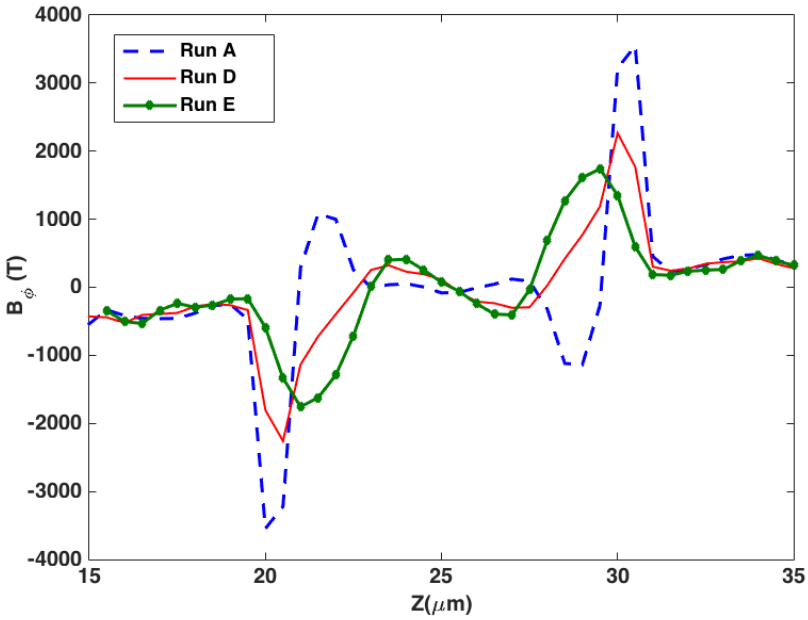

Figure 5.7: Plot of the magnetic field at $x = 10$ μm near the beam injection for runs A, D and E at $15 \leq z \leq 35$ μm and in the y midplane at 2.2 ps.

Figure 5.7 shows a comparison of the line-outs of the azimuthal magnetic fields between Run A and Runs D and E. These lines are taken near the head of the wire, $x = 10$ μm, at $15 \leq z \leq 35$ μm and in the y midplane at 2.2 ps. The magnetic flux density is lower and the width is larger in the case of multilayered-Z wires (Runs D and E) compared to that of pure-Z wire (Run A). Comparing Run A with D where

the interface is sharp, the magnetic field flux density in Run A (pure Z) is higher than in Run D (multilayered Z) by 44% while the width of the field in Run A is smaller than in Run D by 24% at the end of the laser pulse (2 ps). Furthermore, the comparison between Runs D and E, where the difference is only in the shape of wire boundary with substrate, shows that the magnetic flux density in Run D is slightly higher than in E by 26%. However, the magnetic field profile of Run E (green circle-solid line) is smoother compared to that of Run D (red solid line). The width of the magnetic field is larger in Run E than in Run D by 50% at the end of the laser pulse. Thus, grading the atomic number at the interface in the multilayered-Z guide significantly increases the width of the magnetic fields and establish more Gaussian-like profile. This smooth profile affects the heating as it increases the uniformity of the fast electron propagation. This is discussed in Section 5.3.2.2.

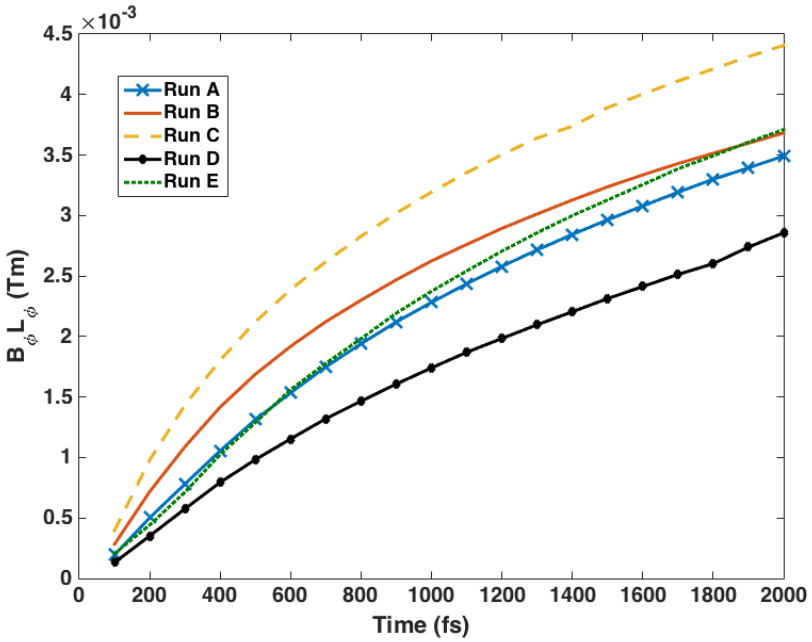

Figure 5.8: Plot of the product $B_\phi L_\phi$ in Tm as a function of time near the head of the wire ($x = 10$ μm) and in the y mid-plane.

Figure 5.8 shows the resulting product $B_\phi L_\phi$ (see Section 5.2) in the units of Tm as a function of time which is estimated near the head of the wire, i.e. $x = 10$ μm, and in the y mid-plane for all the runs. The product $B_\phi L_\phi$ is calculated from the

measurement of the peak of the magnetic field and the FWHM of its width. As shown, Run C gives the highest values of this product. A given value of $B_\phi L_\phi$ of 10^{-3} Tm is obtained at the first 200 fs in Run C while it is obtained later in time at 300 fs in Run B, 400 fs in Runs A and E and finally at 500 fs in Run D. Obtaining this value early in the pulse enhances early collimation of the fast electron beam. This enhanced collimation increases the heating in the wire as more fast electrons are confined. The next highest product is obtained in Run B. The wire radius size in Run B is the same as the core radius size in Run C (i.e. 2.5 μm) and both have the same mass of Al. The reason for $B_\phi L_\phi$ being higher in Run C is likely due to $r_{wire} < r_{spot}$. More fast electrons move into the CH substrate than are confined in the wire in Run B. The product $B_\phi L_\phi$ of Run E (green dotted line) is comparable to that of Run A (blue cross-solid line) at the early time then becomes higher and matches that of Run B (red solid line). This suggests the multilayered Z wire with graded interface configuration produces $B_\phi L_\phi$ values which lie between those observed for large and small diameter pure-Z wires. In addition, the product $B_\phi L_\phi$ of Run E is higher than that of Run D due to the increase in L_ϕ by 50%. This is due to graded the interface between the wire and the CH substrate in Run E. Interestingly, the product $B_\phi L_\phi$ in Run A is higher than in Run D. The 44% difference in B_ϕ between Runs A and D increases the product $B_\phi L_\phi$. Even with this, we find in Section 5.3.2.2 that the heating in Run D is more uniform than in Run A. This results from reduced interior magnetic fields in Run D compared to Run A and the higher fast electron current density in Run D.

5.3.2.2 The fast electron heating

The influence of the resulting azimuthal magnetic field on wire heating in Runs A-E is discussed in this section. Figure 5.9 shows an x-z slice taken of the background temperature in eV in the mid y-direction at 2.2 ps for Runs A-E. Strong heating occurs in the wires where the fast electrons are collimated due to the resistive return

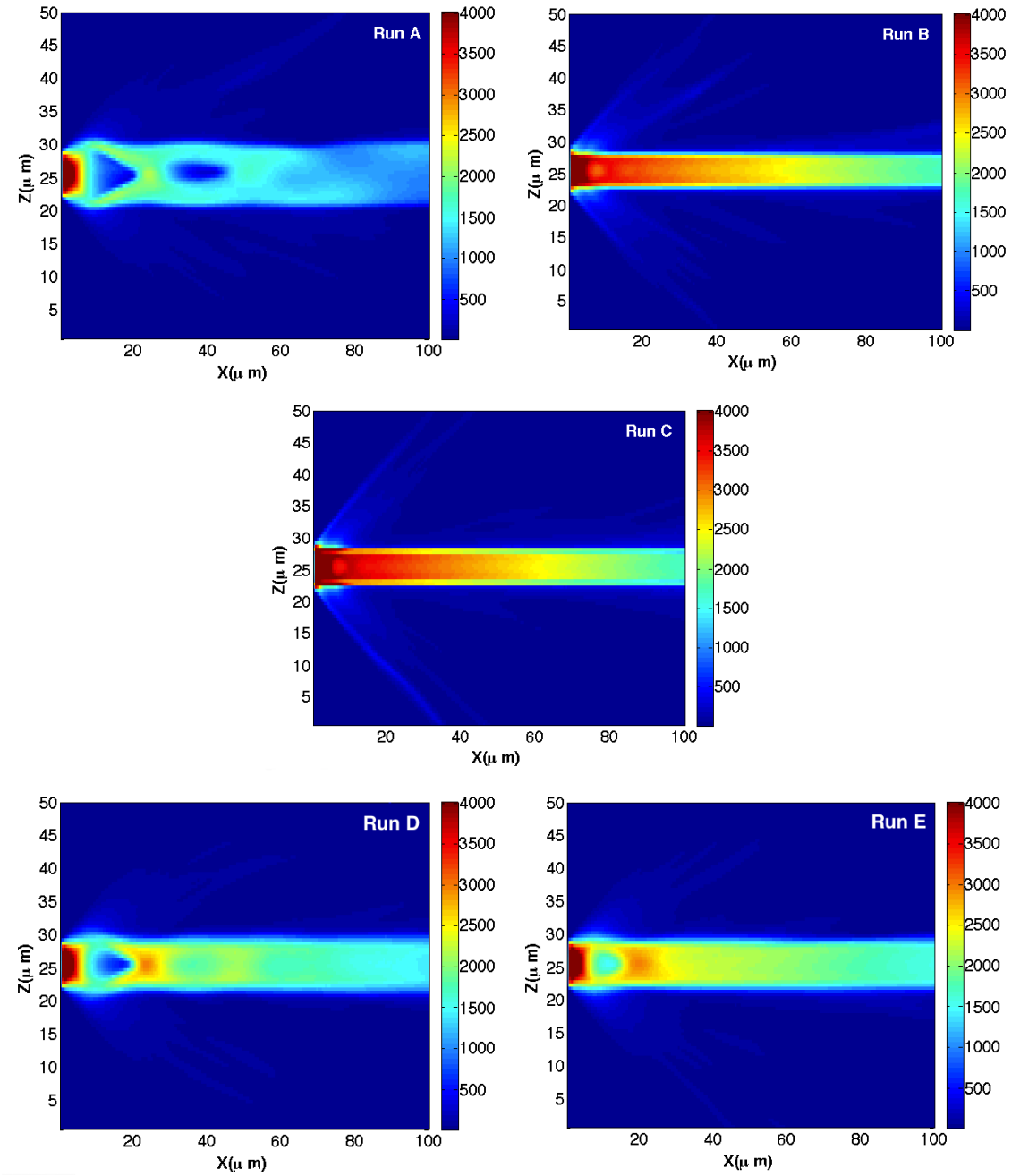

Figure 5.9: x-z Slices taken of the background temperature in (eV) in the y midplane at 2.2 ps for Runs A-E. The design of each run and Target Z profile is shown in Figure 5.3 and summarised in Table 5.1.

current. The CH substrate is heated but to temperature lower than the wire. This heating is due to some radial expansion of the fast electrons and does not result from radiation transport which is not included in ZEPHYROS. There is a gradient in temperature with depth along the guide which is observed in all runs. However, this

gradient differs in each run due to the difference in the generated azimuthal magnetic field discussed previously. Annular heating is observed in Run A at $x = 20$ μm and $x = 40$ μm which is in line with the position of the generated interior magnetic fields as shown previously in Figure 5.5. This corrupts the uniformity of heating along the depth of the wire. More uniform heating with the depth is obtained in Run B due to the small radius of the guide. The result of Run B is already noticed in [74]. However, the heating in Run B is comparable to that in Run C although the latter has twice the wire diameter the of Run B. This result identifies an important solution to solve the problem of the laser pointing stability. A large guide diameter can be heated uniformly just as for a small guide diameter if its interface with the CH substrate is graded in Z and if χ is less than 1. This is discussed later in the end of this section.

The images of Runs D and E show the temperature profile in the case of using multilayered wire scheme. High temperature ≈ 5 keV is observed at the electron beam injection site in both images. This is on the left hand side of the figure. Then the temperature suddenly drops at $x \approx 15$ μm before rising again ≈ 3 keV at $x \approx 25$ μm followed by a gradually dropping along the depth of the guide. The drop in temperature at $x = 15$ μm is due to the growth of the interior magnetic fields at this position, which excludes the fast electrons. However, this drop is larger in Run D than in Run E due to the stronger interior magnetic fields in Run D. The difference between the two runs is due to the graded interface in Run E. Heating in Run D is more uniform than in Run A even though $B_\phi L_\phi$ is lower in D than in A. As the core of Run D is small, this maintains a higher fast electron current density which increases the heating rate. To understand this, it is helpful to look at j_f^2 in both runs. Figure 5.10 shows line-outs of j_f^2 at $y = z = 25$ μm at the end of the laser pulse 2 ps in Runs A and D along x-direction at $10 \leq x \leq 100$ μm. The reason for taking j_f^2 is that the rate of heating scales as $\partial T_b/\partial t \propto \mathbf{j}_f^2$ as stated in (2.32). Generally, the fast electron density in Run D is higher than in Run A. In both runs, there is

a decrease in the fast electron density between $10 \leq x \leq 15$ μm before rising again at $x \approx 17$ μm and reaching the maximum at $x \approx 25$ μm and decreasing again after $x \approx 30$ μm. After this, fluctuations in the fast electron density are observed which is likely due to the drag and scattering of the fast electrons. The observations of the fast electron density in Figure 5.10 are in line with the background temperature images.

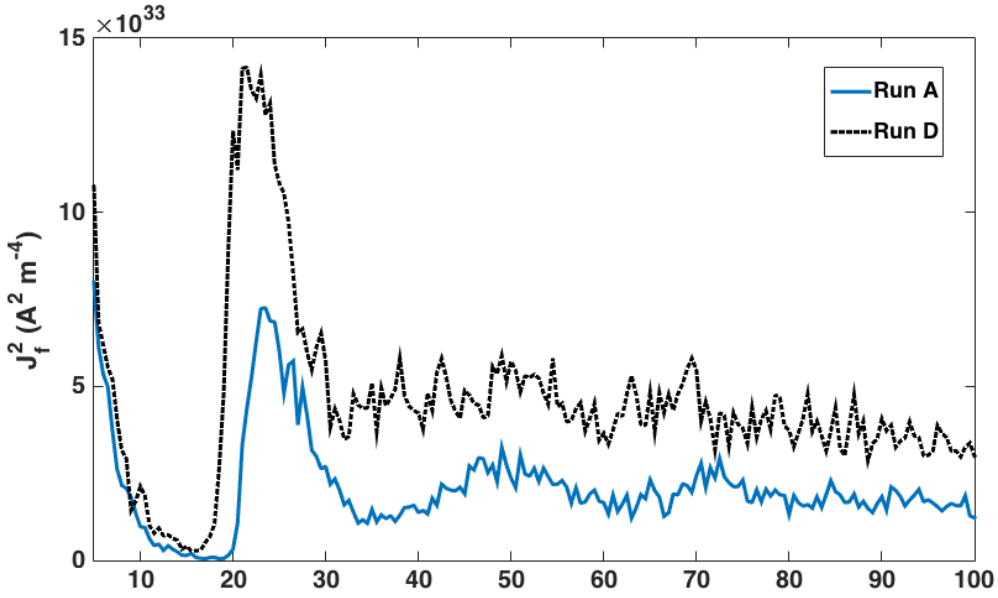

Figure 5.10: Plots of the square fast electron current density in A^2m^{-4} at $y = z = 25$ μm along x-direction at the end of the laser pulse 2 ps in Runs A and D at $10 \leq x \leq 100$ μm.

To view the data of the background temperature images in more detail for Runs B-E, line-outs of the background temperature is taken at $y = z = 25$ μm along x-direction between $10 \leq x \leq 100$ μm at 2.2 ps and shown in Figure 5.11. Generally, all targets have temperatures in the keV range which is high compared to the temperature ranges that observed in [74, 75]. The reason for this is that the reduced Wilks' ponderomotive scaling (2.13) is used in all these targets while a standard Wilks' ponderomotive scaling used in work of [74, 75]. When the reduced Wilks' ponderomotive scaling is used, the fast electron kinetic energy is reduced by 0.6.

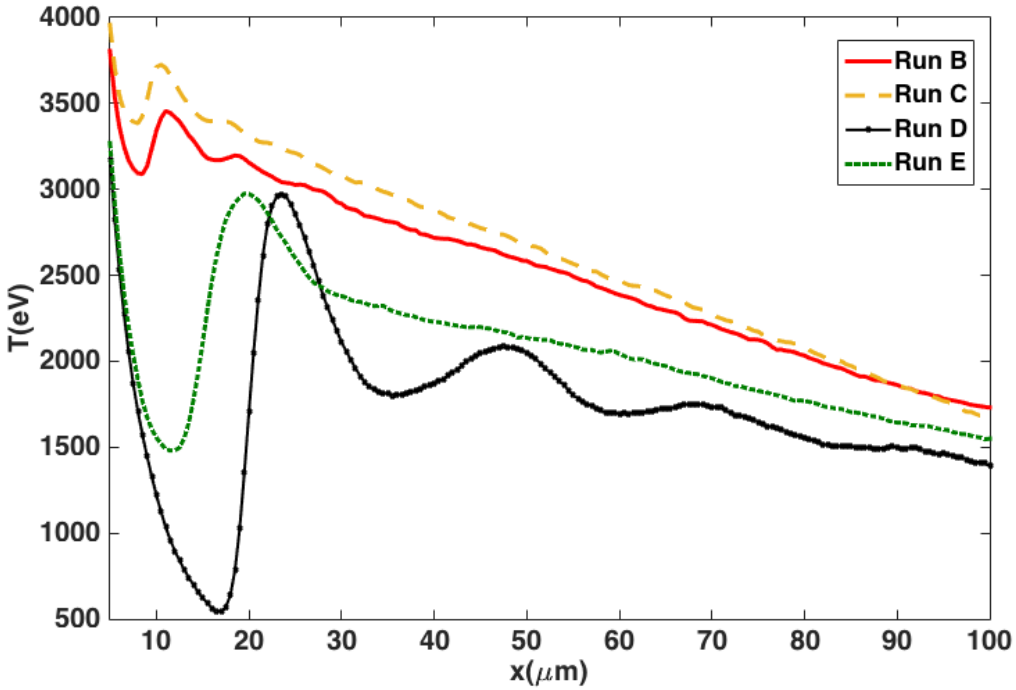

Figure 5.11: Plots of background temperature in eV in Runs B - E at $y = z = 25$ μm at 2.2 ps in each case along x-direction at $10 \leq x \leq 100$ μm.

This reduction increases the fast electron density since,

$$\mathbf{j}_f = \frac{e\beta I_L}{\bar{\epsilon_f}} \tag{5.9}$$

and consequently, this increases the rate of heating as stated in (2.32). In Figure 5.11, it can be seen that Runs B (red solid line) and C (orange dashed line) are heated to similar temperatures. There is oscillation in their temperature between $10 \leq x \leq 15$ μm due to inhomogeneity of the fast electron propagation near the injection region. After this, a gradual reduction in the temperature occurs. The slight difference in temperature between Runs B and C is due to the fact that that $r_{wire} > r_{spot}$ in Run C while $r_{wire} < r_{spot}$ in Run B. Note that Run C provides more tolerance to the pointing laser inaccuracy. Significant drop in temperature is observed in the multilayered-Z scheme (Runs D and E) between $10 \leq x \leq 20$ μm. After $x = 20$ μm, the variation in temperature in Run D (green dotted line) is larger than in Run E (black circle-solid line). More uniform heating is obtained in Run E

where the interface is graded in Z.

On the other hand, the result of Run C is insensitive to the centring accuracy of the beam. It is essential that $r_{wire} > r_{spot}$ and the χ is less than 1 in the design of Run C. To test the insensitivity of the centring accuracy of the beam in Run C, χ is chosen to be 0.44. Figures 5.12 (a) and (b) show two different examples where the laser does not hit the centre of the wire in the design of Run C. In Figure 5.12 (a), the laser centring point is outside the r_{core} but still inside the r_{wire} while in Figure 5.12 (b) the laser hits the upper edge of the r_{core}. The resulting heating from the both examples are still uniform with the depth even with this non-centring. More uniform heating is obtained when the laser hits close to the centre of the wire. As the magnetic field is located on the inner edge of the wire due to the grading the interface, the fast electron beam is uniformly confined in the core. The grading at the interface with χ is less than 1 ensures the fast electrons with diverging trajectory are redirected towards the higher resistivity regions. The conclusion is the design of the Run C gives smoother heating compared to all other runs.

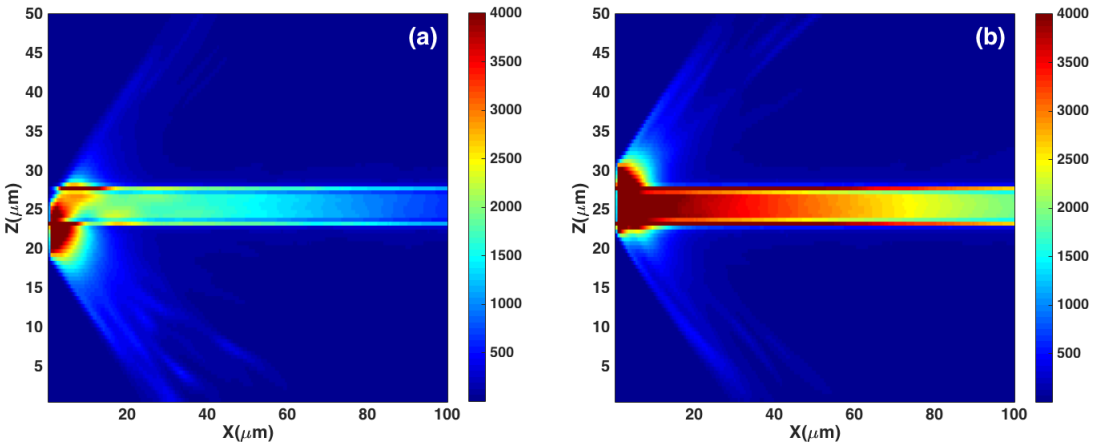

Figure 5.12: x-z slices taken of the background temperature in (eV) in the y midplane at 2.2 ps for two examples of the design of Run C. In (a) the laser centring point is outside the r_{core} but still in the r_{wire} area while the laser hits the upper edge of the r_{core} in (b).

5.3.2.3 Kinetic energy of the fast electrons and their Larmor radius inside the wire

The maximum kinetic energy of the fast electrons confined inside the wire is of interest. This is estimated at the end of the laser pulse by calculating the fast electron momentum using the confinement condition (5.3) for fast electrons with angle of 90° to x-axis as,

$$eB_{\phi}L_{\phi} \approx P_f \tag{5.10}$$

where e is the electronic charge and P_f is the fast electron momentum. This approximation gives the maximum fast electron momentum inside the wire. The Lorentz factor γ is calculated in the form,

$$\gamma = \sqrt{\left(\frac{P_f}{m_e c}\right)^2 + 1} \tag{5.11}$$

where m_e is the electron mass and c is the speed of light to enable an estimate of the kinetic energy of the fast electrons ϵ_f as,

$$\epsilon_f = 0.511(\gamma - 1) \quad \text{MeV} \tag{5.12}$$

Run	B_{ϕ} (T)	L_{ϕ} (μm)	ϵ_f (keV)	r_g (μm)
A	3500	0.99	640	1
B	3600	1	680	1
C	4600	0.96	900	1
D	2200	1.3	480	1.5
E	1700	2.2	720	2

Table 5.2: Maximum kinetic energy ϵ_f and largest Larmor radius of the fast electrons, at 2 ps, inside the wire in Runs A -E

Table 5.2 shows the maximum kinetic energy ϵ_f and the largest Larmor radius r_g of the confined fast electrons inside the wire at 2 ps for Runs A-E along with the values of B_{ϕ} and L_{ϕ}. The energy of the confined fast electrons in Run C (graded

interface) is the highest and reaches ≈ 900 keV. This is inline with the highest temperatures are observed in Run C. Also, the slight difference in temperature between Runs B and C is reflected in the difference between ϵ_f. Runs A and B show a comparable fast electron energy. This is expected since both B_ϕ and L_ϕ are comparable. However, Run B is heated more uniformly than Run A due to the smaller radius of the wire. This is in line with the results in Figure 5.8. Run E has slightly higher ϵ_f than Run D due to the grading the interface in Run E.

The largest Larmor radius is estimated as shown in Table 5.2. Generally, the Larmor radius in the guide with multilayered-Z is larger than in guide with pure-Z. For Runs A-C, this radius r_g is nearly equal to L_ϕ whilst slightly larger in Run D and smaller in Run E. According to the confinement condition (5.3), the fast electrons will be confined if,

$$L_\phi \geq r_g \tag{5.13}$$

5.4 Discussion of the results

The main findings of this chapter concern the effect of grading the atomic number at a boundary between the guide element and the solid substrate. The reason for doing this is to improve the uniformity of heating whilst designing a target with a larger radius of the guide account for laser pointing instabilities. Grading the atomic number at the interface of a resistive guide is beneficial for two reasons; firstly, it helps to collimate the fast electrons uniformly to the core of the larger radius of the guide. This produces heating similar to that in a smaller guide radius. A larger guide radius with grade interface configuration is more tolerant to pointing stability of the laser. Secondly, it increases the product $B_\phi L_\phi$ at an early time of the interaction, which helps to confine more fast electrons into the guide. The condition for best performance of the graded interface configuration is that the ratio between the core of the wire that has not been graded to the laser spot radius must be less than 1.

The study of the grade interface configuration is performed in two schemes of the guide; standard pure-Z and multilayered Z wires. The results of this work can be summarised as follows.

1. For the azimuthal magnetic field

   The configuration reduces the interior magnetic fields that form within the guide close to the axis. This implies more uniform propagation of the fast electrons and consequently improves the heating. In addition, it increases the magnetic flux density B_ϕ in the pure-Z guide by 24% while increasing the width L_ϕ in the multilayered-Z guide by 50% at the end of the laser pulse. A more uniform magnetic field profile is also obtained with a graded interface in the multilayered-Z guide. Furthermore, the graded interface configuration increases azimuthal magnetic field growth rate in both schemes. The fastest and highest azimuthal magnetic field growth rate is obtained when the pure-Z wire has a graded interface in Z. In this case, the typical values of the product $B_\phi L_\phi$ are obtained at the first 200 fs of the interaction. This increases the guide heating as more fast electrons are confined at early time of interaction.

2. For the guide heating

   An increase in the uniformity of heating is obtained in both schemes when their interface with the solid substrate is graded in Z. The graded interface configuration reduces the annular heating strongly in the pure-Z guide scheme while reduce it to some extent in the multilayered-Z guide scheme. Comparable heating is obtained in a large radius, pure-Z guide with graded interface compared to a small radius, pure-Z guide with sharp interface. In addition, improvement in heating is observed in a multilayered-Z guide with graded interface compared to the same scheme with sharp interface due to increasing homogeneity in fast electron density.

3. For fast electron kinetic energy and its Larmor radius

Higher energetic fast electrons are confined in pure-Z and multilayered-Z guides with graded interface. The Larmor radius is of the order of L_ϕ in both schemes.

5.5 Summary

This chapter considers the effect of grading the atomic number Z between the guide and the solid substrate and studies numerically the effect of this configuration on standard and multilayered resistive guide schemes. Out of the designs introduced in this chapter, the pure-Z guide with grade interface is the most promising for three reasons. Firstly, it is more tolerance to pointing process . Secondly, this design gives the highest $B_\phi L_\phi$ compared to all of the other designs. Thirdly, it provides a way to control the uniform propagation of the fast electrons when using larger wires.

Chapter 6

Modelling the Rayleigh-Taylor instability driven by radiatively cooling dense plasma

6.1 Motivation

Lancaster *et al.* [67] included the Rayleigh-Taylor (RT) instability to explain the expansion behaviour of a thick layered target and to reproduce temperatures that were in agreement with other published temperature data [19, 101]. The emergence of the RT instability in their work was unexpected and was inferred from simulation. The findings of Lancaster *et al.* [67] led Rossall *et al.* [4] to design an experiment to directly observe linear regime of the RT growth at the interface of a fast-electron-heated solid density target. In this experiment, a CH-Cu target with a machined sinusoidal interface was X-ray radiographed face-on to measure the growth in the sinusoidal features with time. This chapter investigates the experiment of Rossall *et al.* [4] by performing numerical simulations. The key aim of this investigation is to obtain a better understanding of the physics of the experiment and explore how RT instability may be studied at very high energy density. Four main physics aspects

are involved in this experiment: fast-electron-heating of the solid target, radiative cooling, radiation transport and hydrodynamic RT instability. The physics of each these phenomena are investigated.

The chapter begins with a description of the Rossall *et al.* [4] experiment, including the experimental concept and results (Section 6.2). Then the simulation work is divided into four sections as follows. Section 6.3.1 explores the RT target heating by fast electrons using the ZEPHYROS code. Section 6.3.2 estimates the radiative cooling of each layer in the RT target. Section 6.3.3 focuses on the influence of the radiation transport (in particular the opacity) on the hydrodynamics. Section 6.3.4.1 investigates the RT growth and compares numerical results with the experimental ones. The radiation hydro-codes HELIOS and HYADES are used in these investigations to examine the effect of using theoretical opacity models that based on DCA and screened hydrogenic models respectively on the acceleration of the Cu-CH interface. This acceleration is driven by a pressure difference between the materials. This pressure difference derives from the radiation cooling in the two materials. Finally, the results of the chapter are discussed (Section 6.4) and a summary of the chapter is given in Section 6.5.

6.2 The Rossall *et al.* experiment

6.2.1 Experimental set-up

The Rossall et al. [4] experiment was performed at Target Area West (TAW) using the VULCAN laser [134]. This laser is an Nd:glass laser which operates at a wavelength of 1.053 μm and consists of 8 beam-lines. Figure 6.1 shows a schematic of the experiment. A bi-layered Rayleigh-Taylor target was irradiated by a short-pulse chirped pulse amplification (CPA) beam-line. This beam was focused into a spot of diameter 10 μm with a 3 ps pulse duration containing 300 J of energy. This gives a peak intensity of up to $\approx 10^{20}$ Wcm^{-2}. As shown, the CPA beam was focused on

the RT target in a direction whereby both materials could be heated simultaneously. The RT target dimension was $200 \times 27 \times 200$ μm and consisted of 25 μm and 2 μm thick CH and Cu layers receptively as shown in Figure 6.2. A sinusoidal (ripple) was machined at the interface between the two layers. This has a wavelength of 30 μm and amplitude of 300 nm. The errors associated with the thicknesses of the Cu and CH layers of the target were found to be 10% and 5% respectively, while those associated with the amplitude of the sinusoidal were 0.5 nm for the Cu and a few nm for the CH. The total number of target shots during the experiment was 50.

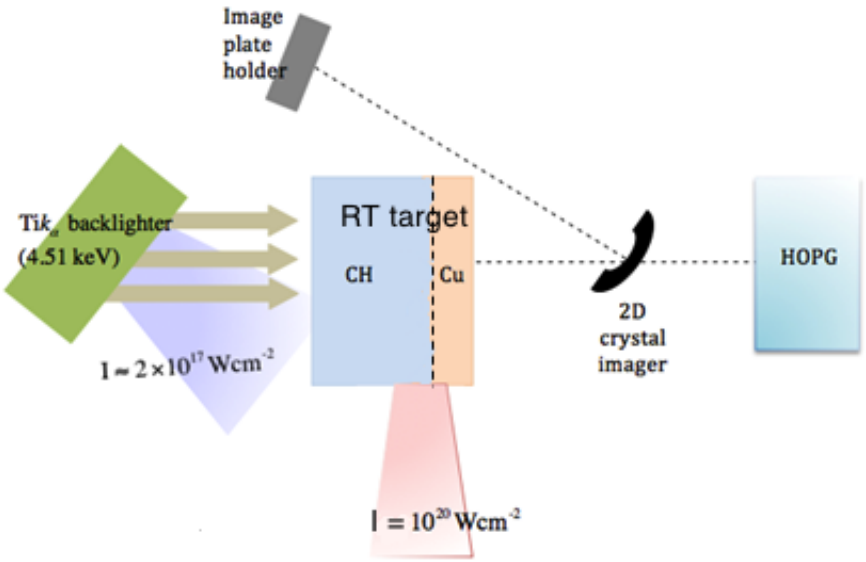

Figure 6.1: Diagram of the Rossall *et al.* [4] experimental set-up (top view).

Two diagnostics were used to study the RT target. The primary diagnostic measured perturbation growth using X-ray backlighter probing. In this diagnostic, a backlighter Ti target was irradiated by a second beam with 2 ps of pulse duration containing 100 J of energy. This beam was focused into a spot of diameter 200 μm using a f/3 parabolic mirror, yielding an intensity of up to $\approx 2 \times 10^{17}$ Wcm^{-2}. The Ti backlighter target thickness was 25 μm. The radiation from the Ti backlighter passed through the RT target at different time delays to measure the change in transmission, from which the amplitude of the sinusoidal can be inferred. The images

of the target were made using a 2D spherical quartz crystal with a radius of 38 cm placed after the RT target and recorded on image plate. The delay time between the RT heating pulse and the backlighter pulse was varied starting from 50 ps and ranging up to 200 ps. The reason for starting at 50 ps was to ensure that radiative cooling in the RT target was established. The second diagnostic measured the Cu K-shell emission spectrum using a HOPG (Highly Ordered Pyrolutic Graphite) spectrometer. This spectrometer was placed out of the RT target plane at angle of 24° facing the Cu layer of the RT target. Then the time-averaged K_α and He-like spectrum was recorded on image plates during the experiment and used to estimate the Cu temperature and density.

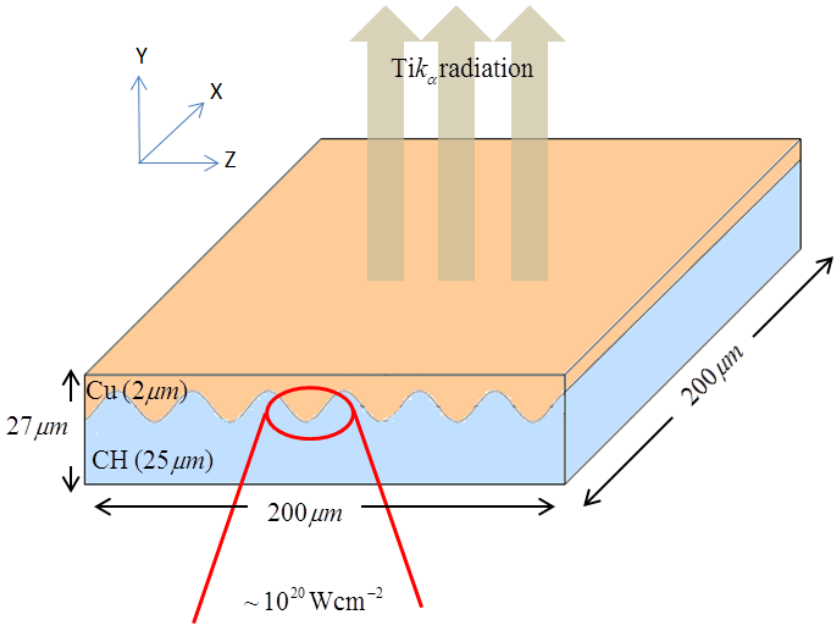

Figure 6.2: Diagram of the RT target design, showing the directions of the laser heating pulse and radiograph radiation.

6.2.2 Rayleigh-Taylor experimental concept

Figure 6.3 shows the stages of RT evolution. The target becomes RT unstable when the density gradient and pressure gradient across the CH-Cu interface are anti-

parallel. The initial density gradient is fixed by the choice of target material. The target is isochorically heated by the fast electrons, with the assumption that both the Cu and the CH are uniformly heated. The pressure gradient ($\nabla P = k_B n \nabla T$) is driven by radiative cooling. The simplistic view is that the intermediate-Z Cu radiatively cools more rapidly than the low-Z CH. As a result, the pressure in the Cu drops more quickly than in the CH, establishing RT unstable conditions with $\nabla\rho \bullet \nabla P < 0$ across the material interface. Material flow results from the differing pressures. However, the situation is more complex. The details of radiative cooling depend upon the temperature and density of the Cu and CH. It is the rich physics associated with radiative cooling that forms a large part of this chapter. It is worth mentioning that this experiment designed only to investigate the RT instability in the linear regime.

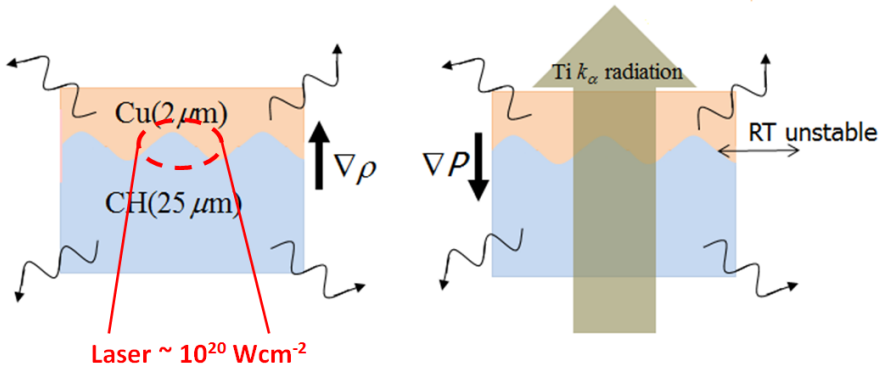

Figure 6.3: Diagram of the RT experimental concept.

6.2.3 Experimental results

The methodology of analysing the experimental data is described extensively by Rossall [5]. A brief discussion of the experimental results is given in this section.

The sinusoidal growth in the RT target is measured using monochromatic X-ray radiography. The change in transmission of a Ti K_α source is measured from peak to trough. The spatial variation of the transmitted radiation, which is dominated by the Cu, gives a measure of the growth of the sinusoidal features. The measurements

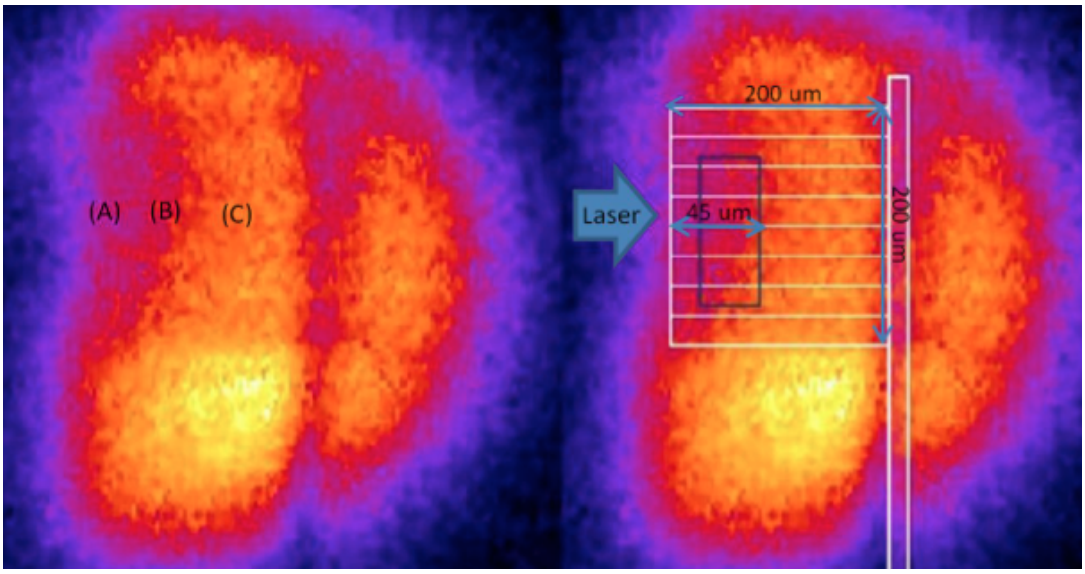

Figure 6.4: Sample of radiographic image of the experiment from the 2D spherical crystal imager at 150 ps. The left image shows the Ti K_α source passing through the RT target. The backlighter does not pass through portion A while it does pass through portions B and C. However, it was difficult to see any perturbations in portion C. Therefore, the RT data is picked up from portion B. The right image shows the laser incidence direction, the RT target dimensions and the integration area (blue box). The distance from the edge of the target to the end of the blue box is ≈ 45 μm.

are converted to line-densities using Beer's law (3.27). From these the growth of the sinusoidal amplitude is inferred. However, this analysis was challenging since poor contrast between the peaks and troughs was obtained in the backlighter images. Figure 6.4 shows an example of the image of the backlighter passing through the RT target at 150 ps. The left image in the Figure 6.4 shows the Ti K_α source passing through the RT target while the right image in the Figure 6.4 shows the same image with a schematic of the target position and dimension, the laser incidence direction and the area where the RT data is picked up by integration (blue box). As a result, the backlighter signal over the selected section of the image, the blue box in Figure 6.4, was integrated along the direction of the perturbations to enhance the contrast of any perturbations which were present. This integration was parallel to the perturbations. Clearly from the left image, the backlighter does not pass into portion A and it is difficult to see any perturbations in portion C. Therefore, the

RT data was picked up from the portion B. The distance from the edge of the target to the end of the blue box is around ≈ 45 μm. We will see later in Section 6.3.1 that the poor contrast in portion C is due to strong fast electron filaments growing parallel to the sinusoidal perturbation direction and the area where the RT data is integrated is the region of the target that is heated uniformly.

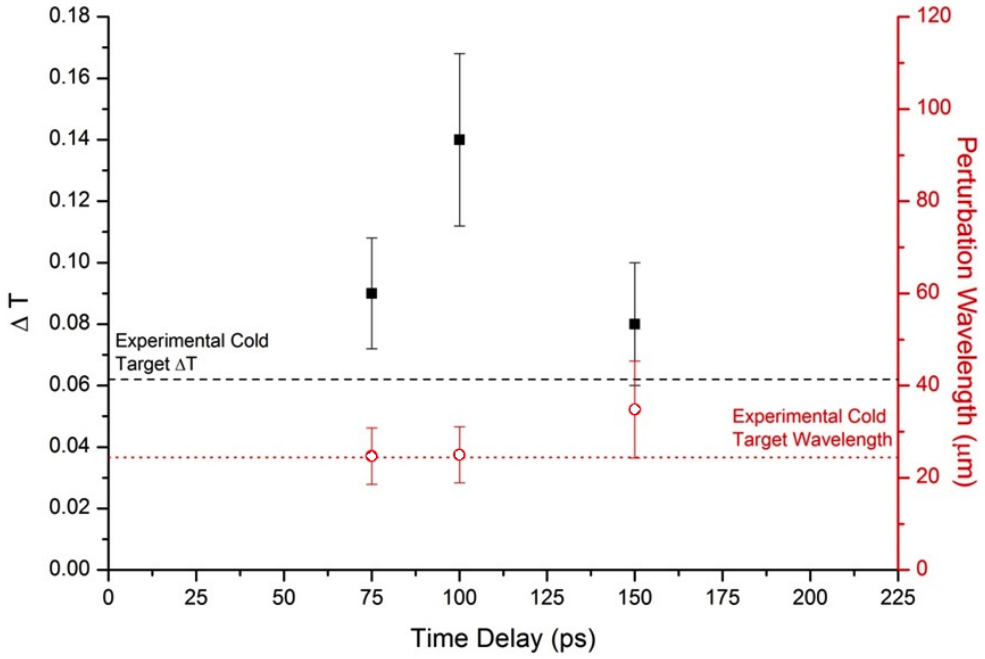

Figure 6.5: The experimental change in transmission ΔT from peak to trough (solid point, left axis) along with the associated perturbation wavelength in μm (hollow point, right axis). The dashed line shows the experimental change in transmission for the cold RT target. The dotted line shows the experimental perturbation wavelength for the cold RT target. This data was analysed by Rossall [5].

The change in the transmission ΔT and the associated perturbation wavelength values resulting from this integration are shown in Figure 6.5. The change in the transmission ΔT is plotted on the left axis (solid points) while the associated perturbation wavelength is plotted on the right axis (hollow points) of Figure 6.5. The black dashed line shows the experimental recorded change in transmission in a cold RT target which is 0.062 ± 0.007. This is from a target that was not shot. In addition, the red dotted line shows the perturbation wavelength of the cold target which is 24.5 ± 6.1 μm. The measurement of ΔT was performed for fast electron heated

RT targets at time delays between 50 ps and 200 ps. However, as explained above, the poor contrast of the images affected the ability to identify the peaks and troughs of the perturbations. This is especially so at the time delays of 50 ps and 200 ps. This was not the case at 75 ps, 100 ps and 150 ps where the increases in ΔT and the associated fundamental wavelength 30 μm were readily identified. At these time delays, the increases in ΔT were observed, which indicates to the increase in the amplitude of the sinusoidal perturbation. At 150 ps time delay, the measurement showed that ΔT was less than it was at 100 ps and the error bar of the associated wavelength was large compared to 75 ps and 100 ps.

Figure 6.6 shows the experimental peak-to-trough amplitude growth in nm. The increase in peak-to-trough amplitude was measured and found to be 480 ± 150 nm and the time integrated growth rate was found to be 10 ± 2 ns^{-1} at a time delay of 100 ps.

The Cu plasma conditions were deduced from the time-averaged record of Cu spectra using the HOPG sperctrometer. It was found that the peak temperature of the Cu was 350 ± 50 eV and the the electron density was $n_e = 10^{22} - 10^{23}$ cm^{-3}.

6.3 The simulation

The RT instability growth in the Rossall *et al.* [4] experiment differs from the classical RT phenomenon (see Chapter 3) in four ways. Firstly, the target thickness is finite, which means that the growth of the RT will be limited to a short time scale by target expansion. Secondly, the target exhibits quick expansion, dropping the density at the interface. Thirdly, the target is heated by the fast electrons, which means that the fast electron transport processes affect target heating. Fourthly, there is strong radiative cooling in both materials of the target, which influences the target pressure. These factors lead to a complex picture. Modelling is therefore needed to understand this experiment. The numerical studies in this chapter are divided into four main sections as follows:

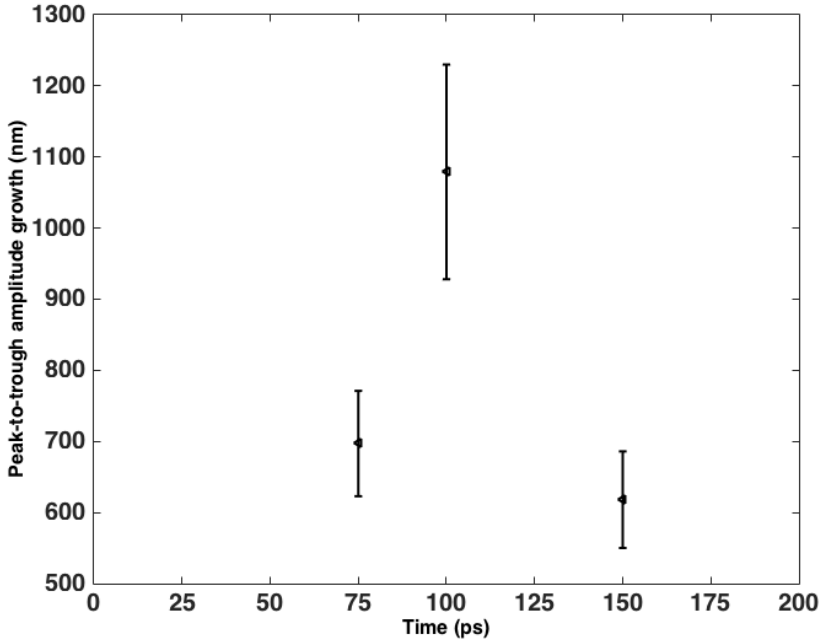

Figure 6.6: The experimental growth in the sinusoidal amplitude. This data was analysed by Rossell [5].

1- Investigation of the RT target heating As explained in Section 6.2.1, the target was shot from one side whereby both the CH and the Cu could be heated simultaneously. This heating is explored via the ZEPHYROS code and the temperature of each material is estimated.

2- Estimating the radiative cooling As stated in Section 6.2.2, the pressure gradient was driven by the radiative cooling. This occurs after isochoric target heating. This radiative cooling is estimated in both hydrodynamic codes; HYADES and HELIOS.

3- Investigation of the radiation transport The influence of radiation transport is investigated in both HYADES and HELIOS. Since each hydro-code uses a different opacity model as explained in Section 3.3, the theoretical TOPS opacity [111] is used for comparison purposes.

4- Investigation of hydrodynamic RT instability The two hydrodynamic codes HYADES and HELIOS are used to model the time dependent interface Atwood number, density, length scale and acceleration. These are used as inputs in to 1D

dimensional RT growth rate formula and RT growth amplitude model.

6.3.1 Investigation of the RT target heating

The background temperatures of the Cu and CH layers were modelled using ZEPHYROS and as a function of the half-divergence angle in a copy of the experimental RT target but without the sinusoidal interface. The cell size of the grid was 1 μm in each direction with 130 macroparticles injected into each cell. This helps to reduce the statistical noise. It was assumed that 30% of the laser energy coupled to the fast electrons. The laser intensity, spot size and pulse duration parameters were identical to those of the experiment. The fast electron temperature was set to 2.7 MeV (see Section 2.2). Three divergence angles of 50°, 60° and 70° were used in the simulations, since these were the expected angles produced for intensities up to 10^{20} Wcm^{-2} [22, 23, 135, 136]. Figure 6.7(a) shows the Z atomic number of the cold RT target at 3 μm depth in the x-direction. The thickness of each layer is shown in the y-direction. The top layer is 2 μm of Cu. Figure 6.7(b) shows the background temperature at 3 μm depth in the x-direction, notice the compressed side in the z-direction. It also shows the heated region where the laser strikes the RT target. It is essential that the laser heats both layers.

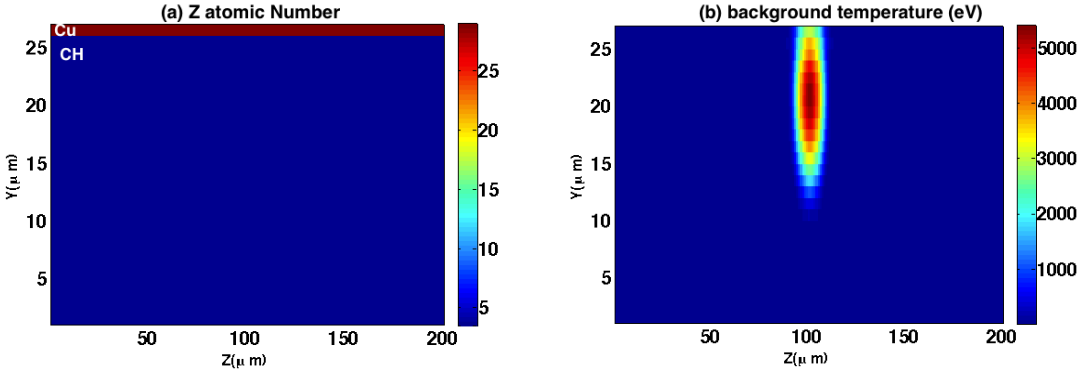

Figure 6.7: (a) Slice taken for target Z-profile at 3 μm depth in x-direction (see Figure 6.2), showing the thickness of each layer in y-direction. (b) Slice taken for target background temperature in eV at 3 μm depth in x-direction at 3.5 ps(see Figure 6.2), showing the simulated laser spot position.

Figure 6.8 shows x-z contour plots of the resulting background temperatures of

the Cu and CH for three divergence angles respectively at 3.5 ps. These slices were taken for each material at the interface where the simulated laser hit. Generally, the simulations showed electron filaments growing along the x-direction. The presence of the filamentary structures inside the RT target implies non-uniform heating. This is likely the reason why no clear perturbations were seen in portion C of the experimental measurement in Figure 6.4. These filaments grow parallel to the sinusoidal perturbation direction. These simulations are in agreement with the observation of filaments in other experiments with similar target dimensions [65]. The presence of filaments leads to complex temperature structures and this will have an impact on the target hydrodynamics. In addition, the RT target heating in the x-direction is also adversely affected by both electric field inhibition and angular dispersion as discussed in Chapter 4.

Figures 6.8 (a) and (b) illustrate the different filaments structure in the Cu and CH layers. This difference between the two materials is related to the resistivity, for example in the Spitzer regime, $T_e > 100$ eV gives relation $Z \propto \eta$ and $\eta \propto T^{-3/2}$. The heating rate is resistivity dependent (2.32), with resistive heating of Cu slower than plastic. According to this, the background temperature in the case of Cu (Z=29) is lower than that of CH (Z=3.5). Therefore, as stated in Section 2.3.6, when the background temperature is low, a small number of large filaments grow, while in the case of a high background temperature, a large number of small-scale filaments are observed [39,137]. This agrees with the filamentary structure observations in Figure 6.8 for Cu and CH.

In addition, the filament structures within the same material differ according to the divergence angles. This is also shown Figure 6.8. Fewer filaments were obtained with a smaller divergence angle. This is related to transverse fast electron temperature $T_{f,\perp}$ [138]. A larger divergence angle causes a reduction in $T_{f,\perp}$, since the number of the fast electron current density $\mathbf{j}_f$ reduces. This affects the modulation in the transverse self-generated magnetic field and how the Lorentz force acts to

bend the oppositing beams.

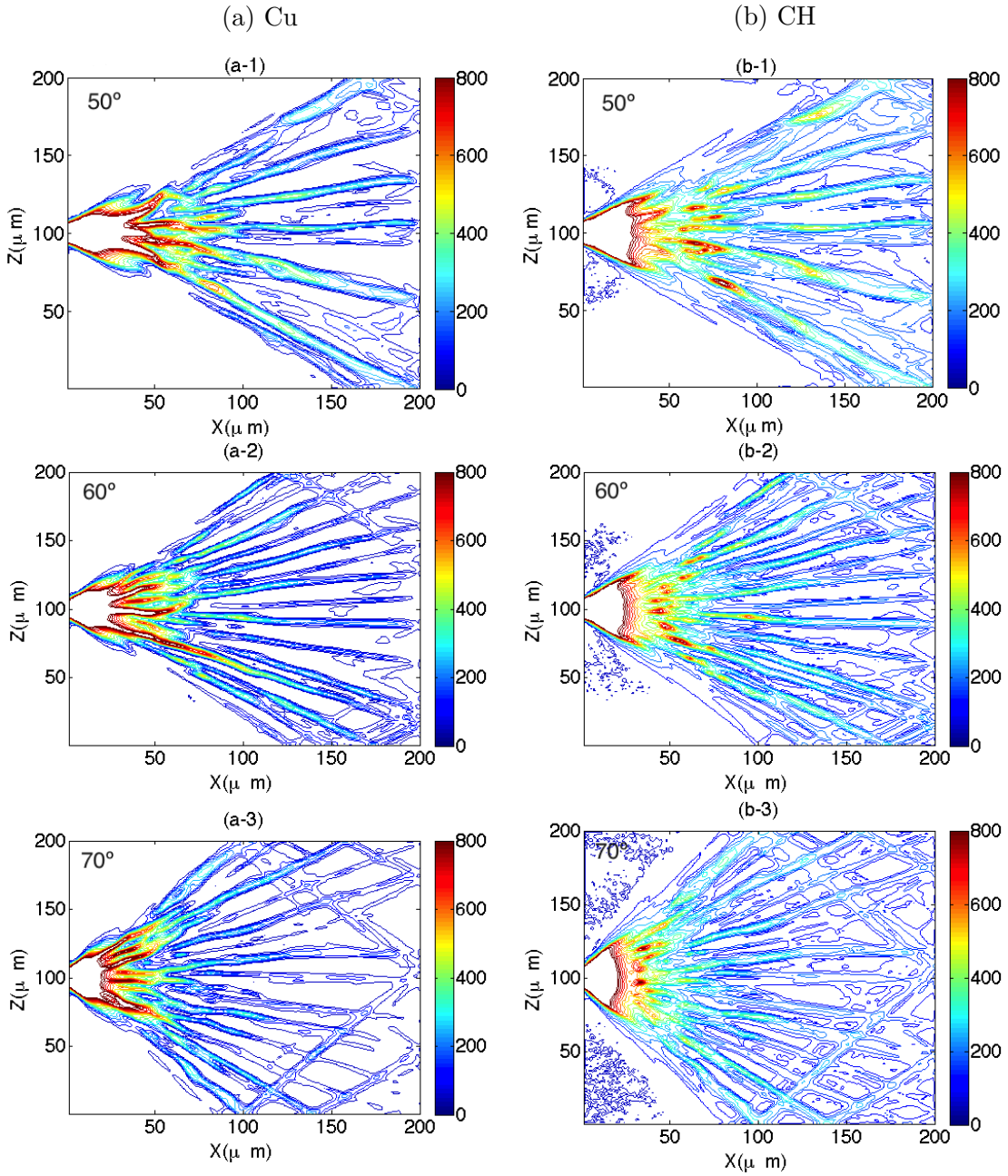

Figure 6.8: Contour slices taken of RT target background electron temperatures in eV at the interface between the Cu and CH layers. Figures (a-1), (a-2) and (a-3) for Cu at 50°, 60° and 70° respectively. Figures (b-1), (b-2) and (b-3) for CH at 50°, 60° and 70° respectively.

Furthermore, the filament temperatures in the same material varied at specific divergence angle. For example, the filament temperatures in the case of Cu at 50° ranged from 200 eV to a peak of 700 eV. This variation in temperature makes

defining a background temperature a challenge. An attempt was made to estimate an overall mass average background temperature of each material individually. The mass of each layer in the RT target was calculated and was found to be 7.14×10^{-7} g for Cu and 1.1×10^{-6} g for CH. The overall background temperature of each material was estimated at $x = 50$ μm. This is the region where the RT data is measurement was made from experimental images. In this region, the simulated RT target temperature is relatively uniform. Figure 6.9(a) shows an example of the temperature distribution and it is varied between 350 eV and 700 eV. The area under these temperature spikes gives the overall background electron temperature. The mean of the background temperature and variance were estimated from this. This process of estimating the background temperature was repeated for each material at different divergence angles and the results are shown in Figure 6.9(b) as a function of the half-divergence angle. It is seen that the background temperature decreases with increasing divergence angle. This is due to the transverse spreading of the fast electrons. The background temperatures at 50° and 60° are similar and are in agreement with the experimental determined temperature of 350 ± 50 eV. The simulation also predicts that the Cu and CH will heat to similar temperatures.

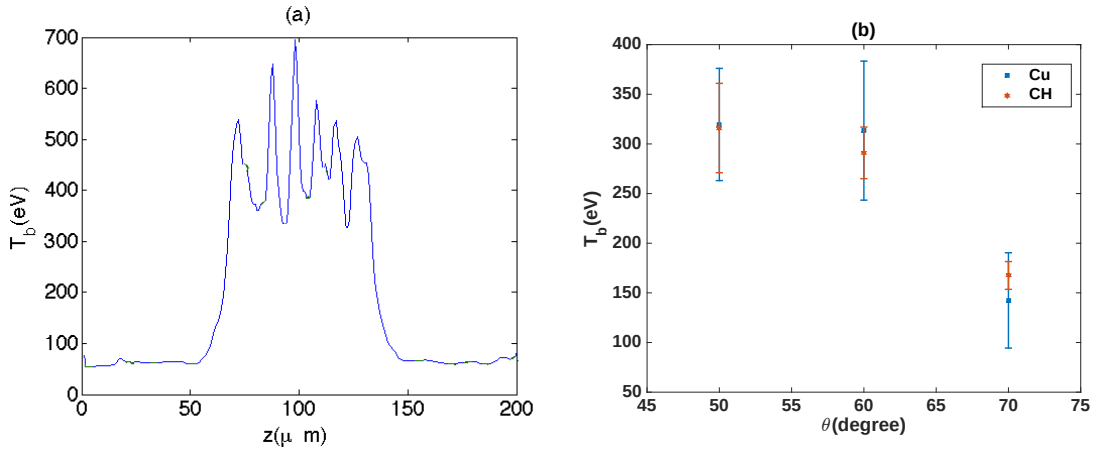

Figure 6.9: (a) Shows an example of estimating the target temperature of CH layer at $x = 50$ μm. The mass average temperature calculated over the material thickness then the mean of the background temperature and its variance were estimated in the area under temperature spikes (b) Shows the resulting background temperature of each material as a function of the half-divergence angle at a depth of 50 μm.

Finally, fast electron refluxing [28] was observed in the simulated RT target. This refluxing is expected since the thickness of the target in the y-direction is restricted to 27 μm. However, the fast electron refluxing does not significantly affect the heating of the RT target.

6.3.2 Radiative cooling

The specific radiative cooling rate Q_{Emis} is a strong function of the temperature, since $Q_{Emis} \propto T^4$ as stated in Section 3.2.2, and it is usually calculated in hydrodynamic codes with multi-group opacities and radiative transfer [118]. At high temperatures, the average excitation and ionisation is high. These contribute to the emission of radiation and the total opacity, which in turn leads to the radiative cooling. Since the radiative cooling is sensitive to radiation emission processes and opacity as shown in (3.31), appropriate accounting for the details of the atomic physics is essential. The estimation of radiative cooling is performed using both HYADES and HELIOS to explore the sensitivities of the two different models. (HELIOS) employs a large amount of detailed atomic data based on the DCA model while HYADES uses in-line calculations based on the screened hydrogenic atomic model. To calculate the radiative cooling, targets of composition and thickness as used in the experiment were modelled under the approximation of LTE and hydrodynamic motion of the plasma turned off.

Figure 6.10(a) shows the radiative cooling rate of the Cu and CH at solid density as a function of temperature; this was obtained from HYADES. From left to right, the radiative cooling of the CH is higher than that of the Cu until 250 eV. Beyond this temperature, the cooling rate of the Cu exceeds that of the CH. This would cause CH to cool faster than Cu in the simulation as CH will radiate more strongly than the Cu at lower temperatures in HYADES. This affects the material flow as the CH pressure gradient might not be sufficient to push the Cu. This has implications for the perturbed amplitude growth predicted from HYADES as shown later in

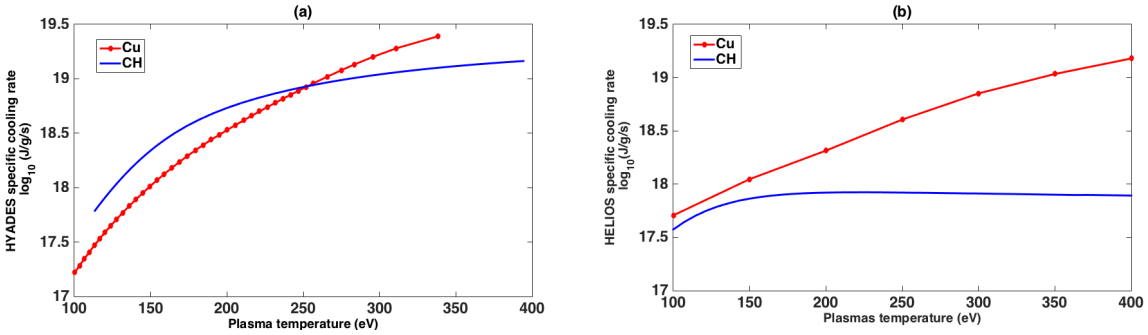

Figure 6.10: (a) Shows log_{10} radiative cooling for solid density of Cu and CH in HYADES, considering LTE and no hydro-motion. Lower than 250 eV the CH starts to cool faster than the Cu in HYADES. (b) Shows log_{10} radiative cooling for solid density of Cu and CH in HELIOS, considering LTE and no hydro-motion. The Cu radiates faster than the CH even at low temperatures in HELIOS.

Section 6.3.4.6. In comparison in HELIOS, Figure 6.10(b) shows the Cu radiative cooling rate is greater than that of the CH including lower temperatures. The two calculations are of the same magnitude the differences, however, particular below 250 eV, are very important.

To explain the reason for this difference in radiative cooling between the two codes, the average ionisation Z^* of the solid density of the Cu and the CH as a function of temperature is shown in Figures 6.11(a) and (b) respectively. Generally, the average ionisation increases with temperature. Figure 6.11(a) shows the average ionisation of Cu solid density. As shown, at the peak experimental temperature of 350 ± 50 eV, Z^* is in the range of Ar-like Cu to Ca-like Cu, i.e. ionised to L-shell. Here, the ions with an incomplete outer shell include a large number of decaying excited states and line transitions which contribute to the energy loss via radiation. These transitions also contribute to the opacity and thus affect the radiative cooling [118]. It is therefore important to use detailed atomic physics models in order to include many possible transitions between the different levels of excitation across many ionisation effects. This is not the case with CH, however, where Figure 6.11(b) shows the average ionisation of solid density CH between 300 and 400 eV is full ionisation $Z^* \approx 3.4$, K-shell.

It is worth mentioning that the plasma also cools by target expansion into the

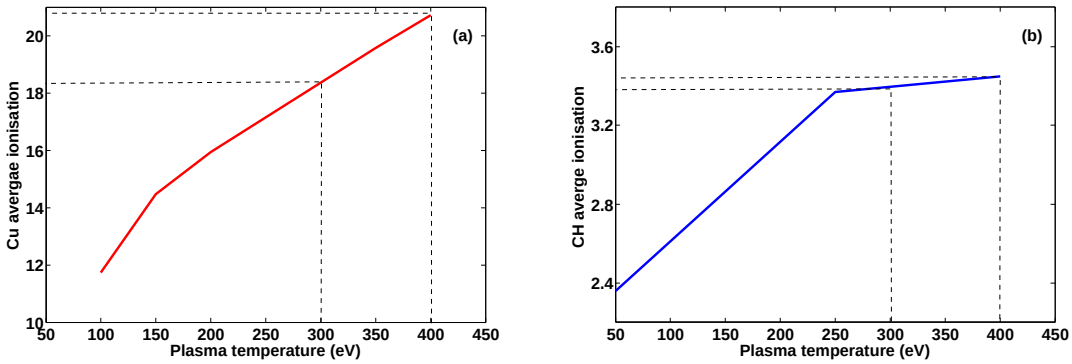

Figure 6.11: (a) Average ionisation Z^* of Cu solid density as a function of temperature. The dashed lines show the experimental temperature range 350 ± 50 eV. (b) Average ionisation Z^* of CH solid density as a function of temperature. The dashed lines show the experimental temperature range 350 ± 50 eV. The CH is fully ionised at these temperatures.

vacuum and thermal conduction. Both effects can be modelled and how these effect RT growth are discussed in Sections 6.3.4.3 and 6.3.4.5 respectively.

6.3.3 Investigation of the radiation transport

As stated in Section 3.2, plasma hydrodynamics can be influenced by aspects of radiation transport, such as the accuracy of the opacity calculation, the details of the atomic data (which are essential in order to estimate the absorption and emission of the photons), and the type of radiative approximation method that is used to perform the radiation calculations. The multi-group radiation model was used here to calculate the radiation transport. This model is computationally efficient and maintains accuracy by grouping opacity variations across the range of frequency domain is of interest. The model was employed using 50 energy groups, with up to 10 keV maximum photon energy.

The RT target consisted of Cu and CH, each of which behave differently with regard to radiation transport. Since CH plasma is a low-Z material, it tends to be optically thin at high temperatures [108]. The difficulty comes with a 2 μm thickness of Cu, since it has an intermediate atomic number (Z=29) and the Cu can vary between optically thick and optically thin across the frequency range. It is assumed

that the simulated RT target is optically thin and the Planckian mean opacity is used here for two reasons. Firstly, since there is no source of energy gain in the simulated target, it is assumed that the radiation can escape the target. This ignores the small fraction of photons of the order of $y_L/\lambda_{<\nu>}$ which are absorbed [6], where y_L is the plasma thickness and $\lambda_{<\nu>}$ is the mean free path of photons. Secondly, the emission opacities are Planckian mean opacities and the radiative cooling depends on emission opacities as defined in (3.31) [118]. In addition, it is assumed that the plasma is in LTE. The assumption of LTE with Planckian mean opacity is valid here since the mean free path of photons is greater than the Cu layer thickness [139].

In the preceding section, it has stated that the difference in the predicted radiative cooling between HYADES and HELIOS is due to the difference in the atomic model used to calculate opacity. Intermediate Z-materials such as Cu need detailed atomic data, including the atomic structure of different ions and the energy levels of ground and excited states and line transitions. HYADES opacity is based on the screened hydrogenic model whereas HELIOS opacity is computed by calculating the contributions of the bound-bound, bound-free and free-free processes using the DCA model. Details of each model were given in Section 3.2.1.

	TOPS		HELIOS		HYADES	
Cu density	$\kappa_{<\nu>p}$	$\lambda_{<\nu>}$	$\kappa_{<\nu>p}$	$\lambda_{<\nu>}$	$\kappa_{<\nu>p}$	$\lambda_{<\nu>}$
(gcm^{-3})	($\mathrm{cm}^2\mathrm{g}^{-1}$)	(μm)	($\mathrm{cm}^2\mathrm{g}^{-1}$)	(μm)	($\mathrm{cm}^2\mathrm{g}^{-1}$)	(μm)
8.93	2200	0.5	1690	0.7	7800	0.1
0.893	990	10	400	30	2600	4
0.0893	400	260	50	2290	2300	44

Table 6.1: Table of Cu emission opacities $\kappa_{<\nu>p}$ in $\mathrm{cm}^2\mathrm{g}^{-1}$ and photon mean free path $\lambda_{<\nu>}$ in μm at 400 eV and different densities.

To show the impact of opacity on radiative cooling, the frequency averaged Planckian mean opacities were calculated for each code using (3.29) at 400 eV for the different densities of the Cu and CH. These were then compared to TOPS opacities at the same temperature and densities. The frequency range is between

$\approx 1\times10^{16}$ Hz to 2×10^{18} Hz which corresponds to the range of the photon energy used in the calculations, i.e. $0.01-10$ KeV. The integration of (3.29) was performed using the trapezoidal integration method. A short IDL program was written to read the extracted HYADES opacity. Table 6.1 shows the emission opacity of Cu for the three codes. Generally, there is a difference between all three codes, which is due to the different in atomic models involved. Some agreement, however, was found between TOPS which uses DTA atomic model and HELIOS which uses DCA atomic model. This is due to the fact that both codes use detailed atomic systems. The difference between them becomes clear at $1/100^{\text{th}}$ solid density. At this density, TOPS opacity is higher than HELIOS by factor 8. Moreover, HYADES opacity $\kappa_{<\nu>p}$ is high compared to both HELIOS and TOPS at all densities. From Table 6.1, the screened hydrogenic atomic model overestimates opacities. This overestimation results from the hydrogenic degeneracy of atomic levels while the splitting of the energy levels with different angular momentum was neglected.

In addition, Table 6.1 shows the mean free path of emitted photons, estimated using (3.28). HYADES has a shorter mean free path $\lambda_{<\nu>}$ than both HELIOS and TOPS, and this difference increases as the Cu density is reduced. This implies that in a HYADES simulation Cu will radiate more effectively and cool more quickly. Again, both the HELIOS and TOPS mean free paths agree except at the lowest density. It is important to note that the mean free path is greater than the size of the Cu layer, i.e. 2 μm, excepted at solid density. The fact that the mean free path at solid density is shorter than the size of the Cu layer can be ignored since the target expands dropping the density quickly.

Table 6.2 shows the emission opacity of CH for the three codes. There is an agreement in the generated opacity from the three codes. This emphasises the fact that in these conditions CH does not need a complex atomic model.

An attempt was made to match the Cu-HYADES radiative cooling with that of Cu-HELIOS, since the HELIOS opacities are in some agreement with TOPS

	TOPS		HELIOS		HYADES	
CH density	$\kappa_{<\nu>p}$	$\lambda_{<\nu>}$	$\kappa_{<\nu>p}$	$\lambda_{<\nu>}$	$\kappa_{<\nu>p}$	$\lambda_{<\nu>}$
(gcm^{-3})	(cm^2g^{-1})	(μm)	(cm^2g^{-1})	(μm)	(cm^2g^{-1})	(μm)
1.1	71	130	70	130	70	120
0.11	8	10700	8.5	10600	8	12100
0.011	0.90	100×10^4	0.8	110×10^4	0.7	140×10^4

Table 6.2: Table of CH emission opacities $\kappa_{<\nu>p}$ in cm^2g^{-1} and photon mean free path $\lambda_{<\nu>}$ in μm at 400 eV and different densities.

opacities as shown in Table 6.1. The ratio between both opacities at each density of the Cu and the CH was estimated, as shown in Table 6.3, this was to enable the use of an opacity multiplier in HYADES. The ratio for CH at different densities is nearly 1, but this is not the case for the Cu, where the ratio needs to be different at each different density. Figure 6.12 shows an example of the Cu radiative cooling at solid density after the using opacity ratio at solid density of 0.22. The cooling rate using the scaled opacity by the multiplier (red circle-solid line) is compared to standard HYADES (green dashed line) and HELIOS (blue solid line). Again, hydrodynamic motion was turned off in these calculations and the cooling rate calculation started at 400 eV. It was found that Cu in standard HYADES cools faster than that in corrected HYADES. In standard HYADES, the temperature drops from 400 eV to 338 eV at time of 1 ps while it drops to 366 eV in the same time period when the 0.22 opacity multiplier is used. However, even with this correction the cooling rate curve does not match that of HELIOS. The opacity multipliers required to match radiative cooling in HELIOS for Cu and CH solid density are greater requiring 0.1 and 0.033 respectively. These values make the HYADES opacity low compared to other opacity values, which is not physically correct. The effect of using an opacity multiplier in HYADES for RT growth is investigated in Section 6.3.4.6.

Cu density (gcm^{-3})	Ratio	CH density (gcm^{-3})	Ratio
8.93	0.22	1.11	1
0.893	0.15	0.11	1.1
0.0893	0.021	0.011	1.14

Table 6.3: The opacity ratios between HELIOS and HYADES for Cu and CH based on values of Tables 6.1 and 6.2 respectively for the different densities.

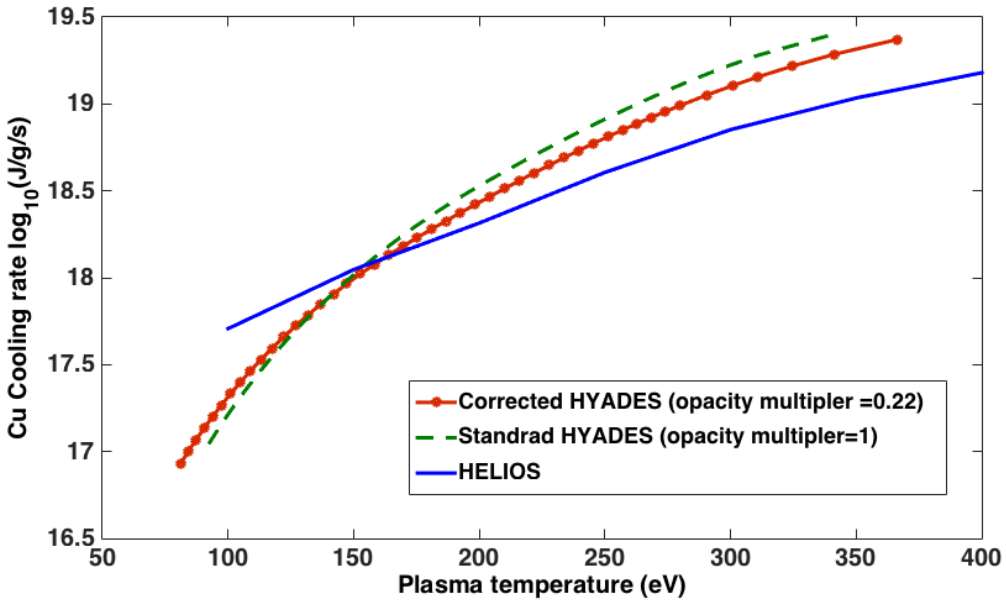

Figure 6.12: Shows the difference in radiative cooling log_{10} for fixed solid density of Cu between standard HYADES (opacity multiplier=1), corrected HYADES (opacity multiplier = 0.22) and HELIOS.

6.3.4 Investigation of hydrodynamic RT instability

6.3.4.1 The hydrodynamic modelling

The approach to hydrodynamic modelling is to set a single uniform temperature for the target, i.e. the same temperature for both layers. The assumption is that the target is instantaneously and isochorically heated by the fast electrons. A similar approach was used by Lancaster *et al.* [67]. The radiation hydrodynamic model simulates the radiative processes and target hydrodynamics over time. The hydrocodes are given the conditions that represent the situation at the end of the short-pulse laser duration including a temperature of 350 eV.

6.3.4.2 Simulation initialisation

The simulations were carried out with a total of 100 zones, 30 for Cu and 70 for CH, in planar geometry. This choice of zone numbers means that the zone sizes were small, which was sufficient resolution to track the changes in the parameters at the material interface. Each material was defined in a separate region with thicknesses of 2 μm of Cu and 25 μm of CH and densities of 8.9 gcm^{-3} and 1.11 gcm^{-3} for the Cu and CH respectively. In HYADES, the Cu layer was feathered into the CH-Cu interface with a ratio of 1.15 in order to obtain high spatial resolution. Open boundary conditions were implemented to allow for plasma expansion. A multigroup diffusion radiative transport model was used with radiation divided into 50 energy groups, with up to 10 keV maximum photon energy. The effect of using a higher number of groups was tested, with a range of 30 to 60 and 100, and it was found that increasing the number of groups in HYADES beyond 40 had no significant impact on the radiation calculations, while in HELIOS, it was computationally expensive using more groups than 50 as the DCA model was used. In addition, LTE ionisation model was employed in both codes.

The tabulated SESAME equation of state [140] was used in HYADES while the tabulated PROPACEOS equation of state was used in HELIOS. The opacity in HYADES is based on hydrogenic model, while the PROPACEOS opacity is used in HELIOS which is based on the DCA model. The time step was chosen with the consideration that it should yield accurate results for post-processing hydrodynamic data with sufficient resolution to enable capture changes in amplitude and growth rate. Trial simulations were carried out with a range of time steps, and as a result the time interval for successive post-processing of the hydrodynamic data was chosen to be 5 ps.

6.3.4.3 RT target expansion dynamic

The temporal evolution of RT target expansion is shown in Figure 6.13. The expansion of the Cu in HELIOS is more rapid than in HYADES. It seems that the compression wave is much stronger in HYADES than in HELIOS. This results in a decrease in density in HELIOS compared to HYADES, leading to higher Atwood number in HYADES than in HELIOS as discussed in the next section.

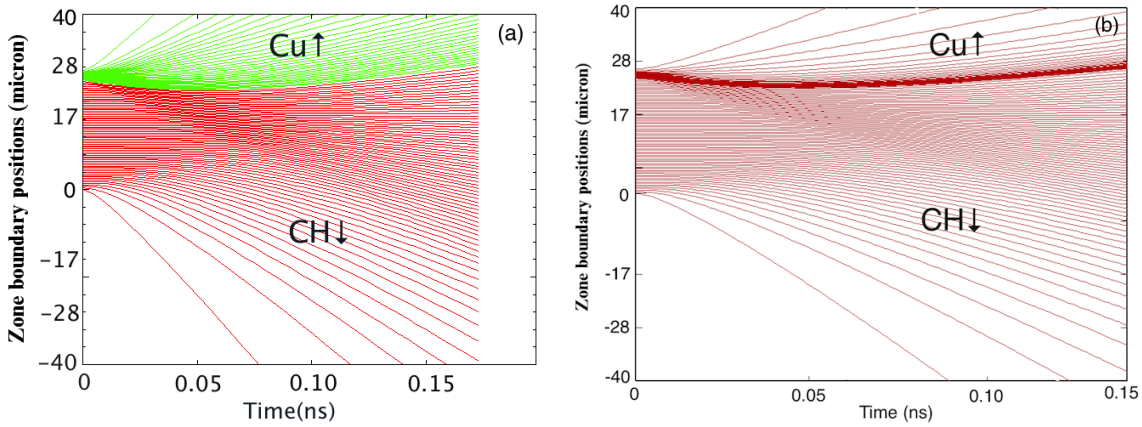

Figure 6.13: (a) Temporal evolution of the RT expansion in HELIOS. The green lines represent the Cu layer expansion and the red lines the CH layer expansion. The arrows indicate the direction of the expansion. (b) Temporal evolution of the RT expansion in HYADES. The Cu layer is located above the 25 μm zone boundary position while the CH layer lies below 25 μm. The arrows indicate the direction of the expansion.

The experimental results predict that the RT growth occurs within the first 150 ps. This is supported by simulation. Initial Cu is at higher density and pressure ensuring a stable interface. This is clear in both Figure 6.13 and Figure 6.14(a). The latter figure shows the simulated pressure (left axis, blue dot-dashed curve) and simulated density (right axis, green solid curve) versus distance at 10 ps. The black dashed lines at 0 and 27 μm show the initial target position while the red dashed line at 25 μm indicates the interface position between the CH and the Cu. Figure 6.14(a) shows that the higher Cu pressure, which is 1×10^{14} Pa, compresses the lower pressure CH, which is 3×10^{13} Pa, and this leads to an increase in the local density of the CH to 1.5 gcm^{-3}. The interface is initially located at 25 μm (red

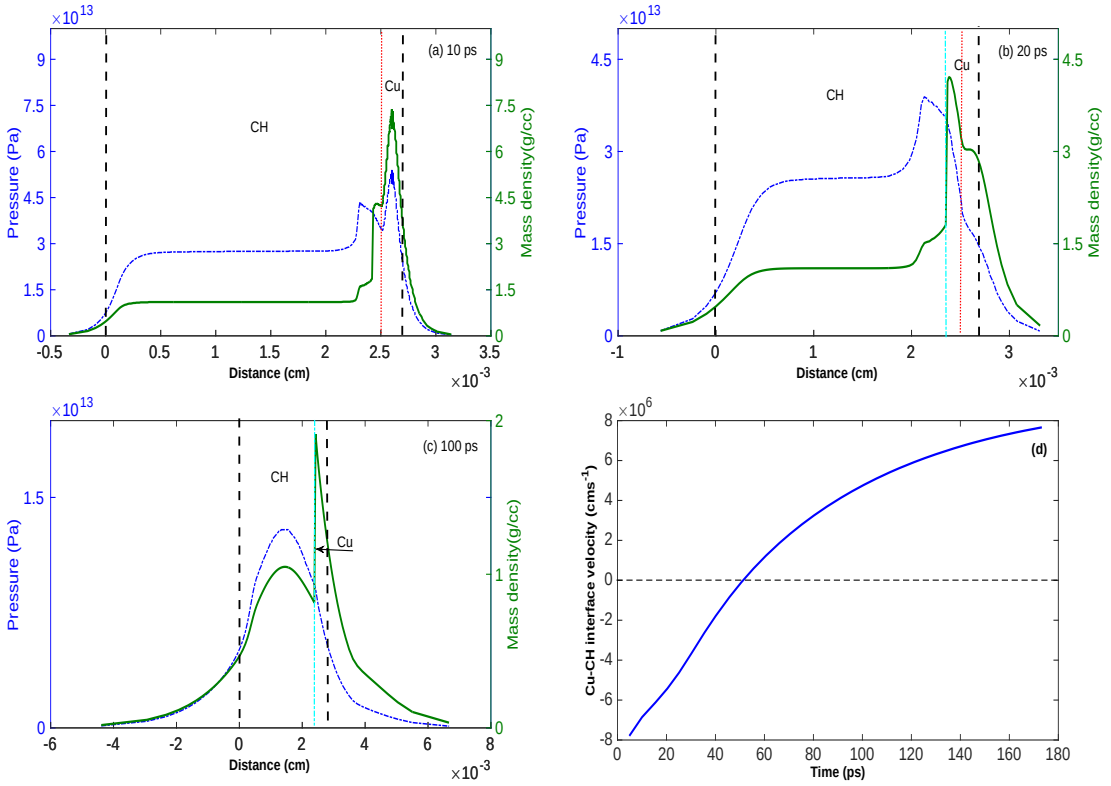

Figure 6.14: Simple pressure (left axis, dot-dashed curve) and density profile (right axis, solid curve) from HELIOS at (a) 10 ps, (b) 20 ps and (c) 100 ps. The red dashed line at distance of 25 μm indicates the initial position of the Cu-CH interface, the sky-blue dot-dashed line indicates the new location of the interface due to the Cu compression at the first 20 ps and the black dashed lines at 0 and 27 μm distance indicate the initial boundaries of the RT target before expansion. (d) shows the velocity of the Cu-CH interface with time in HELIOS.

dashed line), but this position changes due to the Cu compressing the CH. Thus the interface moves approximately -2 μm to the left as shown in Figure 6.14(b). The new location is shown in Figure 6.14(b) as sky-blue dot-dashed line. The simulation suggests that the RT configuration starts to emerge at 20 ps when the Cu pressure drops due to radiative cooling faster than the CH pressure, while the Cu density is still higher than the CH pressure, as shown in Figure 6.14(b). As the time progresses, the Cu pressure drops significantly compared to the CH pressure and the CH then

starts to accelerate the Cu. This is a RT unstable situation. Figure 6.14(c) shows an example of this at 100 ps. Figure 6.14(d) shows the velocity of the Cu-CH interface. During the first 55 ps the Cu accelerates the CH. This is the RT stable situation. The RT unstable situation occurs beyond 55 ps where the CH accelerates the Cu.

6.3.4.4 Post-processor for RT parameters

Both HYADES and HELIOS are used to calculate the time dependent Atwood number A_t, acceleration g , density scale length L and the finite thickness factor f. These are used as input to a 1-dimensional growth rate formula (3.26). With this information, it is possible to predict growth of a perturbation based on the time-dependent evolution. A 1D hydro-code has been used in elsewhere [85, 95] to investigate RT instability in a similar way.

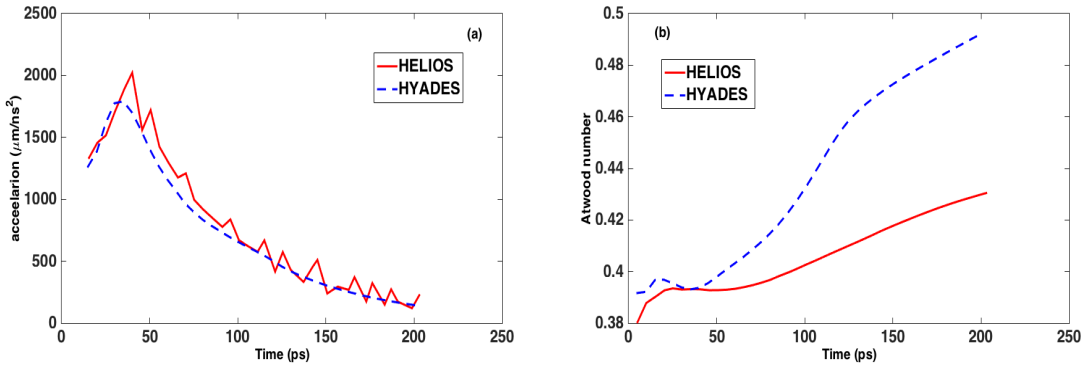

Figure 6.15: (a) Acceleration profile at the Cu-CH interface for both codes. (b) Atwood number at the Cu-CH interface for both codes.

Figure 6.15(a) shows the acceleration profiles of both HELIOS and HYADES. The acceleration values are higher than those usually obtained using a long-pulse laser system by approximately 2-3 orders of magnitude and will lead to high growth rates. The typical RT acceleration value produced by a long-pulse laser system is about 10 μmns^{-2} [34]. The maximum acceleration is at 30 ps in HYADES and at $\approx$ 40 ps in HELIOS then starts to drop due to the target expansion. In addition, Figure 6.15(b) shows a large difference in the predicted Atwood number due to the difference in the expansion dynamics as explained in the previous section. The

Atwood number in HELIOS is smaller than in HYADES.

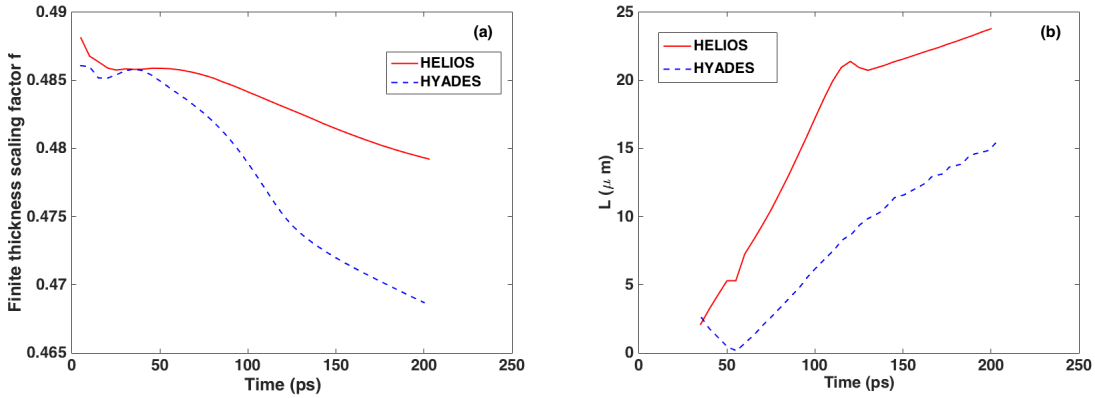

Figure 6.16: (a) shows the time-dependent finite thickness factor f in HELIOS (red solid line) and HYADES (blue dashed line). (b) shows the time-dependent density scale length L in HELIOS (red solid line) and HYADES (blue dashed line).

Figure 6.16 (a) the time-dependent finite thickness factor f. This factor in HELIOS does not change significantly and the same is true of the Atwood number in Figure 6.15(a). In HYADES, the change in this is larger but still small. The importance of including this factor into the RT growth formula (3.26) can be understood from (3.23). According to the denominator in (3.23), if the product of $kh \geq 2$, so $\coth(kh) \approx 1$, thus $f \approx 1$, which means f does not affect the growth rate. In our simulation of the experiment, the initial experimental wavenumber is $k \approx 0.21\ \mu\text{m}^{-1}$ and $\coth(kh_{CH})$ and $\coth(kh_{Cu})$ are approximately 1 and 2.5 respectively. The thickness of the CH is sufficient not to affect the RT growth, this is not the case for Cu and including f is important. Figure 6.16 (b) shows the time-dependent density scale length L. This scale increases significantly with time in HYADES in contrast to HELIOS. The differences in f and L is due to the difference in the expansion dynamics of the two codes.

6.3.4.5 The RT instability growth rate

The growth rate of the RT was calculated from both hydro-codes using (3.26), and the physics of different stabilisation effects on RT growth and the simulation parameters are discussed in Sections 3.1.2 and 6.3.4.2 respectively.

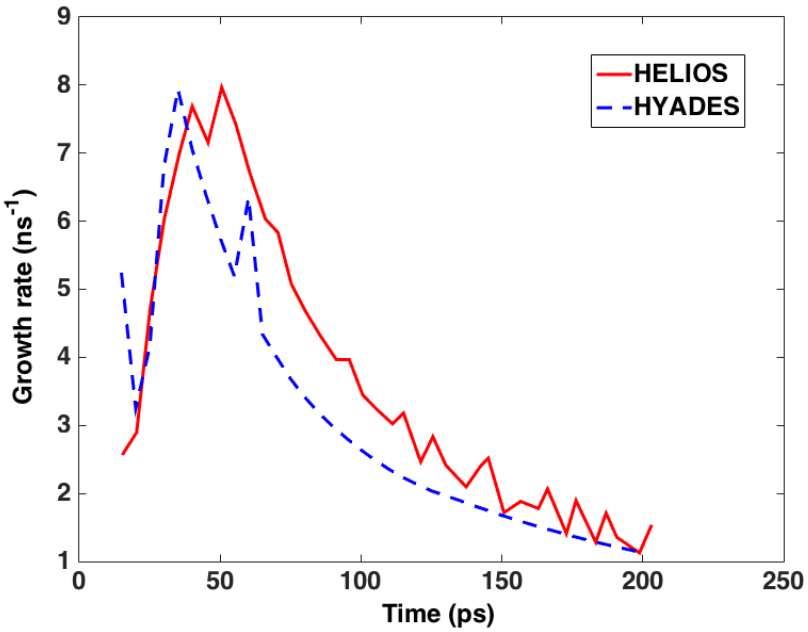

Figure 6.17: Growth rate in ns^{-1} using (3.26) for both HELIOS and HYADES.

Figure 6.17 shows the predicted RT growth rate from HELIOS (red solid line) and HYADES (blue dashed line). The RT growth starts at 20 ps. This growth continues and reach to the peak of ≈ 8 nm^{-1} at ≈ 30 ps in HYADES and at ≈ 45 ps in HELIOS. The growth continues as time progresses but the rate decreases due to the target expansion. This expansion reduces both the acceleration and the density at the interface. The predicted growth rate is lower in HYADES than in HELIOS. This is because the radiative cooling rate is overestimated in HYADES, as discussed in Section 6.3.2. The strong radiative cooling in HYADES makes the target cool quickly, leading to a reduction in pressure in the RT target, so the duration of the CH pushing into the Cu will be short. This is apparent in Figure 6.10(a), since at temperatures lower than 250 eV the cooling rate of the CH is faster than that of the Cu in HYADES.

Figure 6.18 shows calculations using data from HELIOS for classical RT growth formula $\gamma_{classical} = \sqrt{A_t kg}$ (dashed line) , $\gamma_L = \sqrt{A_t kg/(1+kL)}$ (circle-solid line) and (3.26) $\gamma_{LF} = \sqrt{A_t kg/(1+kL)f}$ (solid line), where f is given in (3.23). It is well-known that the classical RT formula overestimates the growth, since density-

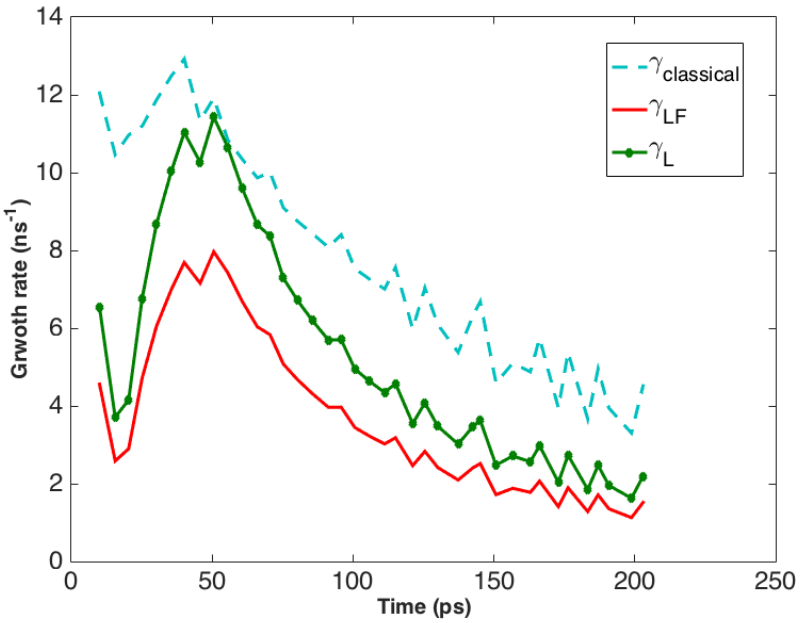

Figure 6.18: Comparison between the growth rate in HELIOS using the classical RT formula (dashed line), (3.26) without including the finite thickness factor f (circle-solid line) and (3.26) formula including f (solid line). This growth is in the unit of ns^{-1}

gradient stabilisation is not taken into account [6]. The influence of density-gradient stabilisation is seen in the green curve. This reduces the growth rate all times and results in a more rapid drop. An additional important effect is the finite target thickness factor f. This factor also stabilises the growth and its effect is seen in the red curve.

Another test was carried out to study the effect of the heat flow inside the plasmas on the RT growth rate. The simulated target was assumed to be heated uniformly and isochorically at $t_{hydro} = 0$, a gradient in temperature occurs once the target starts to expand. A simulation was performed by turning thermal conduction off, this showed that the RT growth rate increased by a factor of 10. This led to testing the validity of using the Spitzer and Harm model [34] and whether using a flux limiter would make a difference. The flux limiter imposes an upper limit on the conductivity. It was found that using a flux limiter does not affect RT growth. To interpret this result, a quantitative estimation of the ratio between the

electron-ion collision mean free path $\lambda_{ei} = (v_{th}/\nu_{ei})$ and temperature scale length $L_T = (T_e/|dT_e/dx|)$ was made for the Cu and the CH. $v_{th} = (k_B T_e/m_e)^{1/2}$ is the electron thermal velocity and ν_{ei} is the electron-ion collision rate defined in (2.20). The electron-ion collision rate ν_{ei} is of order of 10^{18} s^{-1} and 10^{17} s^{-1}, for the Cu and the CH respectively and with $\ln\Lambda = 5$. The thermal velocity v_{th} for both materials was in the order of 10^6 ms^{-1}. This implies that the electron-ion collision mean free path λ_{ei} is 10^{-12} m for Cu and 10^{-11} m for CH. The temperature scale-lengths for both materials are in the order of 10^{-5} m. Therefore, the ratio between the electron-ion collision mean-free-path λ_{ei} and temperature scale length L_T for the Cu and CH, respectively is,

$$\frac{\lambda_{ei}}{L_T} \approx 10^{-7} \tag{6.1}$$

$$\frac{\lambda_{ei}}{L_T} \approx 10^{-6} \tag{6.2}$$

and since $\lambda_{ei} << L_T$, the Spitzer and Harm model is valid here [34]. It is worth mentioning, that this analysis account for heat conduction perpendicular to a planar interface. The RT instability is 3D phenomenon and heat condition in the orthogonal directions is important. This is an important physics which need to be discussed when 2D or 3D hydrodynamic simulation is used to model this experiment.

6.3.4.6 The RT peak-to-trough amplitude growth

The perturbation amplitude is estimated using an analytical approach described in Wood-Vasey *et al.* [85]. This section begins by demonstrating this analytic method, followed by a comparison of the experimental results.

6.3.4.6.1 The analytical solution of embedded interface peak-to-trough amplitude growth

The linear growth of spatial amplitude perturbation is calculated using the analytic approach described in Wood-Vasey *et al.* [85]. This approach is based on solving the linearised equation governing perturbation growth as defined previously

in (3.2) as a function of growth rate using the backward differencing method of the Taylor series [141],

$$\zeta''(t) - \gamma_{RT}^2 \zeta(t) = 0 \tag{6.3}$$

where ζ is the spatial amplitude of the single-mode of the perturbation and γ_{RT} is the growth rate of RT (defined in (3.26)).

The Taylor backward differencing method is a standard method ensuring stability in solving ordinary differential equations (ODEs) [141]. Since (6.3) is a second-order ODE, two boundary conditions need to be specified to describe the physical situation being modelled. If the target is in static equilibrium, it can be assumed that there is no evolution in the spatial amplitude of perturbation ζ at time less than zero. Since the target is manufactured, the initial spatial amplitude can be measured $\zeta(t = 0)$. Thus the perturbation amplitude at $\zeta(t = 0)$ and $\zeta'(t = 0)$ can be specified as,

$$\zeta(t = 0) = \zeta(t < 0) = 600 \text{ nm} \tag{6.4}$$

$$\zeta'(t = 0) = \zeta'(t < 0) = 0 \text{ nm/ps} \tag{6.5}$$

where 600 nm is the initial amplitude of the sinusoidal from peak to trough as used in the experiment. Using the backward differencing method, the spatial amplitude at specific time t_n is,

$$\zeta(t_n) \approx \zeta(t_{n-1}) + \Delta t \zeta'(t_{n-1}) + \frac{\Delta t^2}{2} \zeta''(t_{n-1}) \tag{6.6}$$

$$\zeta(t_{n-1}) \approx \zeta(t_{n-2}) + \Delta t \zeta'(t_{n-2}) + \frac{\Delta t^2}{2} \zeta''(t_{n-2}) \tag{6.7}$$

$$\zeta(t_{n-2}) \approx \zeta(t_{n-1}) - \Delta t \zeta'(t_{n-1}) + \frac{\Delta t^2}{2} \zeta''(t_{n-1}) \tag{6.8}$$

where Δt is the time interval. In addition, the backward differencing method is

applied to equation (6.3) as,

$$\zeta''(t_{n-1}) = \gamma_{RT}^2 \zeta(t_{n-1}) \tag{6.9}$$

$$\zeta''(t_{n-2}) = \gamma_{RT}^2 \zeta(t_{n-2}) \tag{6.10}$$

Substituting (6.9) into (6.6) gives,

$$\zeta(t_n) \approx \zeta(t_{n-1}) + \Delta t \zeta'(t_{n-1}) + \frac{\Delta t^2}{2} \gamma_{RT}^2 \zeta(t_{n-1}) \tag{6.11}$$

Similarly, substituting (6.10) and (6.9) into (6.7) and (6.8), respectively, then combining those latter equations gives,

$$\zeta'(t_{n-1}) \approx \zeta'(t_{n-2}) + \frac{1}{2} \Delta t \gamma_{RT}^2 [\zeta(t_{n-1}) + \zeta(t_{n-2})] \tag{6.12}$$

Equations (6.11) and (6.12) are used to estimate the growth of the perturbed amplitude as a function of the growth rate γ_{RT}. This method is more accurate for estimating the growth than the simple growth calculation equation [142],

$$\zeta(t) = \zeta_0 e^{\gamma_{RT} t} \tag{6.13}$$

where ζ_0 is the initial amplitude. The reason is that this simple growth calculation is applied when the acceleration is constant or slowly varying with time [85]. The acceleration in laser-produced plasmas tends to change very quickly and in the current this case happens in a few picoseconds.

6.3.4.6.2 The RT peak-to-trough amplitude results

Figure 6.19 shows a comparison between the experimental and the HELIOS simulation results for the growth of the perturbed amplitude. The simulated

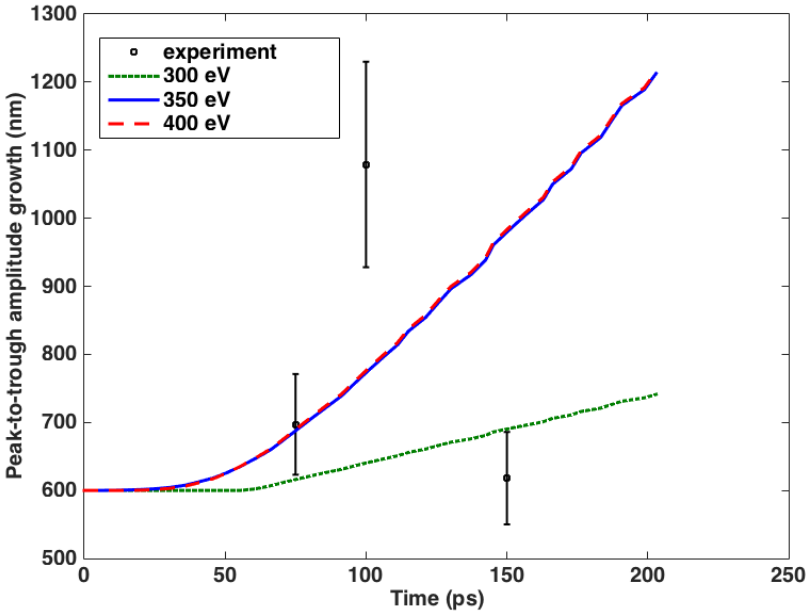

Figure 6.19: Comparison of the experimental and HELIOS simulation results for the growth of the perturbed peak-to-trough amplitude in (nm).

perturbed amplitude is estimated using (6.11) and (6.12) and using the starting temperatures of 300, 350 and 400 eV. The variation in perturbation amplitude due to the uncertainty in temperature is shown as a green dotted line 300 eV and a red dashed line for 400 eV. Generally, the growth increases more as in the experimental data and reproduces the experimental growth at 75 ps reasonably well, while it is slightly lower at 100 ps for 350 eV and 400 eV. The difference in the growth between 350 eV and 400 eV is only 3 nm. However, using 300 eV, the simulation matches within the error of the experiment at 75 ps yet at 150 ps the predicted difference between 350 eV and 300 eV is 72 nm. Several tests were performed to see at which temperature the growth rate curve can reach the experimental data at 100 ps. Generally, it was found that using higher temperatures leads to a higher growth curve and unrealistic temperature 2 KeV are needed to reproduce the experimental point at 100 ps. Interpretation of this result is not straightforward as the Cu.

Futhermore, the experimental peak-to-trough amplitude growth at 150 ps is less than at 100 ps. This is incorrect in terms of linear RT instability where the

perturbation amplitude grows exponentially with time. Figure 6.5 shows a large error bar in the perturbed wavelength at 150 ps. This indicates that this point might not part of the same series. Therefore, this point can be discarded when trying to fix the modelling results.

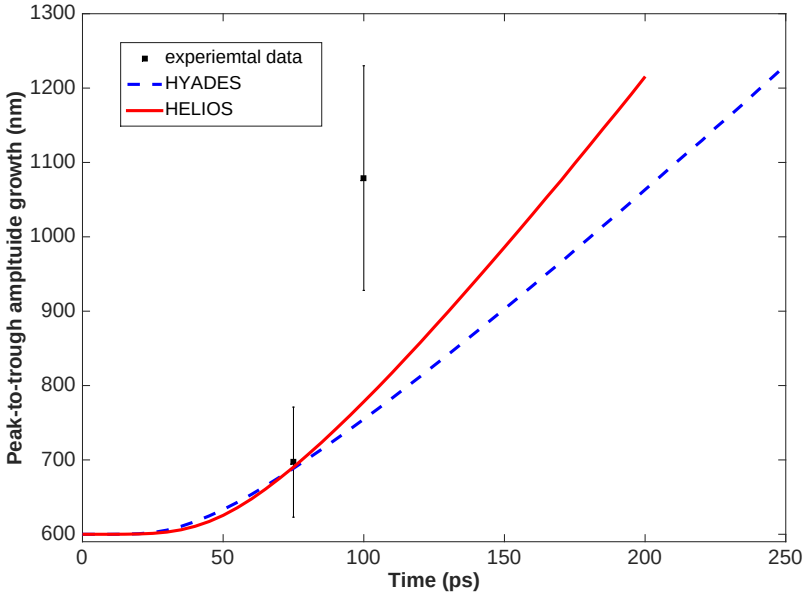

Figure 6.20: Comparison of the experimental growth of perturbed peak-to-trough amplitude in (nm) in with HYADES and HELIOS.

In addition, a comparison between the experimental data and the numerical data from HYADES and HELIOS at 400 eV is shown in Figure 6.20. As shown, the perturbed amplitude in HYADES is lower than that in HELIOS, due to the difference in the radiative cooling rate.

On the other hand, the effect of using an opacity multiplier in HYADES was investigated and it was found that using an opacity multiplier as determined at solid density does not significantly increase the RT growth rate. Also, the correction multiplier at solid density is not valid as time progresses, since the density decreases with time. The effect of using an opacity multiplier is apparent in the temperature profile up to 40 ps of the hydrodynamic simulation, as shown in Figure 6.21. Even with a time dependent opacity multiplier is unlikely HYADES can accurately track the complex emission and opacity processes of the Cu.

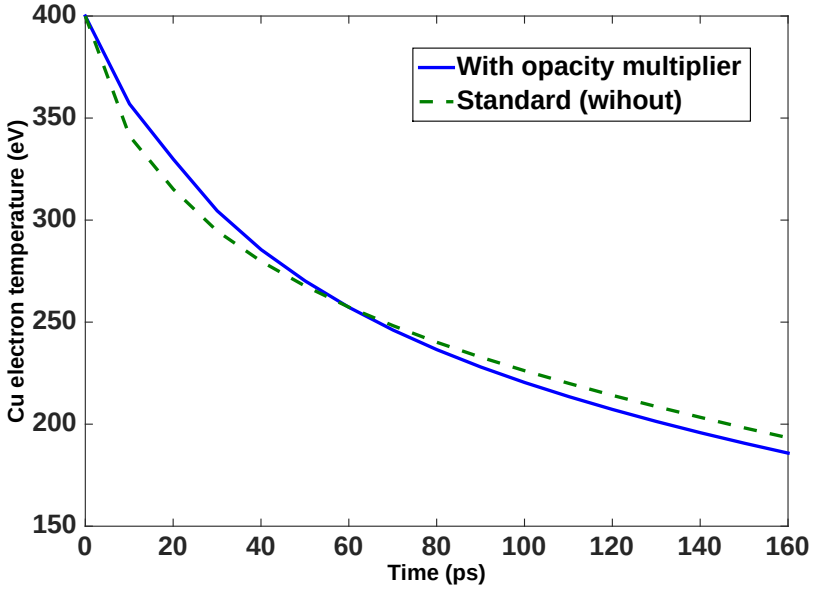

Figure 6.21: Comparing the Cu-HYADES temperature in (eV) in the case of using an opacity multiplier (blue solid line) and the standard simulation (green dashed line).

6.4 Discussion of the results

The numerical investigations of the Rossall *et al.* experiment [4] provide several important findings as follows,

1. RT target heating using the fast electrons :

   The hybrid ZEPHYROS simulation suggested the presence of filaments in the RT target even with a restriction in its thickness to 27 μm. The lack of compactness in other dimensions spoilt the uniformity of heating and minimised the positive heating effect of fast electron refluxing. The presence of filaments explains the poor contrast in the experimental radiographic raw images as they grew parallel to the sinusoidal perturbation. This poor contrast made the experimental analysis challenging resulting in the large error bars associated with measurement as shown in Figure 6.6. However, it was possible to identify the sinusoidal perturbation in the region where more uniform heating arose. This region is at a distance of 50 μm from the laser. The temperature at this distance was estimated and it was found to be 350 eV. Similar

to Cu layer temperature extracted from the experiment. The simulation also suggested that the Cu and the CH are heated to similar temperatures.

2. RT target radiative cooling:

   The biggest challenge in modelling this experiment was to obtain accurate atomic physics calculations in order to predict the radiative cooling correctly. At 350 ± 50 eV, the CH layer is highly ionised but the Cu is not, being ionised to an incomplete L-shell where a possibly large number of decaying excited states and line transitions need to be taken into account. Thus the Cu needs a detailed atomic model to obtain accurate radiative cooling. Without this, a hydro-code will incorrectly estimate the Cu radiative cooling. This is the case when using HYADES, where the simple screened hydrogenic atomic model is used, as it underestimated the radiative cooling. The CH pressure is insufficient to push the Cu and so the RT growth is under-predicted. The DCA atomic model in HELIOS predicted different radiative cooling rates, showing that the Cu radiative cooling was greater than the CH even at low temperatures.

3. RT target radiation transport:

   The accuracy of the opacity calculations plays an important role in the RT results and it was found that the effect of opacity is more important than thermal conduction and the details of the multi-group diffusion model. The importance of opacity lies in the fact that the radiative cooling calculation is affected by the emission opacity as shown in (3.31). The mean emission opacity was calculated from HELIOS and HYADES and compared to TOPS opacity. It was found that the Cu opacity is higher in HYADES than in either HELIOS or TOPS at 400 eV, thus the mean free path of emitted photons is short, which implies that Cu-HYADES was more optically thick than Cu-HELIOS. Again, this is due to the fact that the screened hydrogenic model in HYADES neglected the splitting of the energy levels, which affects the total

opacity emission.

4. RT hydrodynamic instability :

   Rapid growth of the RT has been simulated. This rapid growth occurs after an initial period of interface stability. A rapid drop in Cu pressure reverses the interface acceleration and the RT growth begins, reducing the pressure driving the interface acceleration and the Atwood number. The RT acceleration is high compared to the typical acceleration value that is observed in a long-pulse laser system by 2-3 orders of magnitude. The hydrodynamic simulation indicates that the peak RT growth rate is 8 ns^{-1} which occurs at $\approx$ 45 ps. The peak-to-trough amplitude growth increases more as in the experimental data and reproduces the experimental growth at 75 ps and slightly lower at 100 ps for 350 eV. The growth of the perturbed amplitude increases more in HELIOS, where its opacities show some agreement with TOPS opacities, than in HYADES, and this increase is more in line with the experimental data.

6.5 Summary

This chapter has concentrated on the numerical investigation of the Rossall *et al.* experiment [4] that was performed in the VULCAN TAW. In this experiment, a CH-Cu target with a machined sinusoidal interface was X-ray radiographed face-on to measure the growth in the sinusoidal with time. The simulation of this experiment explored fast electron heating, radiative cooling, radiation transport and RT instability.

This work shows that it is possible to drive the RT instability in a target heated by the fast electrons. However, uniform heating is vital for clear observation of the sinusoidal perturbations. Also, the modelling of this experiment shows the importance of including a robust atomic physics model in hydrodynamic codes. There are a number of areas in which improvements can be made in both the experiment and

the modelling, and these are discussed later in Chapter 7 as recommendations for future work.

Chapter 7

Conclusions and future work

7.1 Summary and Conclusions

This thesis has numerically investigated fast electron heating, with the aim of improving the isochoric heating across the depth in the target. The research has shown that careful design of a thick target is essential to minimise fast electron spreading, which is one of the main mechanisms that obstruct fast electron transport and target heating. Here, we have shown that a wire-like shaped target with transverse confinement of the fast electrons can increase to some extent the uniformity of heating across the depth. We have also found that grading the atomic number at the interface of the resistive guide increases the uniformity of heating across the depth in the guide. The graded interface configuration minimises the annular transport effect and increases the powerful confining magnetic fields which both consequently improve the uniformity of the heating. These guide targets are also more tolerant to laser pointing stability. In addition, we have shown that a target with uniform isochoric fast electron heating is a useful tool with which to investigate hydrodynamic instabilities such as the RT instability.

The thesis began with a brief introduction to fast electron transport and explained the motivation for the fast electron heating study. Chapter 2 has discussed the basic physics of fast electron transport and given a description of the hybrid-

particle ZEPHYROS code, which has been used to carry out the numerical investigation of the fast electron transport. The main physics relevant to Rayleigh-Taylor instability and radiative losses has been explained in Chapter 3.

In Chapter 4, the hindrances to the fast electron transport in a solid target have been discussed with respect to the fast electron beam direction; these are the electric field inhibition, filamentation and the fast electron spreading. The latter effect has been minimised by redesigning the target to be wire-like, so that the transverse directions of the target and the source diameter spot size are comparable. This target design has been numerically tested and found to provide excellent transverse fast electron confinement. Uniform transverse heating was also obtained due to this confinement. However, regardless the control of the fast electron spreading, the fast electron density across the depth in the target was impeded by both the electric field inhibition and the angular dispersion. This impairs in target heating across its depth. Since the angular dispersion has not yet been addressed in the context of the fast electron transport, analytical and numerical investigations have been performed to measure its extent. It was found that the angular dispersion has a quadratic effect on the Ohmic heating. This significantly reduces the heating rate. The reason for this is that the fast electron density drops across the depth as the fast electron beam is longitudinally dispersed. Thus, decreasing the resistive background electron density needed to balance the fast electrons. This drives a strong temperature gradient along the wire-like target depth. Angular dispersion is significant after the end of the electron beam injection and it reduces the heating by a factor of 4. In addition, it impedes the fast electron density more strongly than electric field inhibition, resistive magnetic field, drag and scattering effects. However, the angular dispersion effect can be reduced using lower divergence angle and longer fast electron beam pulse duration so that more uniformity in heating can be obtained. The results of this chapter have confirmed the importance of considering the effects of angular dispersion in the fast electron transport calculations.

In Chapter 5, improvement on the heating in a larger radius of the resistive guide has been discussed. A larger resistive guide is needed as it is more tolerance to pointing stability of the laser. The nonuniform propagation of the fast electrons and heating inside the larger guide is inferred by the development of interior magnetic fields within the guide close to the axis and formation of annular heating pattern. The heating is improved by grading the atomic number at the interface between the guide element and the solid substrate. We referred to this as "graded interface configuration". The main condition for best performance of this graded interface configuration is that the ratio between the core of the wire that has not been graded to the laser spot radius must be less than 1. This configuration investigated in standard, pure-Z and multilayered-Z resistive guiding schemes. Generally, the graded interface configuration helps to collimate the fast electrons to higher resistivity region uniformly which improve both the magnetic collimation and guide heating. In pure-Z resistive guide scheme, the graded interface configuration helps to collimate the fast electrons to higher resistivity region uniformly, producing heating comparable to the heating obtained in smaller guides. Also, it produces more powerful azimuthal magnetic fields at the boundary between the guide element and the solid substrate, leading to increased heating in the guide. In multilayered-Z resistive guide scheme, this configuration minimises effect of interior magnetic fields to some extent which improves the heating. In addition, it was found that the graded interface configuration increases the azimuthal magnetic flux density B_ϕ in the standard-Z guide scheme by 24% while increases the width L_ϕ in the multilayered-Z guide scheme by 50% at the end of the laser pulse. A faster and higher azimuthal magnetic field rate obtained when the interface is graded in Z in standard-Z scheme. The typical values of the product $B_\phi L_\phi$ are obtained at the first 200 fs of the interaction in this scheme. This increases the guide heating as more fast electrons are confined at early time of interaction. Higher energetic fast electrons are confined in pure-Z and multilayered-Z guides with graded interfaces.

Chapter 6 has explored numerically the Rayleigh-Taylor instability experiment driven using a fast electron heated target. The numerical investigation has been divided into four sections in order to study the different aspects of the physics affecting the RT instability. The first section concerned the fast electron heating of the RT target. The simulation has suggested the presence of filaments, although the RT target thickness was thin, 27 μm. Because of the lack of compactness in other directions of the target, the uniformity of heating was spoilt by filament growth. These filaments grow in the direction parallel to the sinusoidal perturbation seeded for RT instability which affects the ability to identify the perturbation and worsens the contrast of the backlighter images. This poor contrast made the experimental analysis challenging resulting in the large error bars associated with measurement. It was possible to identify the sinusoidal perturbation in the region where more uniform heating arose. This was at depth of 50 μm. The temperature was estimated at this depth and found to be in agreement with the experimental Cu temperature 350 ± 50 eV with divergence angles of $50° - 60°$. Also, the simulation has suggested that at this depth the Cu and CH are heated to a similar temperature. The second section investigated the RT target cooling rate. This investigation was performed using two hydro-codes, HELIOS and HYADES, where two different atomic models. At 350 ± 50 eV, the CH layer is highly ionised but the Cu is not, being ionised to an incomplete L-shell where a possibly large number of decaying excited states and line transitions need to be taken into account. Thus, the Cu needs a detailed atomic model. The screened hydrogenic model in HYADES underestimates the cooling rate of the Cu which affects the hydrodynamic motion. The CH pressure was insufficient to push the Cu and so the RT growth is under-predicted. The DCA model in HELIOS showing a greater cooling rate for Cu than for CH even at lower temperature and produces higher RT growth rate. The radiative cooling results led to the third section of the investigation which concerned radiation transport. The importance of opacity lies in the fact that the radiative cooling calculations are

affected by the emission opacity. It has been shown that the Cu opacity is higher in HYADES than in either HELIOS or TOPS opacities. Thus, the simulated RT target in HYADES emits its radiation faster than in HELIOS. The last section investigated the hydrodynamic RT instability. A rapid growth was experimentally observed and the predicted growth obtained from HELIOS simulation was more in line with the experimental data compared to HYADES. The RT acceleration is high compared to the typical acceleration value that is observed in a long-pulse laser system by 2-3 orders of magnitude. The hydrodynamic simulation indicates that the peak RT growth rate is 8 ns^{-1} which occurs at $\approx$ 45 ps. The simulations of this experiment have shown that the RT instability can be driven using short pulse laser system. However, the uniformity of fast electron heating is vital to drive this instability.

7.2 Future work

This section outlines some suggestions for further research. This is restricted to three topics discussed in this thesis; the angular dispersion model, graded-interface of the resistive guide and the RT instability experiment concept.

The angular dispersion model needs to be extended to incorporate the fast electron density predictive capability, parameterising of the laser parameters and materials properties such as lattice structure. Furthermore, angular dispersion needs to be explored with drive laser parameters relevant to the Fast Ignition, i.e. 20 kJ energy and 20 ps laser pulse duration, since it is expected that this may influence the ignition and coupling of the compressed fuel and fast electrons.

In terms of graded interface configuration, this concept needs to be extended to other geometries, for example, in a conical guide [75] for minimising the annular transport and increasing fast electron focusing. Ongoing work includes a comparison of the graded interface resistive guide and a bi-structured resistive guide.

With regard to the RT instability driven in the fast electron heated target, developments can be made to both experimental and numerical investigations. Ex-

perimentally, an extended wire technique could be used as a method of controlling heating uniformity in the transverse direction in order to prevent filamentation. In addition, it would also be useful to measure both the Cu and CH temperatures, e.g. with a dopant, as the simulation of this experiment needs precise initial temperatures for both materials. Numerically, this experiment needs to be explored using a 2D hydrodynamic code in order to study the effects of lateral expansion and the effect of thermal conduction, and to measure the change in transmission. Detailed atomic physics needs to be used in the 2D modelling. Furthermore, the effect of filamentation should be included in the modelling as this contributes to changes in the RT growth rate and to study the effect of the filaments on the interface.

Appendix A

Convergence in ZEPHYROS

In this appendix, the convergence in ZEPHYROS is briefly discussed. The number of the macroparticles is essential to obtain high resolution and to reduce the statistical noise. Statistical noise is the unexplained variation in the simulation due to error or residual. This noise can be decreased via using more macroparticles in a simulation since it scales as $N^{-1/2}$ [124]. This requires more computational resources and a balance needs to be made. In ZEPHYROS, the acceptable macroparticles is tested using Target A (see Chapter 4) and the results is shown in Figure A.1.

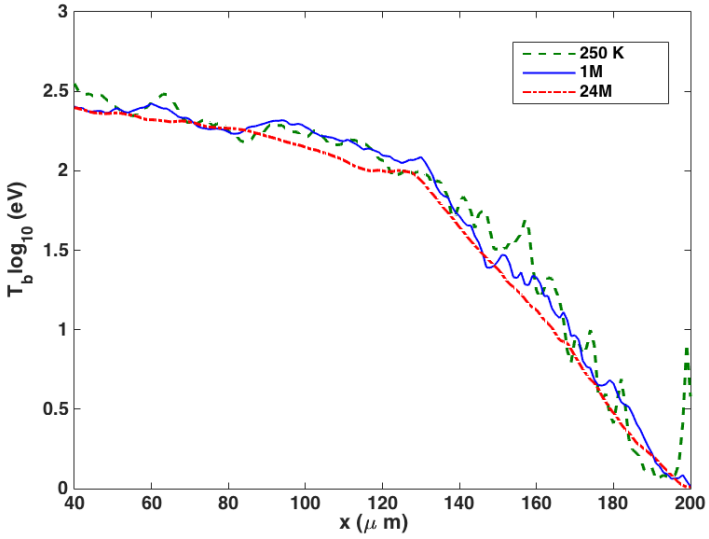

Figure A.1: Line-out of background temperature using logarithmic scale for three different number of macroparticles, 250 thousand, 1 Million and 24 Million

This Figure shows a plot of the background temperature as function of distance in logarithmic scale using three different number of macroparticles 2.5×10^5, 10^6 and 2.4×10^7. As shown, the noise decreases with increasing the number and more smooth line is obtained. The average number of particle per cell is 20, 80 and 1940 for 2.5×10^5, 10^6 and 2.4×10^7, respectively. In this thesis, above 100 particle/cell is used.

Appendix B

Fast electron trajectory inside the guide

The fast electron trajectory inside the guide is shown in this appendix. The fast electron motion is affected by the magnetic field flux density, it width and the wire diameter. The information that provide in both Tables 5.1 and 5.2 is used in this study. A particle pusher code is firstly described, followed by the results of this study.

B.0.1 Particle pusher code

A sample particle pusher code has been written to study the trajectory of the single fast electron motion inside the guide. In this type of code, the positions and momentum of the fast electrons are updated using the leapfrog scheme and Boris algorithm [38, 143] respectively. The position updating is performed in $3P$, where $P = \gamma m_e c$ is the momentum and γ is the Lorentz factor. Each position is evaluated at integral time steps while the momentum is evaluated at half times. For example the position in the x-direction,

$$x^{n+1} = x^n + \frac{\Delta t}{\gamma^{n+1/2} m_e} \mathbf{P}_x^{n+1/2} \tag{B.1}$$

where Δt is the time step size and $\mathbf{P}_x$ is the momentum in the x-direction. The momentum updating is done by the Boris algorithm, which is commonly used in plasma simulations because of its stability and simplicity. In this method, the electric field $\mathbf{E}$ and magnetic field $\mathbf{v} \times \mathbf{B}$ are entirely separated in the discretised equation of motion. Following the discussion in Ref. [38], this algorithm can be divided into three main steps. Firstly, fast electrons are accelerated in the electric field for a half time step,

$$\mathbf{P}^{-} = \mathbf{P}^{n-1/2}_{x,y,z} - \frac{1}{2} e \mathbf{E}^{n} \delta t \tag{B.2}$$

where $\mathbf{P}^{-} = (\mathbf{P}^{-}_{x}, \mathbf{P}^{-}_{y}, \mathbf{P}^{-}_{z})$ is the momentum, e is the electron charge and $\mathbf{E}^{n} = (\mathbf{E}_x, \mathbf{E}_y, \mathbf{E}_z)$ is the electric field. Equation (B.2) is the discretised equation of motion for the electric field. Secondly, the discretised equation of motion for the magnetic field is written as,

$$\frac{\mathbf{P}^{+} - \mathbf{P}^{-}}{\Delta t} = -\frac{e}{2 m_e \gamma^{*}} (\mathbf{P}^{+} + \mathbf{P}^{-}) \times \mathbf{B}^{n} \tag{B.3}$$

where $\mathbf{P}^{+} = (\mathbf{P}^{+}_{x}, \mathbf{P}^{+}_{y}, \mathbf{P}^{+}_{z})$ is the momentum, γ^{*} is the constant Lorentz factor during this step (since this step does not do any work on the fast electrons) and $\mathbf{B}^{n} = (\mathbf{B}_x, \mathbf{B}_y, \mathbf{B}_z)$ is the magnetic field. Equation (B.3) is re-arranged into the following set of three linear equations,

$$\mathbf{P}^{+}_{x} - \mathbf{P}^{-}_{x} = -\alpha_z \mathbf{P}^{+}_{y} + \alpha_y \mathbf{P}^{+}_{z} - \alpha_z \mathbf{P}^{-}_{y} + \alpha_y \mathbf{P}^{-}_{z} \tag{B.4}$$

$$\mathbf{P}^{+}_{y} - \mathbf{P}^{-}_{y} = \alpha_z \mathbf{P}^{+}_{x} - \alpha_x \mathbf{P}^{+}_{z} + \alpha_z \mathbf{P}^{-}_{x} - \alpha_x \mathbf{P}^{-}_{z} \tag{B.5}$$

$$\mathbf{P}^{+}_{z} - \mathbf{P}^{-}_{z} = -\alpha_y \mathbf{P}^{+}_{x} + \alpha_x \mathbf{P}^{+}_{y} - \alpha_y \mathbf{P}^{-}_{x} + \alpha_x \mathbf{P}^{-}_{y} \tag{B.6}$$

where,

$$\alpha_{x,y,z} = \frac{e \Delta t}{2 m_e \gamma^{*}} \mathbf{B}_{x,y,z} \tag{B.7}$$

Equations (B.4) to (B.6) are re-written in the matrix form then solved for $\mathbf{P}^{+}$.

Thirdly, the momentum of each direction is updated by accelerating the fast electrons again by the electric field for half a time step,

$$\mathbf{P}_{x,y,z}^{n+1/2} = \mathbf{P}^{+} - \frac{1}{2} e \mathbf{E}^{n} \delta t \tag{B.8}$$

B.0.1.1 Results

To study the motion of single fast electron inside the guide. The information of the wire radius r_{wire} in Table 5.1 and the magnetic flux density and its width in Table 5.2 are used in the code as input. The electric field value is extracted from ZEPHYROS for each run and it found is of order of 10^8 Vm^{-1}. The magnetic field profile in the pusher code is gaussian as previously shown in Figure 5.2. The fast electron is injected at angle of 90°.

Figure B.1 show the single fast electron motion inside the Run A and B as function of distance . The fast electron oscillates in Run B (small wire diameter) faster than in Run A (large wire diameter). In these two runs, both values of B_ϕ and L_ϕ are comparable. The conclusion is faster fast electron oscillation is obtained with reduced wire radius. The results of Run C is not shown here as the results are similar to Run B.

Single fast electron trajectory is estimated for Runs D and E. Both runs have the same wire radius while the values of B_ϕ and L_ϕ are different. The affect of this difference is clear in Figure B.2. The fast electron oscillates faster in Run E compared to Run D. This is due the large width L_ϕ in Run E and it is in line with the kinetic energy of the fast electron as shown in Table 5.2. With larger L_ϕ, the fast electron circular segment touches the near side of the confining region. Thus, the electron reflects back towards the axis faster than in the case of Run D where the width is small compared to Run E.

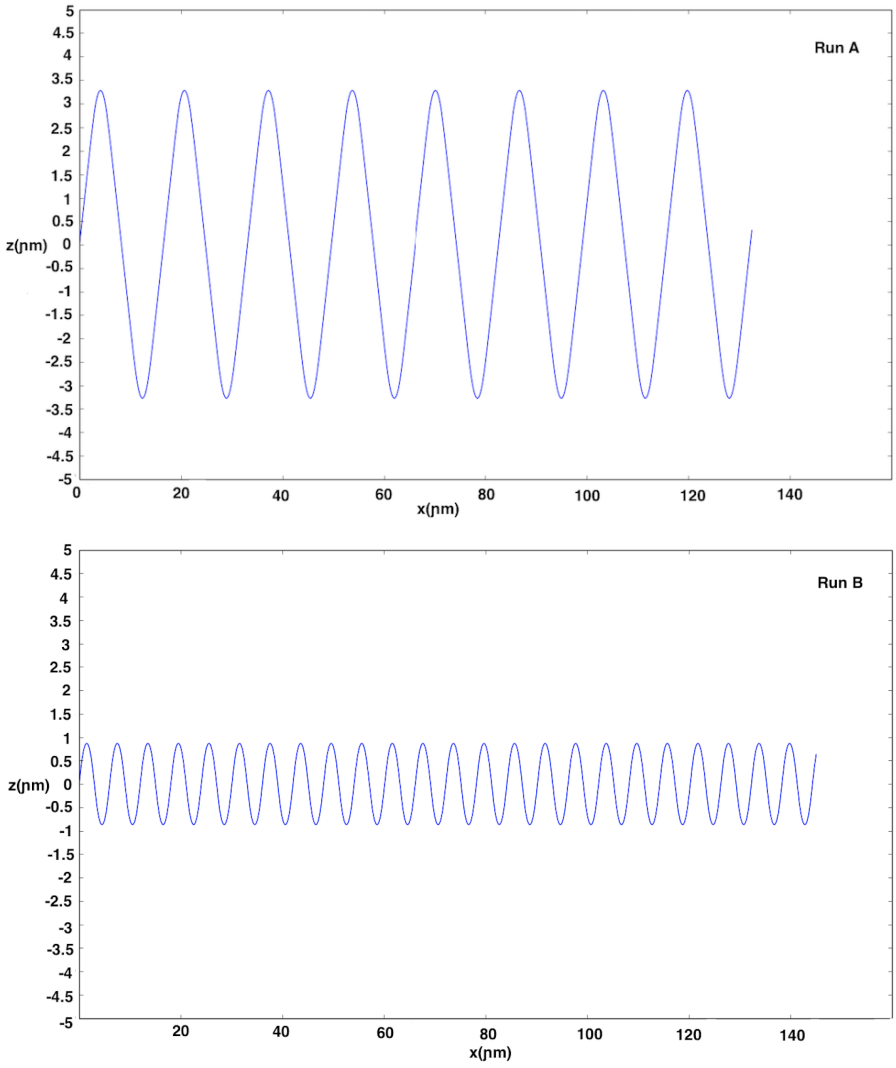

Figure B.1: The fast electron trajectory in Runs A and B

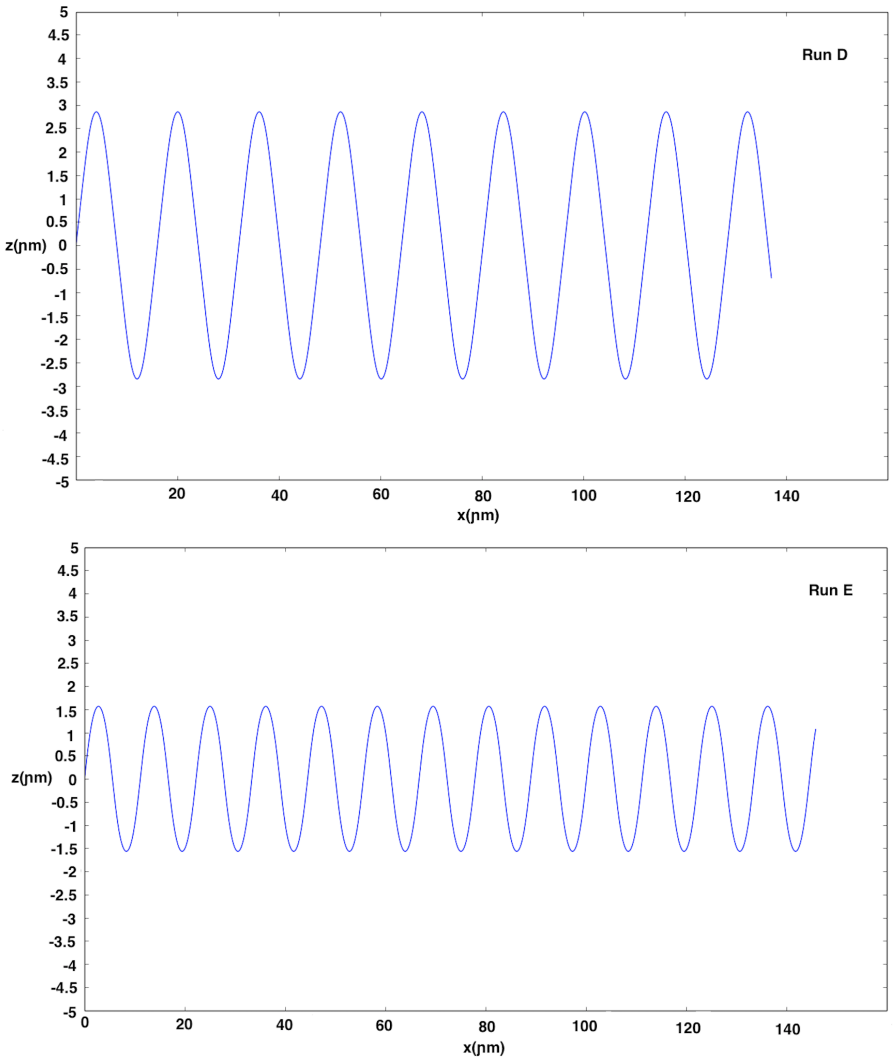

Figure B.2: The fast electron trajectory in Runs D and E

Symbols and Abbreviations

α	Effect of angular dispersion.
β	Fraction of laser energy coupled into the fast electrons.
β_s	Ratio between electron velocity to speed of light.
β_{ablate}	Adjustable factor in Ablative Rayleigh-Taylor instability.
ϵ_0	Vacuum permittivity.
$\bar{\epsilon_f}$	Fast electron mean energy.
η	Resistivity.
η_ν	Emissivity.
γ	Lorentz factor.
γ_{RT}	Rayleigh-Taylor growth rate.
$\gamma_{e,i}$	Number of degrees of freedom for each species, electrons and ions.
γ_{TSE}	growth rate of TSF mode.
κ_ν	Opacity.
$\kappa_{<\nu>p}$	Planckian mean opacity.
$\kappa_{<\nu>R}$	Rosseland mean opacity.
$\kappa_{\nu p_{g_i}}$	Planckian mean opacity for frequency group g_i.
$\kappa_{e,i}$	Thermal conductivity coefficient for electrons and ions.
λ	Wavelength of the sinusoidal perturbation.
λ_L	Wavelength of the laser.
λ_ν	Mean free path of photons.
λ_{ei}	The electron-ion collision mean free path.

λ_D	Debye length.
μ	Chemical potential.
μ_0	Permeability of free space.
μ_ν	Absorption coefficient.
ν	Radiation frequency.
$\bar{\nu}_{ei}$	Background electron-ion collision rate.
ω	Wave frequency.
ω_L	Laser frequency.
ω_{pe}	Plasma frequency.
ϕ	Potential velocity.
$\phi_{h,l}$	Potential velocity of heavier and lighter fluids.
Φ_L	Absorbed laser flux.
$\Delta\Phi$	Electric field potential energy.
ρ	Mass density.
$\rho_{h,l}$	Mass density of the heavier and lighter fluids.
ρ_{avg}	Mass density at the interface.
τ_L	Laser pulse duration.
τ_0	Fast electron duration.
τ_{scatter}	Collisional scattering time of the fast electrons.
τ_e	Electron relaxation time.
τ_{f-b}	Fast-background electron collision time .
$\tau_{e-folding}$	e-folding growth time.
τ_ν	Optical depth.
τ_{ei}	Inverse of electron-ion collision time.
θ_L	Angle of the laser incident.
θ_d	divergence angle.
ζ	Spatial amplitude of the single-mode of the perturbation.
ζ_0	Initial spatial amplitude of perturbation.
$\varepsilon_{e,i}$	Energy density of electrons and ions.

ΔT	Change in Transmission.
Γ	Coulomb coupling parameter.
Γ_{Col}	Collimation parameter.
$\ln\Lambda$	Coulomb logarithm.
χ	Smoothing ratio of the wire radius to the laser spot radius.
ψ	Mixed fraction of materials.
B_ν	Normalised Planck blackbody function.
B_ϕ	Azimuthal magnetic density flux field.
c_s	Adiabatic sound speed.
I_L	Laser intensity.
I_ν	Spectral radiation intensity.
$I_{\nu 0}$	Initial spectral radiation intensity.
L_s	Scale length.
L_0	fast electron penetration depth due to beam divergence.
L_ϕ	Width of the azimuthal magnetic field.
Q_{ei}	Electron-ion heat exchange rate.
R	Fast electron beam radius.
r_s	interatomic spacing.
$\mathbf{r}_g$	Larmor radius.
x_0	fast electron penetration depth due to electric field inhibition.

Bibliography

[1] P. McKenna, F. Lindau, O. Lundh, D. Neely, A. Persson, and C. Wahlström, "High-intensity laser-driven proton acceleration: influence of pulse contrast," *Philosophical Transactions of the Royal Society A: Mathematical, Physical and Engineering Sciences*, vol. 364, p. 711, 2006.

[2] S. Kar, A. P. L. Robinson, D. C. Carroll, O. Lundh, K. Markey, P. McKenna, P. Norreys, and M. Zepf, "Guiding of relativistic electron beams in solid targets by resistively controlled magnetic fields," *Phys. Rev. Lett.*, vol. 102, p. 055001, 2009.

[3] B. Ramakrishna, S. Kar, A. P. L. Robinson, D. J. Adams, K. Markey, M. N. Quinn, X. H. Yuan, P. McKenna, K. L. Lancaster, J. S. Green, R. H. H. Scott, P. A. Norreys, J. Schreiber, and M. Zepf, "Laser-driven fast electron collimation in targets with resistivity boundary," *Phys. Rev. Lett.*, vol. 105, p. 135001, 2010.

[4] A. K. Rossall, I. A. Bush, C. P. Edwards, G. J. Tallents, N. C. Woolsey, P. J., W. Nazzarov, K. Lancaster, T. Winstone, C. Spindloe, H. Lowe, and P. Morantz, "Measurement of Rayleigh-Taylor instability growth in a layered target heated by a high power short pulse laser," *CLF Annual Report*, 2010-2011.

[5] A. K. Rossall, "Characterisation and measurement of laser produced plasma emission and applications in opacity experiments," *University of York*, 2011.

[6] J. Colvin and J. Larsen, *Extreme Physics: Properties and Behavior of Matter at Extreme Conditions*. Cambridge University Press, 2013.

[7] S. Pfalzner, *An introduction to inertial confinement fusion*. CRC Press, 2006.

[8] P. Gibbon, *Short pulse laser interactions with matter*. World Scientific Publishing Company, 2004.

[9] S. C. Wilks and W. L. Kruer, "Absorption of ultrashort, ultra-intense laser light by solids and overdense plasmas," *IEEE Journal of Quantum Electronics*, vol. 33, p. 1954, 1997.

[10] P. K. Patel, A. J. Mackinnon, M. H. Key, T. E. Cowan, M. E. Foord, M. Allen, D. F. Price, H. Ruhl, P. T. Springer, and R. Stephens, "Isochoric heating of solid-density matter with an ultrafast proton beam," *Phys. Rev. Lett.*, vol. 91, p. 125004, 2003.

[11] J. E. Bailey, G. A. Rochau, R. C. Mancini, C. A. Iglesias, J. J. MacFarlane, I. E. Golovkin, C. Blancard, P. Cosse, and G. Faussurier, "Experimental investigation of opacity models for stellar interior, inertial fusion, and high energy density plasmas(a)," *Phys. Plasmas*, vol. 16, p. 058101, 2009.

[12] S. Atzeni and J. Meyer-ter Vehn, *The Physics of Inertial Fusion: BeamPlasma Interaction, Hydrodynamics, Hot Dense Matter: BeamPlasma Interaction, Hydrodynamics, Hot Dense Matter*, vol. 125. Oxford University Press, 2004.

[13] P. Neumayer, H. J. Lee, D. Offerman, E. Shipton, A. Kemp, A. L. Kritcher, T. Döppner, C. A. Back, and S. H. Glenzer, "Isochoric heating of reduced mass targets by ultra-intense laser produced relativistic electrons," *High Energy Density Physics*, vol. 5, p. 244, 2009.

[14] F. Perez, L. Gremillet, M. Koenig, S. D. Baton, P. Audebert, M. Chahid, C. Rousseaux, M. Drouin, E. Lefebvre, T. Vinci, J. Rassuchine, T. Cowan,

S. A. Caillard, K. A. Flippo, and R. Shepherd, "Enhanced isochoric heating from fast electrons produced by high-contrast, relativistic-intensity laser pulses," *Phys. Rev. Lett.*, vol. 104, p. 085001, 2010.

[15] G. Dyer, R. Sheppherd, J. Kuba, E. Fill, A. Wootton, P. Patel, D. Price, and T. Ditmire, "Isochoric heating of solid aluminium with picosecond X-ray pulses," *Journal of Modern Optics*, vol. 50, p. 2495, 2003.

[16] D. H. Sharp, "An overview of Rayleigh-Taylor instability," *Physica D: Nonlinear Phenomena*, vol. 12, p. 3, 1984.

[17] J. E. Bailey, G. A. Rochau, R. C. Mancini, C. A. Iglesias, J. J. MacFarlane, I. E. Golovkin, C. Blancard, P. Cosse, and G. Faussurier, "Experimental investigation of opacity models for stellar interior, inertial fusion, and high energy density plasmasa)," *Phys. Plasmas*, vol. 16, p. 058101, 2009.

[18] G. Huser, M. Koenig, A. Benuzzi-Mounaix, E. Henry, T. Vinci, B. Faral, M. Tomasini, B. Telaro, and D. Batani, "Temperature and melting of laser-shocked iron releasing into an LiF window," *Phys. Plasmas*, vol. 12, p. 060701, 2005.

[19] R. G. Evans, E. L. Clark, R. T. Eagleton, A. M. Dunne, R. D. Edwards, W. J. Garbett, T. J. Goldsack, S. James, C. C. Smith, B. R. Thomas, R. Clarke, D. J. Neely, and S. J. Rose, "Rapid heating of solid density material by a petawatt laser," *Appl. Phys. Lett.*, vol. 86, p. 191505, 2005.

[20] M. Sherlock, E. G. Hill, R. G. Evans, S. J. Rose, and W. Rozmus, "In-depth plasma-wave heating of dense plasma irradiated by short laser pulses," *Phys. Rev. Lett.*, vol. 113, p. 255001, 2014.

[21] A. R. Bell, J. R. Davies, S. Guerin, and H. Ruhl, "Fast-electron transport in high-intensity short-pulse laser-solid experiments," *Plasma Phys. Control. Fusion*, vol. 39, p. 653, 1997.

[22] K. L. Lancaster, J. S. Green, D. S. Hey, K. U. Akli, J. R. Davies, R. J. Clarke, R. R. Freeman, H. Habara, M. H. Key, R. Kodama, K. Krushelnick, C. D. Murphy, M. Nakatsutsumi, P. Simpson, R. Stephens, C. Stoeckl, T. Yabuuchi, M. Zepf, and P. A. Norreys, "Measurements of energy transport patterns in solid density laser plasma interactions at intensities of $5 \times 10^{20}\mathrm{Wcm}^{-2}$," *Phys. Rev. Lett.*, vol. 98, p. 125002, 2007.

[23] J. S. Green, V. M. Ovchinnikov, R. G. Evans, K. U. Akli, H. Azechi, F. N. Beg, C. Bellei, R. R. Freeman, H. Habara, R. Heathcote, M. H. Key, J. A. King, K. L. Lancaster, N. C. Lopes, T. Ma, A. J. MacKinnon, K. Markey, A. McPhee, Z. Najmudin, P. Nilson, R. Onofrei, R. Stephens, K. Takeda, K. A. Tanaka, W. Theobald, T. Tanimoto, J. Waugh, L. Van Woerkom, N. C. Woolsey, M. Zepf, J. R. Davies, and P. A. Norreys, "Effect of laser intensity on fast-electron-beam divergence in solid-density plasmas," *Phys. Rev. Lett.*, vol. 100, p. 015003, 2008.

[24] L. Gremillet, G. Bonnaud, and F. Amiranoff, "Filamented transport of laser-generated relativistic electrons penetrating a solid target," *Phys. Plasmas*, vol. 9, p. 941, 2002.

[25] P. Norreys, D. Batani, S. Baton, F. N. Beg, R. Kodama, P. M. Nilson, P. Patel, F. Pérez, J. J. Santos, R. Scott, V. Tikhonchuk, M. Wei, and J. Zhang, "Fast electron energy transport in solid density and compressed plasma," *Nucl. Fusion*, vol. 54, p. 054004, 2014.

[26] D. A. Chapman, S. J. Hughes, D. J. Hoarty, and D. J. R. Swatton, "Hot electron transport modelling in fast ignition relevant targets with non-spitzer resistivity," in *J.Phys.: Conf. Ser.*, vol. 244, p. 022031, 2010.

[27] A. P. L. Robinson, D. J. Strozzi, J. R. Davies, L. Gremillet, J. J. Honrubia, T. Johzaki, R. J. Kingham, M. Sherlock, and A. A. Solodov, "Theory of fast electron transport for fast ignition," *Nucl. Fusion*, vol. 54, p. 054003, 2014.

[28] Y. Sentoku, T. E. Cowan, A. Kemp, and H. Ruhl, "High energy proton acceleration in interaction of short laser pulse with dense plasma target," *Phys. Plasmas*, vol. 10, p. 2009, 2003.

[29] M. Borghesi, J. Fuchs, S. V. Bulanov, A. J. Mackinnon, P. K. Patel, and M. Roth, "Fast ion generation by high-intensity laser irradiation of solid targets and applications," *Fusion Science and Technology*, vol. 49, p. 412, 2006.

[30] D. Umstadter, J. Workman, A. Maksimchuk, X. Liu, U. Ellenberger, J. S. Coe, and C.-Y. Chien, "Picosecond X-rays from subpicosecond-laser-produced hot-dense matter," *Journal of Quantitative Spectroscopy and Radiative Transfer*, vol. 54, p. 401, 1995.

[31] M. Tabak, J. Hammer, M. E. Glinsky, W. L. Kruer, S. C. Wilks, J. Woodworth, E. M. Campbell, M. D. Perry, and R. J. Mason, "Ignition and high gain with ultrapowerful lasers," *Phys. Plasmas*, vol. 1, p. 1626, 1994.

[32] D. Strickland and G. Mourou, "Compression of amplified chirped optical pulses," *Optics communications*, vol. 55, p. 447, 1985.

[33] S. C. Wilks, W. L. Kruer, M. Tabak, and A. B. Langdon, "Absorption of ultra-intense laser pulses," *Phys. Rev. Lett.*, vol. 69, p. 1383, 1992.

[34] S. Eliezer, *The interaction of high-power lasers with plasmas*, vol. 1^{st} edn. IOP publishing, 2002.

[35] K. B. Wharton, S. P. Hatchett, S. C. Wilks, M. H. Key, J. D. Moody, V. Yanovsky, A. A. Offenberger, B. A. Hammel, M. D. Perry, and C. Joshi, "Experimental measurements of hot electrons generated by ultraintense ($>$ 10^{19} Wcm^{-2}) laser-plasma interactions on solid-density targets," *Phys. Rev. Lett.*, vol. 81, p. 822, 1998.

[36] K. Yasuike, M. H. Key, S. P. Hatchett, R. A. Snavely, and K. Wharton, "Hot electron diagnostic in a solid laser target by K-shell lines measurement from

ultraintense laser–plasma interactions (3×10^{20} Wcm^{-2},$\leq$400 J)," *Rev. Sci. Instrum.*, vol. 72, p. 1236, 2001.

[37] F. Brunel, "Not-so-resonant, resonant absorption," *Phys. Rev. Lett.*, vol. 59, p. 52, 1987.

[38] P. McKenna, D. Neely, R. Bingham, and D. Jaroszynski, *Laser-Plasma Interactions and Applications.* Springer, 2013.

[39] D. A. Jaroszynski, R. A. Bingham, and R. A. Cairns, *Laser-plasma interactions.* CRC Press, 2009.

[40] F. N. Beg, A. R. Bell, A. E. Dangor, C. N. Danson, A. P. Fews, M. E. Glinsky, B. A. Hammel, P. Lee, P. A. Norreys, and M. Tatarakis, "A study of picosecond laser–solid interactions up to 10^{19} Wcm^{-2}," *Phys, Plasmas,*, vol. 4, p. 447, 1997.

[41] M. Sherlock, "Universal scaling of the electron distribution function in one-dimensional simulations of relativistic laser-plasma interactions," *Phys.Plasmas*, vol. 16, p. 103101, 2009.

[42] T. Kluge, T. Cowan, A. Debus, U. Schramm, K. Zeil, and M. Bussmann, "Electron temperature scaling in laser interaction with solids," *Phys. Rev. Lett.*, vol. 107, p. 205003, 2011.

[43] H. Alfvén, "On the motion of cosmic rays in interstellar space," *Phys. Rev.*, vol. 55, p. 425, 1939.

[44] J. D. Huba, *NRL: plasma formulary.* 2007.

[45] R. R. Freeman, D. Batani, S. Baton, M. Key, and R. Stephens, "The generation and transport of large currents in dense materials: The physics of electron transport relative to fast ignition," *Fusion science and technology*, vol. 49, p. 297, 2006.

[46] Y. T. Lee and R. M. More, "An electron conductivity model for dense plasmas," *Phys. Fluids*, vol. 27, p. 1273, 1984.

[47] S. M. Guerin, A. R. Bell, J. R. Davies, and M. G. Haines, "One-dimensional particle simulations of fast electron transport in solid targets," *Plasma Phys. Control. Fusion*, vol. 41, p. 285, 1999.

[48] A. R. Bell, A. P. L. Robinson, M. Sherlock, R. J. Kingham, and W. Rozmus, "Fast electron transport in laser-produced plasmas and the KALOS code for solution of the Vlasov–Fokker–Planck equation," *Plasma Phys. Control. Fusion*, vol. 48, p. R37, 2006.

[49] A. P. L. Robinson, H. Schmitz, and P. McKenna, "Resistivity of non-crystalline carbon in the 1–100 ev range," *New Journal of Physics*, vol. 17, p. 083045, 2015.

[50] H. R. Rüter and R. Redmer, "Ab initio simulations for the ion-ion structure factor of warm dense aluminum," *Phys. Rev. Lett.*, vol. 112, p. 145007, 2014.

[51] D. A. MacLellan, D. C. Carroll, R. J. Gray, N. Booth, M. Burza, M. P. Desjarlais, F. Du., B. Gonzalez-Izquierdo, D. Neely, H. W. Powell, A. P. L. Robinson, D. R. Rusby, G. G. Scott, X. H. Yuan, C. Wahlstrom, and P. McKenna, "Annular fast electron transport in silicon arising from low-temperature resistivity," *Phys. Rev. Lett.*, vol. 111, p. 095001, 2013.

[52] F. F. Chen, "Introduction to plasma physics and controlled fusion volume 1: Plasma physics," vol. 2^{nd}edn., 1985.

[53] X. H. Yang, M. Borghesi, and A. P. L. Robinson, "Fast-electron self-collimation in a plasma density gradient," *Phys. Plasmas*, vol. 19, p. 062702, 2012.

[54] M. E. Glinsky, "Regimes of suprathermal electron transport," *Phys.Plasmas*, vol. 2, p. 2796, 1995.

[55] H. Bethe, "Zur theorie des durchgangs schneller korpuskularstrahlen durch materie," *Annalen der Physik*, vol. 397, p. 325, 1930.

[56] H. Bethe, "Bremsformel für elektronen relativistischer geschwindigkeit," *Zeitschrift für Physik*, vol. 76, p. 293, 1932.

[57] J. R. Davies, "How wrong is collisional Monte Carlo modeling of fast electron transport in high-intensity laser-solid interactions?," *Phys. Rev. E*, vol. 65, p. 026407, 2002.

[58] J. R. Davies, A. R. Bell, and M. Tatarakis, "Magnetic focusing and trapping of high-intensity laser-generated fast electrons at the rear of solid targets," *Phys. Rev. E*, vol. 59, p. 6032, 1999.

[59] A. R. Bell and R. J. Kingham, "Resistive collimation of electron beams in laser-produced plasmas," *Phys. Rev. Lett.*, vol. 91, p. 035003, 2003.

[60] A. P. L. Robinson and M. Sherlock, "Magnetic collimation of fast electrons produced by ultraintense laser irradiation by structuring the target composition," *Phys. Plasmas*, vol. 14, p. 083105, 2007.

[61] E. S. Weibel, "Spontaneously growing transverse waves in a plasma due to an anisotropic velocity distribution," *Phys. Rev. Lett.*, vol. 2, p. 83, 1959.

[62] A. Bret, M.-C. Firpo, and C. Deutsch, "Characterization of the initial filamentation of a relativistic electron beam passing through a plasma," *Phys. Rev. Lett.*, vol. 94, p. 115002, 2005.

[63] M. Tatarakis, F. N. Beg, E. L. Clark, A. E. Dangor, R. D. Edwards, R. G. Evans, T. J. Goldsack, K. W. D. Ledingham, P. A. Norreys, M. A. Sinclair, M.-S. Wei, M. Zepf, and K. K., "Propagation instabilities of high-intensity laser-produced electron beams," *Phys. Rev. Lett.*, vol. 90, p. 175001, 2003.

[64] L. Silva, R. A. Fonseca, J. W. Tonge, W. B. Mori, and J. M. Dawson, "On the role of the purely transverse weibel instability in fast ignitor scenarios," *Phys.Plasma*, vol. 9, p. 2458, 2002.

[65] M. Storm, A. A. Solodov, J. F. Myatt, D. D. Meyerhofer, C. Stoeckl, C. Mileham, R. Betti, P. M. Nilson, T. C. Sangster, W. Theobald, and C. Chunlei, "High-current, relativistic electron-beam transport in metals and the role of magnetic collimation," *Phys. Rev.Lett.*, vol. 102, p. 235004, 2009.

[66] J. Fuchs, T. Cowan, P. Audebert, H. Ruhl, L. Gremillet, A. Kemp, M. Allen, A. Blazevic, J. C. Gauthier, M. Geissel, M. Hegelich, S. Karsch, P. Parks, M. Roth, Y. Sentoku, R. Stephens, and E. M. Campbell1, "Spatial uniformity of laser-accelerated ultrahigh-current mev electron propagation in metals and insulators," *Phys. Rev. Lett*, vol. 91, p. 255002, 2003.

[67] K. L. Lancaster, J. Pasley, J. S. Green, D. Batani, S. Baton, R. G. Evans, L. Gizzi, R. Heathcote, C. H. Gomez, M. Koenig, P. Koester, A. Morace, I. Musgrave, P. A. Norreys, P. Perez, J. N. Waugh, and N. C. Woolsey, "Temperature profiles derived from transverse optical shadowgraphy in ultraintense laser plasma interactions at 6×10^{20} Wcm^{-2}," *Phys. Plasmas*, vol. 16, p. 056707, 2009.

[68] L. Volpe, D. Batani, G. Birindelli, A. Morace, P. Carpeggiani, M. H. Xu, F. Liu, Y. Zhang, Z. Zhang, X. X. Lin, F. Liu, P. F. Zhu, L. M. Meng, Z. H. Wang, Y. T. Li, Z. M. Sheng, Z. Y. Wei, J. J. Santos, and C. Spindloe, "Propagation of a short-pulse laser-driven electron beam in matter," *Phys.Plasmas*, vol. 20, p. 033105, 2013.

[69] M. H. Key, M. D. Cable, T. E. Cowan, K. G. Estabrook, B. A. Hammel, S. P. Hatchett, E. A. Henry, D. E. Hinkel, J. D. Kilkenny, J. A. Koch, W. L. Kruer, A. B. Langdon, B. F. Lasinski, R. W. Lee, B. J. MacGowan, A. Mackinnon, J. D. Moody, M. J. Moran, A. A. Offenberger, D. M. Pennington, M. D. Perry,

T. J. Phillips, T. C. Sangster, M. S. Singh, M. A. Stoyer, M. Tabak, G. L. Tietbohl, M. Tsukamoto, K. Wharton, and S. C. Wilks, "Hot electron production and heating by hot electrons in Fast Ignitor research," *Phys. Plasmas*, vol. 5, p. 1966, 1998.

[70] F. Pisani, A. Bernardinello, D. Batani, A. Antonicci, E. Martinolli, M. Koenig, L. Gremillet, F. Amiranoff, S. Baton, J. Davies, T. Hall, D. Scott, P. Norreys, A. Djaoui, C. Rousseaux, P. Fews, H. Bandulet, and H. Pepin, "Experimental evidence of electric inhibition in fast electron penetration and of electric-field-limited fast electron transport in dense matter," *Phys. Rev. E*, vol. 62, p. R5927, 2000.

[71] R. Kodama, P. A. Norreys, K. Mima, A. E. Dangor, R. G. Evans, H. Fujita, Y. Kitagawa, K. Krushelnick, T. Miyakoshi, N. Miyanaga, T. Norimatsu, S. J. Rose, T. Shozaki, K. Shigemori, A. Sunahara, M. Tampo, K. A. Tanaka, Y. Toyama, Y. Yamanaka, and M. Zepf, "Fast heating of ultrahigh-density plasma as a step towards laser Fusion Ignition," *Nature*, vol. 412, p. 798, 2001.

[72] J. Pasley, M. Wei, E. Shipton, S. Chen, T. Ma, F. Beg, N. Alexander, R. Stephens, A. MacPhee, D. Hey, *et al.*, "Nail-like targets for laser-plasma interaction experiments," *Plasma Science, IEEE Transactions on*, vol. 36, p. 1128, 2008.

[73] A. R. Bell, J. R. Davies, and S. M. Guerin, "Magnetic field in short-pulse high-intensity laser-solid experiments," *Phys. Rev. E*, vol. 58, p. 2471, 1998.

[74] A. P. L. Robinson, H. Schmitz, and J. Pasley, "Rapid embedded wire heating via resistive guiding of laser-generated fast electrons as a hydrodynamic driver," *Phys. Plasmas*, vol. 20, p. 122701, 2013.

[75] A. P. L. Robinson, H. Schmitz, J. S. Green, C. P. Ridgers, N. Booth, and J. Pasley, "Control of wire heating with resistively guided fast electrons through an inverse conical taper," *Phys. Plasmas*, vol. 22, p. 043118, 2015.

[76] H. Nishimura, R. Mishra, S. Ohshima, H. Nakamura, M. Tanabe, T. Fujiwara, N. Yamamoto, S. Fujioka, D. Batani, M. Veltcheva, T. Desai, J. R., kawamura T., Y. Sentoku, R. Mancini, H. P., koike F., and M. K., "Energy transport and isochoric heating of a low-Z, reduced-mass target irradiated with a high intensity laser pulse," *Phys.Plasmas*, vol. 18, p. 022702, 2011.

[77] J. Myatt, W. Theobald, J. A. Delettrez, C. Stoeckl, M. Storm, T. C. Sangster, A. V. Maximov, and R. W. Short, "High-intensity laser interactions with mass-limited solid targets and implications for fast-ignition experiments on omega ep(a)," *Phys. Plasmas*, vol. 14, p. 056301, 2007.

[78] A. J. Kemp, Y. Sentoku, V. Sotnikov, and S. C. Wilks, "Collisional relaxation of superthermal electrons generated by relativistic laser pulses in dense plasma," *Phys. Rev. Lett-*, vol. 97, p. 235001, 2006.

[79] J. R. Davies, A. R. Bell, M. G. Haines, and S. M. Guerin, "Short-pulse high-intensity laser-generated fast electron transport into thick solid targets," *Phys. Rev. E*, vol. 56, p. 7193, 1997.

[80] A. P. L. Robinson, *ZEPHYROS VERSION : 1.0 series*. CLF, 2014.

[81] J. Lindl, "Development of the indirect-drive approach to inertial confinement fusion and the target physics basis for ignition and gain," *Phys. Plasmas*, vol. 2, p. 3933, 1995.

[82] J. M. Blondin and D. C. Ellison, "Rayleigh-Taylor instabilities in young supernova remnants undergoing efficient particle acceleration," *The Astrophysical Journal*, vol. 560, p. 244, 2001.

[83] L. Rayleigh, "Investigation of the character of the equilibrium of an incompressible heavy fluid of variable density," *Proc. London Math. Soc.*, vol. 14, p. 170, 1882.

[84] G. Taylor, "The instability of liquid surfaces when accelerated in a direction perpendicular to their planes. I," *Proc. R. Soc. London. Ser. A. Math. and Phys. Sci.*, vol. 201, no. 1065, p. 192, 1950.

[85] W. M. Wood-Vasey, K. S. Budil, B. A. Remington, S. G. Glendinning, A. M. Rubenchik, M. Berning, J. O. Kane, and J. T. Larsen, "Computational modeling of classical and ablative Rayleigh–Taylor instabilities," *Laser and Particle Beams*, vol. 18, p. 583, 2000.

[86] H.-J. Kull, "Theory of the Rayleigh-Taylor instability," *Physics Reports*, vol. 206, p. 197, 1991.

[87] S. W. Haan, "Weakly nonlinear hydrodynamic instabilities in inertial fusion," *Phys. Fluids B: Plasma Phys.*, vol. 3, p. 2349, 1991.

[88] D. Ofer, D. Shvarts, Z. Zinamon, and S. A. Orszag, "Mode coupling in nonlinear Rayleigh–Taylor instability," *Phys. Fluids B: Plasma Phys.*, vol. 4, p. 3549, 1992.

[89] R. LeLevier, G. J. Lasher, and F. Bjorklund, "Effect of a density gradient on Taylor instability," 1955.

[90] S. E. Bodner, "Rayleigh-Taylor instability and laser-pellet fusion," *Phys. Rev. Lett.*, vol. 33, p. 761, 1974.

[91] H. Takabe, K. Mima, L. Montierth, and R. L. Morse, "Self-consistent growth rate of the Rayleigh-Taylor instability in an ablatively accelerating plasma," *Phys. Fluids*, vol. 28, p. 3676, 1985.

[92] A. J. Cole, J. D. Kilkenny, P. T. Rumsby, R. G. Evans, C. J. Hooker, and M. H. Key, "Measurement of Rayleigh–Taylor instability in a laser-accelerated target," *Nature*, vol. 299, p. 329, 1982.

[93] J. Nuckolls and L. Wood, "Laser compression of matter to super-high densities: Thermonuclear (CTR)," *Nature*, vol. 239, p. 139, 1972.

[94] J. D. Lindl and W. C. Mead, "Two-dimensional simulation of fluid instability in laser-fusion pellets," *Phys. Rev. Lett.*, vol. 34, p. 1273, 1975.

[95] K. S. Budil, B. A. Remington, T. A. Peyser, K. O. Mikaelian, P. L. Miller, N. C. Woolsey, W. M. Wood-Vasey, and A. M. Rubenchik, "Experimental comparison of classical versus ablative Rayleigh-Taylor instability," *Phys. Rev. Lett.*, vol. 76, p. 4536, 1996.

[96] R. Betti, V. N. Goncharov, R. L. McCrory, and C. P. Verdon, "Growth rates of the ablative Rayleigh–Taylor instability in inertial confinement fusion," *Phys. Plasmas*, vol. 5, p. 1446, 1998.

[97] V. Lobatchev and R. Betti, "Ablative stabilization of the deceleration phase Rayleigh-Taylor instability," *Phys. Rev. Lett.*, vol. 85, p. 4522, 2000.

[98] D. A. Martinez, V. A. Smalyuk, J. O. Kane, A. Casner, S. Liberatore, and L. P. Masse, "Evidence for a bubble-competition regime in indirectly driven ablative Rayleigh-Taylor instability experiments on the NIF," *Phys. Rev. Lett.*, vol. 114, p. 215004, 2015.

[99] M. E. Manuel, C. K. Li, F. H. Séguin, J. A. Frenje, D. T. Casey, R. D. Petrasso, S. X. Hu, R. Betti, J. Hager, D. D. Meyerhofer, and V. Smlyuk, "Rayleigh-Taylor-induced magnetic fields in laser-irradiated plastic foils," *Phys. Plasmas*, vol. 19, p. 082710, 2012.

[100] M. E. Manuel, M. Flaig, T. Plewa, C. K. Li, F. H. Séguin, J. A. Frenje, D. T. Casey, R. D. Petrasso, S. X. Hu, R. Betti, J. Hager, D. D. Meyer-

hofer, and V. Smalyuk, "Collisional effects on Rayleigh-Taylor-induced magnetic fieldsa)," *Phys. Plasmas*, vol. 22, p. 056305, 2015.

[101] M. Nakatsutsumi, J. R. Davies, R. Kodama, J. S. Green, K. L. Lancaster, K. U. Akli, F. N. Beg, S. N. Chen, D. Clark, R. R. Freeman, C. D. Gregory, H. Habara, R. Heathcote, D. S. Hey, K. Highbarger, A. J. Jaanimagi, M. H. Key, K. Krushelnick, T. Ma, A. MacPhee, A. J. Mackinnon, H. Nakamura, R. B. Stephens, M. Storm, M. Tampo, W. Theoblad, L. Van Woerkem, R. L. Weber, M. S. Wei, W. N. C., and P. A. Norreys, "Space and time resolved measurements of the heating of solids to ten million kelvin by a petawatt laser," *New J. Phys.*, vol. 10, p. 043046, 2008.

[102] L. D. Landau and E. M. Lifshitz, *Fluid Mechanics: Landau and Lifshitz: Course of Theoretical Physics*, vol. 6. Elsevier, 2013.

[103] D. L. Youngs, "Rayleigh-Taylor instability: numerical simulation and experiment," *Plasma Phys. Control. Fusion*, vol. 34, p. 2071, 1992.

[104] X. Ribeyre, V. T. Tikhonchuk, and S. Bouquet, "Compressible Rayleigh–Taylor instabilities in supernova remnants," *Physics of Fluids*, vol. 16, p. 4661, 2004.

[105] C. M. Huntington, C. C. Kuranz, R. P. Drake, A. R. Miles, S. T. Prisbrey, H.-S. Park, H. F. Robey, and B. A. Remington, "Design of experiments to observe radiation stabilized rayleigh-taylor instability growth at an embedded decelerating interface," *Phys. Plasmas*, vol. 18, p. 112703, 2011.

[106] M. F. Modest, *Radiative heat transfer*. Academic press, 2013.

[107] A. Vogler, J. H. M. J. Bruls, and M. Schussler, "Approximations for non-grey radiative transfer in numerical simulations of the solar photosphere," *Astronomy and Astrophysics*, vol. 421, p. 741, 2004.

[108] D. Salzmann, *Atomic physics in hot plasmas*. Oxford Univ. Press, 1998.

[109] E. Wagenaars, D. S. Whittaker, and G. J. Tallents, "A method to probe Rosseland and Planck mean opacities with high-order harmonics," *High Energy Density Physics*, vol. 7, p. 17, 2011.

[110] M. H. Mahdieh and S. Hosseinzadeh, "Calculation of the radiative opacity for some low Z plasmas produced by high power pulsed lasers," in 18^{th} *International Symposium on Gas Flow & Chemical Lasers & High Power Lasers*, p. 77511N, International Society for Optics and Photonics, 2010.

[111] J. Abdallah Jr and R. E. H. Clark, "Tops: A multigroup opacity code," tech. rep., Los Alamos National Lab., NM (USA), 1985.

[112] S. J. Rose, "Calculations of the radiative opacity of laser-produced plasmas," *Journal of Physics B: Atomic, Molecular and Optical Physics*, vol. 25, p. 1667, 1992.

[113] J. J. MacFarlane, I. E. Golovkin, and P. R. Woodruff, "HELIOS-CR–a 1-d radiation-magnetohydrodynamics code with inline atomic kinetics modeling," *Journal of Quantitative Spectroscopy and Radiative Transfer*, vol. 99, p. 381, 2006.

[114] J. T. Larsen and S. M. Lane, "HYADES— a plasma hydrodynamics code for dense plasma studies," *Journal of Quantitative Spectroscopy and Radiative Transfer*, vol. 51, p. 179, 1994.

[115] J. G. Rubiano, R. Rodrıguez, J. M. Gil, F. H. Ruano, P. Martel, and E. Mınguez, "A screened hydrogenic model using analytical potentials," *Journal of Quantitative Spectroscopy and Radiative Transfer*, vol. 72, p. 575, 2002.

[116] C. C. Smith, "A screened hydrogenic model with fine structure splitting," *High Energy Density Physics*, vol. 7, p. 1, 2011.

[117] R. Marchand and X. Bonnin, "Radiative losses and cooling rates in plasmas," *Phys. Fluids B: Plasma Phys.*, vol. 4, p. 2652, 1992.

[118] J. J. MacFarlane, "Development of spectral and atomic models for diagnosing energetic particle characteristics in fast ignition experiments," tech. rep., Prism Computational Sciences, Inc., 2009.

[119] S. S. Harilal, B. OShay, M. S. Tillack, and M. V. Mathew, "Spectroscopic characterization of laser-induced tin plasma," *J. Appl. Phys.*, vol. 98, p. 013306, 2005.

[120] A. R. Bell, R. G. Evans, and D. J. Nicholas, "Elecron energy transport in steep temperature gradients in laser-produced plasmas," *Phys. Rev. Lett.*, vol. 46, p. 243, 1981.

[121] R. J. Mason, "Apparent and real thermal inhibition in laser-produced plasmas," *Phys. Rev. Lett.*, vol. 47, p. 652, 1981.

[122] M. D. Rosen, H. A. Scott, D. E. Hinkel, E. A. Williams, D. A. Callahan, R. P. J. Town, L. Divol, P. A. Michel, W. L. Kruer, L. J. Suter, R. A. London, J. A. Harte, and G. B. Zimmerman, "The role of a detailed configuration accounting (DCA) atomic physics package in explaining the energy balance in ignition-scale hohlraums," *High Energy Density Physics*, vol. 7, p. 180, 2011.

[123] J. J. MacFarlane, I. E. Golovkin, R. C. Mancini, L. A. Welser, J. E. Bailey, J. A. Koch, T. A. Mehlhorn, G. A. Rochau, P. Wang, and P. Woodruff, "Dopant radiative cooling effects in indirect-drive Ar-doped capsule implosion experiments," *Phys. Rev. E*, vol. 72, p. 066403, 2005.

[124] A. P. L. Robinson, A. R. Bell, and R. J. Kingham, "Fast electron transport and ionization in a target irradiated by a high power laser," *Plasma Phys. Control. Fusion*, vol. 48, p. 1063, 2006.

[125] D. J. Hoarty, P. Allan, S. F. James, C. R. D. Brown, L. M. R. Hobbs, M. P. Hill, J. W. O. Harris, J. Morton, M. G. Brookes, R. Shepherd, J. Dunn, H. Chen, E. Von Marley, P. Beiersdorfer, H. K. Chung, R. W. Lee, G. Brown, and J. Emig, "Observations of the effect of ionization-potential depression in hot dense plasma," *Phys. Rev. Lett.*, vol. 110, p. 265003, 2013.

[126] M. Borghesi, A. J. Mackinnon, A. R. Bell, G. Malka, C. Vickers, O. Willi, J. R. Davies, A. Pukhov, and J. Meyer-ter Vehn, "Observations of collimated ionization channels in aluminum-coated glass targets irradiated by ultraintense laser pulses," *Phys. Rev. Lett.*, vol. 83, p. 4309, 1999.

[127] A. P. L. Robinson, M. Sherlock, and P. A. Norreys, "Artificial collimation of fast-electron beams with two laser pulses," *Phys. Rev. Lett.*, vol. 100, p. 025002, 2008.

[128] T. Ma, M. H. Key, R. J. Mason, K. U. Akli, R. L. Daskalova, R. R. Freeman, J. S. Green, K. Highbarger, P. A. Jaanimagi, J. A. King, K. L. Lancaster, S. P. Hatchett, A. J. Mackinnon, A. G. MacPhee, P. A. Norreys, P. K. Patel, R. B. Stephens, W. heobald, L. D. Van Woerkom, M. S. Wei, and S. C. Wilks, "Transport of energy by ultraintense laser-generated electrons in nail-wire targets," *Phys. Plasmas*, vol. 16, p. 112702, 2009.

[129] R. Kodama, Y. Sentoku, Z. L. Chen, G. R. Kumar, S. P. Hatchett, Y. Toyama, T. E. Cowan, R. R. Freeman, J. Fuchs, Y. Izawa, M. H. Key, Y. Kitagawa, K. Kondo, T. Matsuoka, H. Nakamura, M. Nakatsutsumi, P. A. Norreys, T. Norimatsu, R. A. Snavely, R. B. Stephens, M. Tampo, K. A. Tanaka, and T. Yabuuchi, "Plasma devices to guide and collimate a high density of MeV electrons," *Nature*, vol. 432, p. 1005, 2004.

[130] P. Audebert, R. Shepherd, K. B. Fournier, O. Peyrusse, D. Price, R. Lee, P. Springer, J.-C. Gauthier, and L. Klein, "Heating of thin foils with a

relativistic-intensity short-pulse laser," *Phys. Rev. Lett.*, vol. 89, p. 265001, 2002.

[131] A. P. L. Robinson and H. Schmitz, "Elliptical magnetic mirror generated via resistivity gradients for fast ignition inertial confinement fusion," *Phys. Plasmas*, vol. 20, p. 062704, 2013.

[132] A. A. Solodov, R. Betti, K. S. Anderson, J. F. Myatt, W. Theobald, and C. Stoecki, "Controlling the divergence of laser-generated fast electrons through resistivity gradients in fast-ignition targets," *Bull. Am. Phys. Soc.*, vol. 55, p. 69, 2010.

[133] A. P. L. Robinson, H. Schmitz, J. S. Green, C. P. Ridgers, and N. Booth, "Guiding of laser-generated fast electrons by exploiting the resistivity-gradients around a conical guide element," *Plasma Phys. Control. Fusion*, vol. 57, p. 064004, 2015.

[134] C. N. Danson, J. Collier, D. Neely, L. J. Barzanti, A. Damerell, C. B. Edwards, M. H. R. Hutchinson, M. H. Key, P. A. Norreys, D. A. Pepler, I. N. Rose, P. F. Taday, W. T. Toner, M. Trentlman, F. N. Walsh, T. B. Winstone, and R. W. W. Wyatt, "Well characterized $10^{19}\mathrm{Wcm}^{-2}$ operation of VULCAN—an ultra-high power Nd: glass laser," *Journal of Modern Optics*, vol. 45, p. 1653, 1998.

[135] M. Coury, D. C. Carroll, A. P. L. Robinson, X. H. Yuan, C. M. Brenner, M. Burza, R. J. Gray, K. L. Lancaster, Y. T. Li, X. X. Lin, D. A. MacLellan, H. Powell, M. N. Quinn, O. Tresca, C. G. Wahlstrom, D. Neely, and P. McKenna, "Injection and transport properties of fast electrons in ultraintense laser-solid interactions," *Phys. Plasmas*, vol. 20, p. 043104, 2013.

[136] J. J. Honrubia and J. Meyer-ter Vehn, "Fast ignition of fusion targets by laser-driven electrons," *Plasma Phys. Control. Fusion*, vol. 51, p. 014008, 2009.

[137] P. McKenna, A. P. L. Robinson, D. Neely, M. P. Desjarlais, D. C. Carroll, M. N. Quinn, X. H. Yuan, C. M. Brenner, M. Burza, M. Coury, P. Gallegos, R. J. Gray, K. L. Lancaster, Y. T. Li, X. X. Lin, O. Tersca, and G. G. Whalstrom, "Effect of lattice structure on energetic electron transport in solids irradiated by ultraintense laser pulses," *Phys. Rev. Lett.*, vol. 106, p. 185004, 2011.

[138] A. P. L. Robinson, R. J. Kingham, C. P. Ridgers, and M. Sherlock, "Effect of transverse density modulations on fast electron transport in dense plasmas," *Plasma Phys. Control. Fusion*, vol. 50, p. 065019, 2008.

[139] W. F. Huebner and W. D. Barfield, *Opacity*. Springer, 2014.

[140] S. P. Lyon and J. D. Johnson, "Los Alamos National Laboratory, Los Alamos, N M," *Report LA-UR*-92-3407, 1992.

[141] R. L. Burden and J. D. Faires, "Numerical analysis, 6^{th} edn. (brooks cole)," *Co., Pacific Grove, California*, 1997.

[142] B. A. Remington, M. M. Marinak, S. V. Weber, K. S. Budil, O. L. Landen, S. W. Haan, J. D. Kilkenny, and R. J. Wallace, "Single–mode Rayleigh–Taylor experiments in 2D and 3D," *Proceedings of the* 5^{th} *International Workshop on Compressible Turbulent Mixing*, 1996.

[143] C. K. Birdsall and A. B. Langdon, *Plasma physics via computer simulation*. CRC Press, 2014.